Università degli Studi dell'Aquila

Dipartimento di Scienze Fisiche e Chimiche

Scuola di Dottorato in Fisica

– Ciclo XXV –

Measurement of Seasonal Variation of Be7 flux with Borexino Experiment and New Observables Sensitive to Matter Effect from Updated Solar Neutrino Global Fit

Thesis Submitted for the degree of
Dottore di Ricerca in Fisica SSD Fis/04

Advisor
Dr. Aldo Ianni
Sezione LNGS INFN

Tutor
Prof. Sergio Petrera
Università e gruppo collegato
INFN dell'Aquila

Dottorando
Francesco Lombardi
Università dell'Aquila
Sezione LNGS INFN

PhD School Coordinator
Prof. Michele Nardone
Università e gruppo collegato
INFN dell'Aquila

Anno Accademico 2011-2012

Contents

Introduction

The measurement of the solar neutrino flux of Beryllium (ν_{Be7}) with Borexino experiment, represents another and important tile in what that, for several decades, has been the big puzzle of the solar neutrino physics. Together the previous results from KamLAND experiment, namely the measurement of the $\overline{\nu}$ flux from nuclear reactors, we obtained finally a univocal solution for the parameters of the flavour oscillation theory in which is involved the flavour of electronic neutrinos: Δm^2_{12} and $\tan^2\theta_{12}$. These parameters are part of the mixing matrix for the flavours of Mikheyev-Smirnov-Wolfenstein theory (MSW). In additional, from Daya Bay experiment, recently, has been published also the measurement of the parameter θ_{13} of MSW mixing matrix which for several time presented a big indetermination.

The combination of these results, together with those from atmospheric-neutrinos (ν_μ and ν_τ), allowed us to reach a good measurement of all main parameters of the mixing matrix, necessary to obtain the real flux emitted in the solar core from nuclear reactions. Unfortunately the high precision reached is not enough yet to perform a discrimination between the fluxes produced from high ($HZ_\odot$) and low ($LZ_\odot$) metallicity of the solar models. Effectively the most expected measurement, able to discriminates between two kinds of metallicity, concerns the neutrino fluxes produced from nuclear reactions in the CNO cycle, with a endpoint energy at 1.5 MeV. The expected flux difference produced in the two models is about of 30-35%. Actually, the unique experiment able to perform a measurement at these energies is Borexino. Unfortunately at these energies there are also the ^{210}Bi decay spectrum that, in the first three years of data taking, was subject to some not negligible variations. These background fluctuations prevented, until now, an accurate measurement.

In the last two years it was done a long purification campaign, reducing considerably all the main background components. This big result suggests that, in the next future, Borexino could perform a much more accurate estimation of CNO flux. The current estimation are not able to discriminate between two expected rates ($R^{LZ_\odot}_{CNO} = 3.5$ cpd/100ton for the low metallicity and $R^{HZ_\odot}_{CNO} = 5.0$ cpd/100ton for the high metallicity). The new challenges for the neutrino research, are related to the definition of neutrino mass hierarchy and to the Majorana's neutrino identification by mean of neutrinoless double beta decay ($\nu 02\beta$) and, at the same time, to find out the existence or not of sterile *neutrino and the measurement of CP angle in the MSW mixing matrix. These new frontiers of physics require much more accurate measurements by means of new and huge detectors of the tens of kilotons class that are going to be build.*

In this thesis it has been done a not trivial analysis, mainly for the critical features of the dataset: the measurement of the seasonal variation of the ν_{Be7} solar neutrino, due to the Earth revolution around the Sun. The latter represent the proof that what has been observed with Borexino is effectively a flux of particles coming from the Sun.

The seasonal modulation, indeed, is due to elliptical shape of the terrestrial orbit in which the eccentricity is equal to $\varepsilon = 0.0167$.

Effectively this measurement was hard to perform because of the very weak signal to noise ratio and because of the not complete background stability that featured the first 3 years of the data taking. This instability and the small amplitude of the expected signal (a variation of about 7% with respect to total flux and versus the 14% of statistical fluctuations), pushed myself to look for new methods to perform the signal analysis in order to extract the seasonal modulation informations hidden in the Borexino data. The "traditional" methods for the spectral analysis as FFT (Fast Fourier Transform, Lomb-Scargle or wavelet analysis, etc.) being based on Fourier transform, cannot be applied on non-stationary and non-periodical functions, as in the cases of any noisy signals in which signal-to-noise ratio SNR is $\ll 1$.

Forcing these algorithms to operate on data or functions with these features, they generate an overestimation of the real spectral component (signal harmonics) and then also the energy associated to the signal.

For more than one decade, in the Research Centers of Adaptive Data (RCADA-NASA) it has been developed a first algorithm able to decompose a non linear and stationary signal in its oscillating modes by N. Huang (1998): "The Empirical Mode Decomposition" (EMD). During these years the algorithms has been improved and extended to the so called "Ensemble Empirical Mode Decomposition" (EEMD) that we adopted and optimized for this kind of measurement. This innovative technique removed almost completely the statistical fluctuations allowing us to extract the expected signal, even if quietly covered by the statistical noise.

In the second part of the thesis I used the last Borexino results, in which I gave a substantial contribution to the software development for the spectral analysis and to implement an innovative algorithm for locating the inner vessel shape (" Dynamic Vessel Shape" *– DVS), to perform a study on the impact of Borexino results in the non standard interaction field (NSI), supposed for the weak interactions with the standard matter.*

In the first chapter I will introduce the neutrino physics and the principles for the flavour oscillation theory in the vacuum and in the matter. Therefore I will describe the standard solar model features and the main nuclear processes that generate the energy necessary to sustain the solar structure along with the neutrino fluxes that we observe on the Earth. In the second chapter I will discuss the main features of Borexino experiment and the data selection done in order to optimize the dataset for the analysis. In the third chapter I will introduce the software and mathematical tools for the EEMD based on Huang-Hilbert transform (HHT) in order to extract spectral information of the from the data. In the fourth chapter I will show the data analysis, together with all simulations done, in order to tune the best values of parameters used for applying the new method. In the fifth chapter I will introduce the non standard interaction (NSI) for the neutrino and relative modification of the MSW Hamiltonian. I will describe also the simulation of neutrino propagation in the sun and in the Earth matter, in order to study the effects of the non standard interactions during the neutrino propagation in a medium. I will discuss also the characteristics of the main solar neutrino experiments and the global fit, in order to study the results obtained with the NSI by means of the

simulations of neutrino propagation performed in the "Istituto de Fìsica Corpuscolar" fo Valencia (Spain) with Dr. Carlos Peña Garay as advisor.

Chapter 1

Neutrino Physics

The neutrino ν (and antineutrino $\overline{\nu}$) is a lepton type particle described by Standard Model (SM) as a massless particle. Its definition is due to the fact that, in all observed interactions, the right-hand (left-hand) chirality component was never observed. Therefore the SM cannot builds a mass term with the usual Yukawa mechanism as for all other particles. Nevertheless the massless neutrinos are in strong contrast with all observational evidences obtained in the last 60th years. The existence of effects as the solar neutrino disappearance, namely the flavour oscillation of the neutrinos, could be explained only with the existence of the neutrino mass.

The neutrino mass issue is, maybe, one of the main problems of the particle physics today. To solve this inconsistency of the Standard Model, it has been developed several theoretical models in which the neutrino was handled as either Dirac or Majorana particle or as both (*seesaw* models).

All these new models introduced to explain the nature of the neutrino masses may introduce new non standard interactions that, if reals, could be detected by means of modern neutrino detectors. We will discuss these non-standard interaction in the last chapter.

1.1 Neutrino Mass

1.1.1 General assumptions

In the Standard Model (SM) the neutrino particle ν_l (and its antiparticle $\overline{\nu_l}$) are defined as neutral fermions massless with spin $S = \frac{1}{2}$. These kind of particles can interact only by means of weak interactions. Along with charged leptons $l_L^{\mp}$, they are part of a isospin doublet ψ_L $(left)$ that is invariant under transformations of type $SU(2)_L \times U(1)_Y$:

$$\psi_L = \begin{pmatrix} \nu_e \\ e^- \end{pmatrix}_L ; \begin{pmatrix} \nu_\mu \\ \mu^- \end{pmatrix}_L ; \begin{pmatrix} \nu_\tau \\ \tau^- \end{pmatrix}_L \tag{1.1}$$

$$\psi_R = \quad e_R^- \quad ; \quad \mu_R^- \quad ; \quad \tau_R^-$$

The right-handed component, ψ_R in the chiral representation, is composed only by charged massive leptons $l_R^{\mp}$.

Experimentally we observed that in the weak interaction of neutrinos only the *left* component is involved, namely only ν_l chiral component, whereas the right component is never observed in any kind of interaction. For this reason we define ν_R as *sterile* neutrinos. They are not included among the particles described by SM.

The absence of *right* component for the neutrino does not enable the SM to have a Lagrangian term that could be associate to the neutrino masses. Moreover there are not strong reasons to put in the theory both neutrino masses and its *right-handed* component, except for giving a better symmetry between *quarks* and *leptons* families. For these reasons the neutrino field in the SM is described as a Weyl spinor defined by:

$$i\gamma^\mu \partial_\mu \nu_L = 0 \tag{1.2}$$

that describe the massless fermion fields.

The first experiments to perform a measurement of neutrino fluxes coming from the Sun showed a flux amounting to one third with respect to what predicted by the Standard Solar Model (SSM) [86]. This was the first evidence of so called *solar neutrino problem.*

These results create problems to the goodness of Standard Solar Model (SSM) and

the physical assumptions to calculate it. But the SSM capacity to reproduce the observed data and the improvement in the measurements of the cross sections for nuclear reactions, persuaded all to introduce a new theory to describe the disappearance of neutrinos and the flavor oscillation.

This theory is based on an idea due to Pontecorvo (1957) [97] in analogy with the regeneration of neutral K mesons [96].

The new theory needs of a mass term for neutrinos in the Lagrangian equation and a matrix to perform the flavors mixing. These two new elements can be introduced easily, but we need also of a theory that can explain the origin of them and mainly why, unlike quarks for which the masses m_u and m_d are of the same order of magnitude, in the case of m_ν their values are so small with respect to the charged lepton.

1.1.2 Neutrino Masses and Seesaw models

In order to provide a mass to neutrino field, we can use the usual Yukawa mechanism by writing the interaction term of neutrino field with the vacuum Higgs field. But to write this term we must introduce a right-hand term for the neutrino field.

To describe the right–handed chiral component of the neutrino field, we can use the Dirac formalism in which we assume the existence of a new particle: the neutrino sterile (ν_s). The Dirac formalism is the standard way to provide the mass to a particle field, but is not able to explain why the neutrino mass $m_\nu \ll m_l$.

The other class of models are based on formalism introduced by Majorana, in which we can build the chiral right–handed component of neutrino field using charge conjugation as follow:

$$\nu_R \equiv \nu_L^C = \mathcal{C}\overline{\nu_L}^T. \tag{1.3}$$

Following the Majorana formalism we can write a mass term for *left-handed* neutrinos:

$$\mathcal{L}_{mass}^M = -\frac{1}{2} m_\nu \, \overline{\nu_L}^C \, \nu_L + H.c. \tag{1.4}$$

where $H.c.$ means the Hermitian conjugate of Lagrangian term and

$$\overline{\nu_L}^C = -\nu_L^T \mathcal{C}^\dagger \tag{1.5}$$

This term, unfortunately, is not invariant under $SU(2)_L \times U(1)_Y$ transformation, then it is forbidden by the symmetry of Standard Model. A possible theoretical solution for this problem could be obtained through the so called *"seesaw"* model, in which the Lagrangian of neutrino field contains both terms of Yukawa interaction to provide a mass to Dirac field, and the term of Majorana mass for both components of the chiral representation, that are ν_L and ν_R.

The advantage of this representation is that, apart from giving a mass to neutrinos, it provides also a possible explanation for the huge difference between the mass of charge leptons and neutrinos [107].

Assuming the existence of the right–handed chiral component ν_R, in the *"seesaw"* mechanism, we can write simultaneously both mass terms for Dirac's neutrino:

$$\mathscr{L}^D = -m_D \overline{\nu_R}\, \nu_L + \text{H.c.}, \tag{1.6}$$

and two mass terms for the Majorana's neutrino for both chiral components ν_L and ν_R:

$$\mathscr{L}^L = \frac{1}{2} m_L\, \nu_L^T\, \mathcal{C}^\dagger \nu_L + \text{H.c.} \qquad \mathscr{L}^R = \frac{1}{2} m_R\, \nu_R^T\, \mathcal{C}^\dagger \nu_R + \text{H.c.}. \tag{1.7}$$

At last we obtain a Lagrangian term for both formalisms:

$$\mathscr{L}^{D+M} = \mathscr{L}^D + \mathscr{L}^L + \mathscr{L}^R =$$

$$\mathscr{L}^{D+M} = \frac{1}{2} N_L^T\, \mathcal{C}^\dagger\, M\, N_L + \text{H.c.} \tag{1.8}$$

in which

$$N_L = \begin{pmatrix} \nu_L \\ \nu_R^C \end{pmatrix} = \begin{pmatrix} \nu_L \\ \mathcal{C}\, \overline{\nu}_L^T \end{pmatrix} \tag{1.9}$$

represents the neutrino doublet in the new chiral representation. The mass matrix M is defined as:

$$M = \begin{pmatrix} m_l & m_D \\ m_D & m_R \end{pmatrix}. \tag{1.10}$$

In this representation, with a suitable change of phase for the chiral states, we can rule out the degree of freedom related to this phase, assuming both m_R and m_D real and positive and m_L complex. But in this way the eigenvalues of the mass for the chiral

fields are not well defined, therefore we perform a diagonalization of the mass matrix M in Eq.1.10, by means of the unitary transformation:

$$N_L = \hat{U}\, n_L \tag{1.11}$$

where

$$n_L = \begin{pmatrix} \nu_{1L} \\ \nu_{2L} \end{pmatrix} \tag{1.12}$$

is the column vector of the chiral field *left* of the neutrino mass eigenstates. The unitary matrix operator $\hat{U}$ reads:

$$\hat{U}^T\, M\, \hat{U} = \begin{pmatrix} m_1 & 0 \\ 0 & m_2 \end{pmatrix} \tag{1.13}$$

in which $m_k \geq 0$.

Using the transform Eq.1.11, the Dirac-Majorana term of matrix can be written as:

$$\mathscr{L}^{D+M} = \frac{1}{2} \sum_{k=1,2} m_k\, \nu_{kL}^T \mathcal{C}^\dagger\, \nu_{kL} + \text{H.c.} = -\frac{1}{2} \sum_{k=1,2} m_k \overline{\nu}_k\, \nu_k \tag{1.14}$$

in which ν_k is defined as:

$$\nu_k = \nu_{kL} + \nu_{kL}^C = \nu_{kL} + \mathcal{C}\, \overline{\nu}_{kL}^T. \tag{1.15}$$

This kind of formalism implies that the massive neutrinos are Majorana neutrinos. Among all possible choices, a very interesting one for the masses M_L, M_R and M_D is:

$$m_D \ll m_R; \qquad m_L = 0. \tag{1.16}$$

From the general case, with this selection we obtain that the terms of diagonal mass matrix are:

$$\hat{U}^T\, M\, \hat{U} = \text{diag}(m_1; m_2)$$

where m_1 and m_2 are defined as:

$$m_1 \simeq \frac{m_D^2}{m_R}, \quad m_2 \simeq m_R \tag{1.17}$$

then the weight of m_2 is equal to m_R, that is the heavier component of the right–handed neutrino mass (*"sterile"*):

$$\nu_{2L} \simeq \nu_R^C. \tag{1.18}$$

For ν_1, to which it corresponds the eigenvalue m_1, is the lighter eigenstate which corresponds to the left–handed eigenstate of neutrino mass:

$$\nu_{1L} \simeq -i\nu_L. \tag{1.19}$$

The idea to set $m_L = 0$ is natural because the mass terms for the Majorana left–handed component are not allowed by SM symmetry being invariant under $SU(2)_L \times U(1)_Y$ symmetry transformation.
So far it has not been possible to establish what does it determine the m_R and m_D mass values, maybe they are related to the energy scales of GUT or to the super-symmetry breaking. However we are yet in the theoretical speculations and there are not any experimental validations. We can note, anyway, that if the neutrinos are Majorana neutrinos, we should be able to observe the double neutrinoless beta decay ($0\nu2\beta$) [9].

1.2 Neutrino Oscillation

We start discussing the neutrino oscillation with two flavours in vacuum and in matter. In the case of propagation in matter, we consider only the case with slow varying density (Solar case). Afterwards, we will extend the same calculation to oscillation with three flavours and we will discuss also a modification of Mikheyev Smirnov Wolfenstein (MSW) theory, to perform a study on the effects of the matter potential.

1.2.1 Oscillation in the vacuum

The flavour state of neutrino $|\nu_l\rangle$ ($l = e, \mu, \tau$) is a superposition of mass states $|\nu_i\rangle$ ($i = 1, 2, 3$)

$$\begin{aligned} |\nu_l\rangle &= \textstyle\sum_{i=1}^{3} \hat{U}^*_{il} |\nu_i\rangle \qquad \textit{neutrino} \\ |\overline{\nu_l}\rangle &= \textstyle\sum_{i=1}^{3} \hat{U}_{il} |\overline{\nu_i}\rangle \qquad \textit{antineutrino} \end{aligned} \tag{1.20}$$

along, respectively, the eigenvalues of mass m_i ($m_1 < m_2 < m_3$) are oscillated. The matrix $\hat{U}_{il}$ and $\hat{U}^*_{il}$ are called mixing matrix and complex conjugate respectively. In the case of solar neutrinos, they are produced from β decay and electron capture, then only

with the electronic flavour. The oscillation process allows the mixing mainly between ν_e and ν_μ. Only in negligible part they becomes ν_τ. For this reason we can limit our discussion only to two flavours by treating the μ and τ flavour just as only one. Without losing the generality in a second step we can extend our discussion to three flavours. In the case of two flavours we can write the mixing matrix as:

$$\hat{U} = \cos\theta\hat{\mathbb{I}} + i\sin\theta\hat{\sigma}_2 = \begin{pmatrix} \cos\theta & 0 \\ 0 & \cos\theta \end{pmatrix} + i \begin{pmatrix} 0 & -i\sin\theta \\ i\sin\theta & 0 \end{pmatrix}$$

where $\hat{\sigma}_2$ is the second Pauli's matrix, then we obtain:

$$\hat{U} = \begin{pmatrix} \cos\theta & \sin\theta \\ -\sin\theta & \cos\theta \end{pmatrix}. \tag{1.21}$$

In our treatment we assume a mass hierarchy such that the lighter neutrino mass is the m_1. Therefore this has to be the predominant eigenvalue in the case of electron flavour. The same has to be in the case of m_2 mass eigenvalue for muon flavour ν_μ and m_3 for ν_τ. Following the Pontecorvo's theory [77], the difference between the mass eigenvalues, introduces in the equation of the motion a phase term that generate the mixing during the propagation in the vacuum.

The time evolution of a neutrino with a given flavour follow the Schrödineg equation:

$$i\frac{d}{dt}|\nu_l(t)\rangle = \hat{H}|\nu_l(t)\rangle. \tag{1.22}$$

The solution of this equation it's like:

$$|\nu_l(t)\rangle = e^{-i\hat{H}t}|\nu_l(0)\rangle \tag{1.23}$$

where the $\hat{H}$ it's the Hamiltonian of system defined as:

$$\hat{H} = \int d^3x\mathcal{H}(x) = -\int d^3x\mathcal{L}(x) \tag{1.24}$$

where $\mathcal{H}(x)$ and $\mathcal{L}(x)$ are the Hamiltonian and Lagrangian densities of system. The solar neutrinos are ultra-relativistic due to the very small mass with respect to their emission energy. Using the natural unites ($h = c = 1$), we can write:

$$E_i = \sqrt{p_i^2 + m_i^2} \simeq p_i\left(1 + \frac{m_i^2}{2p_i^2}\right) = p_i + \frac{m_i^2}{2p_i}. \tag{1.25}$$

where E_i and p_i are the energy and momentum of eigenvalue ν_i.
Using the ultra-relativistic limit, we can put $E_i \simeq p_i$ obtaining:

$$E_i = p_i + \frac{m_i^2}{2E_i}. \tag{1.26}$$

We can calculate the magnitude of probability that an initial state $|\nu_l\rangle$, after a time t, coincides with another state $|\nu_{l'}\rangle$ by means of scalar product:

$$A_{l\to l'} = \langle \nu_{l'}|\nu_l(t)\rangle = \hat{U}_{l'i} e^{-i\hat{H}t} \hat{U}^*_{li}. \tag{1.27}$$

Therefore we can define the vacuum Hamiltonian as:

$$\begin{aligned} H^0_{l\to l'} = \hat{U}_{l'i} e^{-i\hat{H}t} \hat{U}^*_{li} = \hat{U}_{l'i} \left(p_i + \frac{m_i^2}{2E} \right) \hat{U}^*_{li} = \\ = p_i U_{l'i} \hat{U}^*_{li} + \hat{U}_{l'i} \frac{m_i^2}{2E} \hat{U}^*_{li} = \\ = p_i \delta_{li} + \hat{U}_{l'i} \frac{m_i^2}{2E} \hat{U}^*_{li} \end{aligned} \tag{1.28}$$

where E is the measured energy of neutrino.
We can also divide this Hamiltonian in two terms:

$$\hat{H} = e^{-i(\hat{H}_0 + \hat{H}_{eff})t} = e^{-ipt} e^{-i\hat{H}_{eff}t}. \tag{1.29}$$

The momentum of neutrino, when emitted by a nuclear reaction, is fixed. Therefore the term e^{-ipt} represents a global phase that could be ruled out by means of re-phasing, without changing the term that introduces the oscillation.
In the vacuum the flavour oscillation comes from the effective Hamiltonian H_{eff}, defined as:

$$H_{eff} = H_1 = \hat{U}_{l'i} \, \frac{m_i^2}{2E} \, \hat{U}^*_{li}. \tag{1.30}$$

In two flavours case we define the Hamiltonian as:

$$H_1 = \frac{1}{2E} \begin{pmatrix} \cos\theta & \sin\theta \\ -\sin\theta & \cos\theta \end{pmatrix} \begin{pmatrix} m_1^2 & 0 \\ 0 & m_2^2 \end{pmatrix} \begin{pmatrix} \cos\theta & -\sin\theta \\ \sin\theta & \cos\theta \end{pmatrix}. \tag{1.31}$$

performing the following substitution:

$$\begin{cases} m_1^2 = \dfrac{m_1^2 + m_2^2}{2} - \dfrac{m_1^2 - m_2^2}{2} = -\dfrac{\Delta m^2}{2} \\ \\ m_2^2 = \dfrac{m_1^2 + m_2^2}{2} + \dfrac{m_1^2 - m_2^2}{2} = \dfrac{\Delta m^2}{2} \end{cases} \tag{1.32}$$

we can obtain a more compact formulation for the effective Hamiltonian:

$$H_{eff} = \frac{\Delta m^2}{4E} \begin{pmatrix} -\cos 2\theta & \sin 2\theta \\ \sin 2\theta & \cos 2\theta \end{pmatrix} \tag{1.33}$$

Hence we can write the transition amplitude in the new mass eigenstate basis:

$$\begin{aligned} A_{l\to l'} = \langle \nu_{l'} | \nu_l(t) \rangle = \\ = \hat{U}^*_{l'i} e^{-i(H_0+H_{eff})\,t}\, \hat{U}_{li} \simeq -iU^*_{l'i} \left(p + \frac{m_i^2}{4p} \right)\, t\, \hat{U}_{li} \simeq \\ \simeq p\, \delta_{ll'} + \frac{\Delta m^2}{4p} \begin{pmatrix} -\cos 2\theta & \sin 2\theta \\ \sin 2\theta & \cos 2\theta \end{pmatrix}. \end{aligned} \tag{1.34}$$

In the case of two neutrinos, we can define the flavour state as:

$$\begin{aligned} |\nu_l\rangle = \cos\theta |\nu_1\rangle + \sin\theta |\nu_2\rangle \\ |\nu_{l'}\rangle = \cos\theta |\nu_2\rangle - \sin\theta |\nu_1\rangle; \end{aligned} \tag{1.35}$$

Performing the time evolution of the mass eigenstate:

$$|\nu_i(t)\rangle = e^{-iE_i t} |\nu_i(0)\rangle, \tag{1.36}$$

we obtain the time evolution of transition amplitude:

$$\begin{aligned} A_{l\to l'} = \langle \nu_{l'} | \nu_l(t) \rangle = \sin\theta\cos\theta \left(-\langle \nu_2 | \nu_2 \rangle e^{-iE_2 t} + \langle \nu_1 | \nu_1 \rangle e^{-iE_1 t} \right) = \\ = i \sin 2\theta \sin\left(\frac{E_2 - E_1}{2} t \right). \end{aligned} \tag{1.37}$$

Then the oscillation probability is defined as the square module of transition amplitude $A_{l\to l'}$:

$$P_{\nu_l \to \nu_{l'}} = |\langle \nu_{l'} | \nu_l(t) \rangle|^2 = \sin^2 2\theta \sin^2\left(\frac{E_2 - E_1}{2} t \right). \tag{1.38}$$

Since we are in the ultra-relativistic regime, the oscillation probability depends only on the difference between the energies E_i of two mass eigenstate $|\nu_i\rangle$. We can also rewrite this phase term in terms of differences of mass Δm^2 of two eigenstates as follows:

$$E_2 - E_1 = \frac{m_2^2 - m_1^2}{2E}, \tag{1.39}$$

where

$$E_i \simeq E + \frac{m_i^2}{2E}, \tag{1.40}$$

then we can write the probability as:

$$P_{l\to l'} = \sin^2 2\theta \sin^2\left(\frac{\Delta m^2 L}{4E}\right) \qquad \textit{(probability of disappearance)} \tag{1.41}$$

$$P_{l\to l} = 1 - \sin^2 2\theta \sin^2\left(\frac{\Delta m^2 L}{4E}\right) \quad \textit{(probability of survival of flavour)} \tag{1.42}$$

in which we have substituted $L = ct$.

From the equations 1.41 and 1.42, we can define also the typical oscillation length for a neutrino:

$$L^{osc} = \frac{4\pi E}{\Delta m^2}. \tag{1.43}$$

Therefore, from these relations, we can observe that oscillations in the vacuum depend only on the mass differences of their eigenstates. Furthermore it exists a degeneracy on the angle, because the $sin^2(2\theta)$ is symmetric with respect to:θ and $\pi/2 - \theta$.

Finally this degeneracy is solved by choosing ν_1 or ν_2 as lighter mass eigenstates predominant to generate the electronic flavour ν_e.

In this treatment we assumed only the propagation in vacuum, but also in this case we can find a solution for solar neutrinos (so-called VAC solution). The values for the mixing parameters are very far from the *Large Mixing Angle* solution (LMA) found with the results of KamLAND experiment [87].

As we will see in the next section, when the neutrino passes through the matter with a non homogeneous electronic density, as in the case of the Solar interiors, a resonant effect take place for the effective Hamiltonian term, that increase the oscillation effects increasing also the suppression factor for the electronic neutrinos with respect to vacuum case.

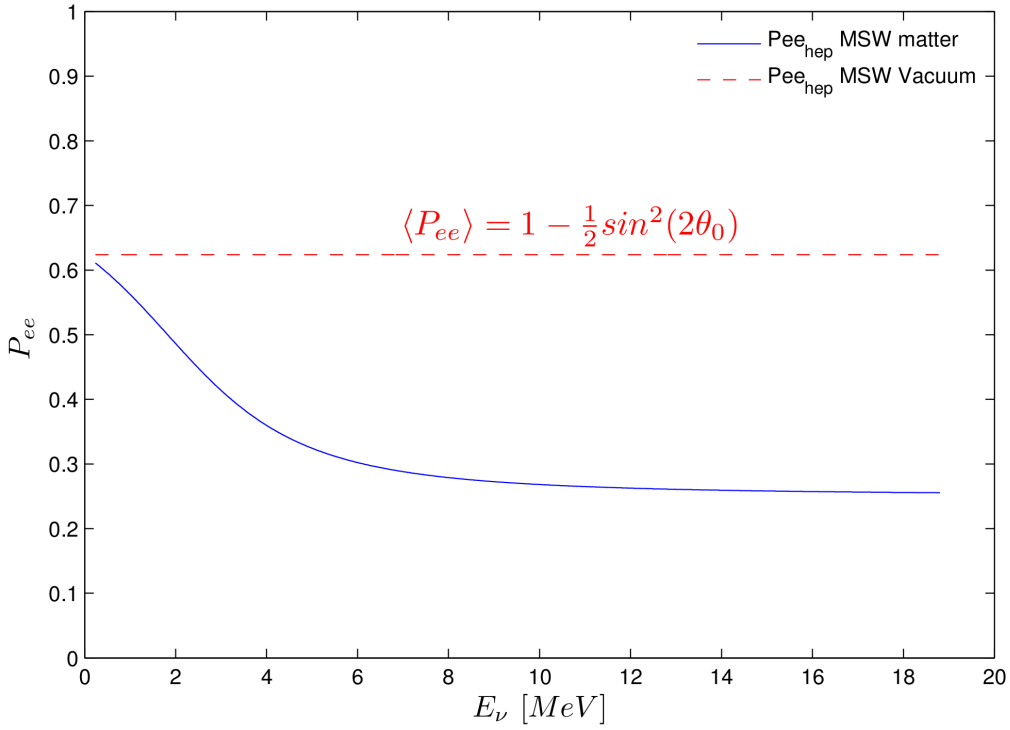

Figure 1.1: Comparison of survival probability as a function of energy with and without matter effect (MSW theory) by assuming $\Delta m^2 = 5.0780 \times 10^{-5}\ eV^2$ and $\sin^2(2\theta) = 0.7526$.

1.2.2 Oscillation in matter: Solar case

The ordinary matter is composed only by *electron* leptons, the unique channel with which the neutrino can perform an interaction is the weak channel. In the ordinary matter, the neutrinos ν_μ and ν_τ, in order to conserve the leptonic number, can interact only by means of the neutral boson Z^0 (through the neutral current, NC) whereas the electron neutrino can interacts also by means of the charged bosons W^+ and W^- (or charged current, CC).

The Lagrangian for the three flavours is composed, as well as the kinetic term, also by two weak interaction terms with fermion present in matter (e, $p(uud)$ and $n(udd)$):

$$\mathscr{L}_{eff} = \mathscr{L}_{Kin} + \mathscr{L}_{W^\pm} + \mathscr{L}_{Z^0}. \tag{1.44}$$

Since that the neutrino energies are of the order of MeV, $E_\nu \ll M_{W^\pm}$ (80 GeV) $< M_{Z^0}$ (91 GeV), we can approximate of the weak interaction constant with the Fermi constant

G_F. Therefore the elastic scattering for the charged current (CC) is described from Lagrangian:

$$\mathscr{L}_{W^\pm}(x) = -\frac{G_F}{\sqrt{2}} \left[\overline{\nu_e}(x)\gamma^\mu \left(1-\gamma^5\right) e(x)\right] \left[\overline{e}\gamma_\mu \left(1-\gamma^5\right) \nu_e(x)\right] \tag{1.45}$$

that, by applying the Fierz identity, becomes:

$$\mathscr{L}_{W^\pm}(x) = -\frac{G_F}{\sqrt{2}} \left[\overline{\nu_e}(x)\gamma^\mu \left(1-\gamma^5\right) \nu_e(x)\right] \left[\overline{e}\gamma_\mu \left(1-\gamma^5\right) e(x)\right]. \tag{1.46}$$

In this way we separated the electron and neutrino contributions. From Eq.1.46 we can calculate the expectation value of the interaction Hamiltonian of neutrinos with the background electron in the medium, assuming that they are stationary with respect to the incoming neutrinos:

$$\langle \nu_e(x), e(p_e,s)|\hat{H}_{W^\pm}|\nu_e(x), e(p_e,s)\rangle = \frac{G_F}{\sqrt{2}} \left[\langle \nu_e|\overline{\nu_e}(x)\gamma^\mu \left(1-\gamma^5\right) \nu_e(x)|\nu_e\rangle\right] \times$$

$$\times \int \mathrm{d}^3p_e\, f(E_e,T)\frac{1}{2}\sum_{s=\pm1}[\langle e^-(p_e,s)|\overline{e}(x)\gamma_\mu(1-\gamma^5)e(x)|e^-(p_e,s)\rangle], \tag{1.47}$$

in which the electron state $|e^-(p_e,s)\rangle$ is defined by:

$$|e^-(p_e,s)\rangle = \frac{1}{2E_eV} a_e^{s\dagger}(p_e)|0\rangle. \tag{1.48}$$

The function $f(E_e,T)$ is the statistical distribution of the electron energy E_e, that depends on the background temperature T. This function is normalized such that:

$$\int \mathrm{d}^3p_e f(E_e,T) = \rho_e V, \tag{1.49}$$

where ρ_e is the electron density in the medium and V is the Volume. Then $\rho_e V$ is the total number of electrons.

By performing the average on the helicity in the Eq.1.47 and integrating over d^3p_e, we obtain the effective Hamiltonian for the charged current:

$$\hat{H}_{eff}(x) = 2E_{\nu_e}\, V_{CC}[\overline{\nu_e}(x)\gamma^0(1-\gamma^5)\nu_e(x)] \tag{1.50}$$

where

$$V_{CC} = \sqrt{2}G_F\rho_e. \tag{1.51}$$

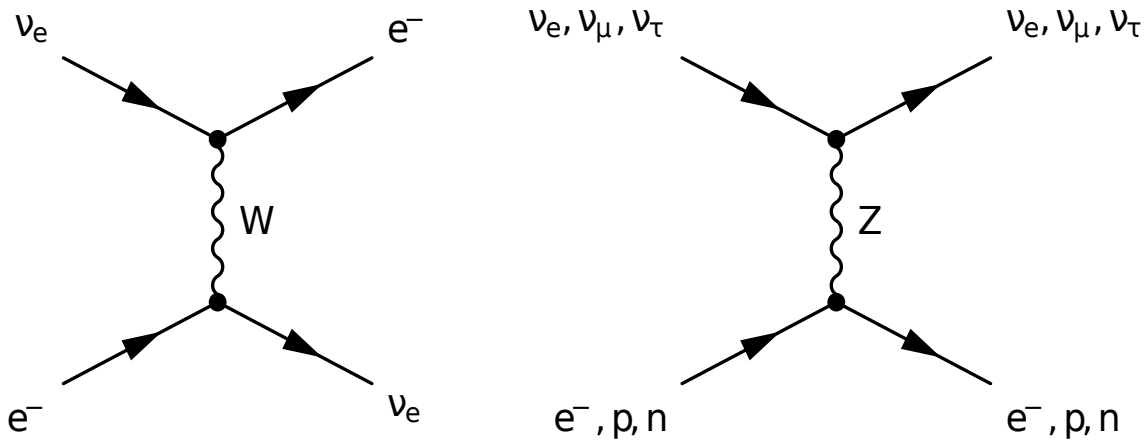

Figure 1.2: The Feynman diagrams of the coherent forward elastic scattering processes that generate the CC potential V_{CC} through $W^{\pm}$ exchange and the NC potential V_{NC} through Z^0 exchange.

In the integral present in Eq.1.47, the electronic term is composed by a vectorial part $\overline{e}\gamma_\mu e$ and a axial part $\overline{e}\gamma_\mu\gamma^5 e$ $(V-A)$. The vectorial part determines the current in the medium that vanishes in average. The axial term vanishes because there are not present resultant magnetic fields able to polarize the medium. Therefore the only term present is the electronic density $J_e = (\rho_e(x), \vec{\mathbf{J}}_e) \equiv \rho_e(x)$.
The interaction for the neutral current (NC) is given by the equation:

$$\mathscr{H}_{eff}^{NC} = \frac{G_F}{\sqrt{2}} \sum_{l=e,\mu,\tau} \left[\overline{\nu_l}(x)\gamma^\mu(1-\gamma^5)\nu_l(x)\right] \sum_{\mathcal{F}=p,n,e} \left[\overline{\mathcal{F}}(x)\gamma_\mu(g_V^{\mathcal{F}} - g_A^{\mathcal{F}}\gamma^5)\mathcal{F}(x))\right] \quad (1.52)$$

in which $\mathcal{F}$ represents all fermions present in ordinary matter, that are the protons $p(uud)$, the electrons e and the neutrons $n(udd)$. The potential of matter is generated by the interaction of all flavours with the fermions $\mathcal{F}$:

$$V_{NC}^{\mathcal{F}} = \sqrt{2} G_F \rho_{\mathcal{F}} g_V^{\mathcal{F}} \qquad (\mathcal{F} = e, p, n). \quad (1.53)$$

Since the matter is neutral in average, the number of electron is equal to the protons number, therefore the respective contributions cancel out each other:

$$g_V^e = -\frac{1}{2} + 2\sin^2\theta_W \qquad elettroni \quad (1.54)$$

$$g_V^p = 2g_V^u + g_V^d = \frac{1}{2} - 2\sin^2\theta_W \qquad protoni \quad p = uud. \quad (1.55)$$

The only contribution remaining is the one provided by neutrons:

$$g_V^n = g_V^u + 2g_V^d = -\frac{1}{2} \qquad neutroni \quad n = udd. \tag{1.56}$$

Therefore the term of the matter potential for neutral current is:

$$V_{NC} = -\frac{1}{2}\sqrt{2}G_F\rho_n. \tag{1.57}$$

This potential, unlike the one provided by charged currents, is in common to all three flavours of neutrinos, therefore originates a global phase term that does not modify the flavour oscillation term. It can be ruled out making a simply change of the global phase that does not change the Hamiltonian. The time evolution of a neutrino with a given flavour ν_l ($l = e,\ \mu,\ \tau$) and with momentum $\vec{p}$, is described by the following Hamiltonian:

$$\hat{H} = \hat{H}_0 + \hat{H}_I = \hat{H}_{eff} + \hat{H}_I \tag{1.58}$$

where $\hat{H}_{eff}$ is the vacuum term of Eq.1.33, for which the mass states $|\nu_i\rangle$ ($i = 1, 2, 3$) are eigenstates ($\hat{H}_{eff}|\nu_i\rangle = E_i|\nu_i\rangle$ and $E_i = \sqrt{\vec{p_i}^2 + m_i^2}$) and $\hat{H}_I$ is the matter interaction term:

$$\hat{H}_I|\nu_l\rangle = V_l|\nu_l\rangle \tag{1.59}$$

in which V_l is matter potential defined as sum of the charged and neutral current contributions:

$$V_l = V_{CC}\delta_{le} + V_{NC} = \sqrt{2}G_F(\rho_e\delta_{le} - \frac{1}{2}\rho_n) \qquad (\delta_{le} = 0 \text{ se } l \neq e). \tag{1.60}$$

In the case of two flavours, we can write the effective Hamiltonian through the matter as:

$$\hat{H}_{eff}^{matter} = \hat{H}_{eff} + 2E\hat{V}_{CC}(x) =$$
$$= \frac{\Delta m^2}{2}\begin{pmatrix} -\cos 2\theta & \sin 2\theta \\ \sin 2\theta & \cos 2\theta \end{pmatrix} + \begin{pmatrix} 2\sqrt{2}EG_F\rho_e(x) & 0 \\ 0 & 0 \end{pmatrix} \tag{1.61}$$

where it has been added, in the Eq.1.33, also the charged current interaction term due to the electron neutrinos interaction with the matter electrons. Therefore we can rewrite the matter potential V_{CC} as:

$$\hat{V}_{CC}(x) = \begin{pmatrix} \sqrt{2}G_F\rho_e(x) & 0 \\ 0 & 0 \end{pmatrix} = \sqrt{2}G_F\rho_e(x)\begin{pmatrix} 1 & 0 \\ 0 & 0 \end{pmatrix} =$$

$$= \sqrt{2} G_F \rho_e(x) \left[\begin{pmatrix} \frac{1}{2} & 0 \\ 0 & \frac{1}{2} \end{pmatrix} + \begin{pmatrix} \frac{1}{2} & 0 \\ 0 & -\frac{1}{2} \end{pmatrix} \right] \tag{1.62}$$

The first term in the Eq.1.62 becomes a simply global phase that we can eliminate, obtaining the diagonal term called *Wolfenstein* term:

$$\hat{V}_{CC}(x) = \frac{1}{2} \begin{pmatrix} \sqrt{2} G_F \rho_e(x) & 0 \\ 0 & -\sqrt{2} G_F \rho_e(x) \end{pmatrix}, \tag{1.63}$$

from which we obtain the final Hamiltonian of neutrino field in matter with electron density $\rho_e(x)$:

$$\hat{H}_{eff}^{matter} = \frac{\Delta m^2}{2} \begin{pmatrix} -\cos 2\theta & \sin 2\theta \\ \sin 2\theta & \cos 2\theta \end{pmatrix} + \frac{1}{2} \begin{pmatrix} 2\sqrt{2} E G_F \rho_e(x) & 0 \\ 0 & -2\sqrt{2} E G_F \rho_e(x) \end{pmatrix}. \tag{1.64}$$

To obtain a more compact form we can use the following definitions:

$$\begin{cases} \Delta m_m^2 \cos 2\theta_m = \dfrac{\Delta m^2}{4E} \cos 2\theta - \sqrt{2} G_F \rho_e(x) \\ \\ \Delta m_m^2 \sin 2\theta_m = \dfrac{\Delta m^2}{4E} \sin 2\theta \end{cases} \tag{1.65}$$

therefore we obtain:

$$\hat{H}_{eff}^{matter} = \frac{\Delta m_m^2}{2} \begin{pmatrix} -\cos 2\theta_m & \sin 2\theta_m \\ \sin 2\theta_m & \cos 2\theta_m \end{pmatrix}. \tag{1.66}$$

From the Eq.1.65 we can obtain the equation for Δm_m^2 and $\tan^2 2\theta_m$:

$$\Delta m_m^2 = \frac{1}{4E} \sqrt{\Delta m^2 \sin^2 2\theta - \left(\Delta m^2 \cos 2\theta - V_{CC}(x) \right)^2} \tag{1.67}$$

$$\tan 2\theta_m = \frac{\sin 2\theta}{\cos 2\theta - V_{CC}(x) \dfrac{4E}{\Delta m^2}} \tag{1.68}$$

In order to study the time evolution of neutrino field in matter, we assume that the initial flavour state of neutrino is the electron neutrino ($l = e$). We can neglect the common phases because they do not interfere with the terms that produce the oscillation.

The Schröedinger equation for the neutrino in matter is:

$$i \frac{\mathrm{d}}{\mathrm{d}t} \begin{pmatrix} \nu_e \\ \nu_\mu \end{pmatrix} = \frac{\Delta m_m^2}{4E} \begin{pmatrix} -\cos\theta_m & \sin\theta_m \\ \sin\theta_m & \cos\theta_m \end{pmatrix} \begin{pmatrix} \nu_e \\ \nu_\mu \end{pmatrix}. \tag{1.69}$$

Let us perform the following transformation:

$$\begin{pmatrix} \nu_e \\ \nu_\mu \end{pmatrix} = \hat{U}_m \begin{pmatrix} \nu_1 \\ \nu_2 \end{pmatrix} \tag{1.70}$$

where the unitary matrix

$$\hat{U}_m = \begin{pmatrix} \cos\theta_m & \sin\theta_m \\ -\sin\theta_m & \cos\theta_m \end{pmatrix} \tag{1.71}$$

is the effective mixing matrix in matter. Therefore we obtain a new time evolution equation in the mass eigenstate ν_1 and ν_2:

$$i\frac{\mathrm{d}}{\mathrm{d}t}\begin{pmatrix} \nu_1 \\ \nu_2 \end{pmatrix} = \frac{1}{4E}\begin{pmatrix} -\Delta m^2_m & -4Ei\frac{\mathrm{d}\theta_m}{\mathrm{d}t} \\ 4Ei\frac{\mathrm{d}\theta_m}{\mathrm{d}t} & \Delta m^2_m \end{pmatrix}\begin{pmatrix} \nu_1 \\ \nu_2 \end{pmatrix}. \tag{1.72}$$

The off-diagonal terms, proportional to $\mathrm{d}\theta_m/\mathrm{d}t$, are due to the derivative

$$\frac{\mathrm{d}}{\mathrm{d}t}\begin{pmatrix} \nu_e \\ \nu_\mu \end{pmatrix} = \frac{\mathrm{d}\hat{U}_m}{\mathrm{d}t}\begin{pmatrix} \nu_1 \\ \nu_2 \end{pmatrix} + \hat{U}_m\frac{\mathrm{d}}{\mathrm{d}t}\begin{pmatrix} \nu_1 \\ \nu_2 \end{pmatrix}.$$

If the matter density is constant then $\mathrm{d}\theta_m/\mathrm{d}t = 0$. Therefore the evolution of the effective masses of neutrinos in matter are decoupled providing the following transition probability:

$$P_{\nu_e\to\nu_\mu} = \sin^2 2\theta_m \sin^2\left(\frac{\Delta m^2_m x}{4E}\right) \tag{1.73}$$

that has the same structure of the vacuum case in Eq.1.41. If the matter density is not constant, as in the solar case that has an exponential trend as a function of the radius $\rho_e(x) \propto e^{-\alpha r/R_\odot}$, the off diagonal terms does not vanishes, but their values are:

$$\frac{d\theta_m}{dt} = \frac{1}{2}\frac{2E\sin 2\theta_m}{\Delta m^2_m}\frac{dV_{CC}(x)}{dx} \qquad (x = t \quad \text{natural units}). \tag{1.74}$$

The effect of the off diagonal term in Eq.1.72 is to generate a transition, that is a mixing, between the mass eigenstates in matter ν_1 and ν_2.

This transition is negligible if the off-diagonal terms are much more smaller than the differences between the diagonal terms. We can also introduce an *"adiabatic"* parameter γ in order to quantify the amount of this transition:

$$\gamma = \frac{\Delta m^2_m}{4E|d\theta_m/dt|}. \tag{1.75}$$

For the sake of simplicity in the calculation it is more advantageous to rewrite the adiabatic parameter in term of the vacuum parameters, that are Δm^2 and $\sin 2\theta_0$ as shown in [54]. Therefore we have:

$$\gamma = \frac{\Delta m^2 \sin^2 2\theta_0}{2E_\nu \cos 2\theta_0 |\nabla \ln \rho_e(x)|_{res}} \tag{1.76}$$

where $|\nabla \ln \rho_e(x)|_{res}$ is the logarithmic derivative of the electronic density evaluated in the point where the resonance occurs. In the case of the Sun this derivative is equal to $|\nabla \ln \rho_e(x)|_{res} \simeq 1/R_\odot$ being $\rho_e(r) \simeq 254\, \mathscr{N}_A\, e^{(-10.54\, r/R_\odot)}$ (where $\mathscr{N}_A$ is the Avogadro number).

If $\gamma \gg 1$ along all neutrino trajectory, the transition between the mass eigenstates is negligible, therefore the evolution is called adiabatic. In the Sun the time evolution of

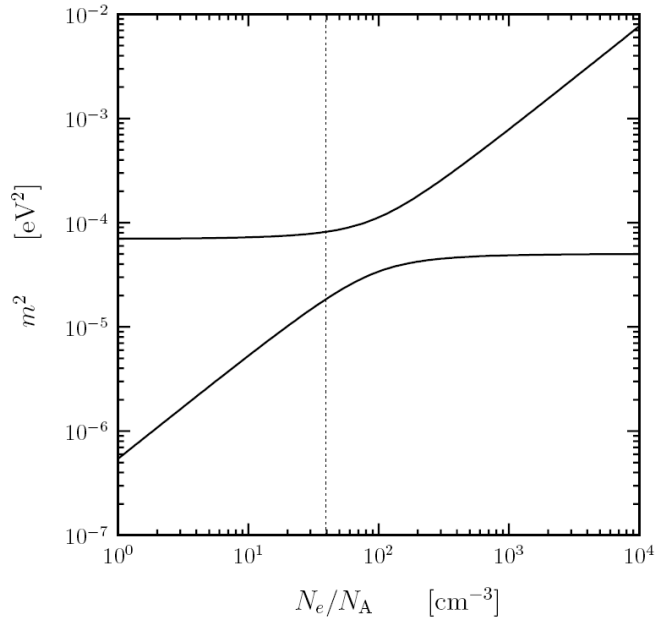

Figure 1.3: Trend of mass eigenstates with the electron density of the matter in the two flavours case with the Large Mixing Angle solution. The black dashed line is the point where the resonance occurs for a fixed energy of initial neutrino (in this case $E_\nu = 5\, MeV$ of solar case).

the neutrino states is adiabatic because of $\gamma > 10^4$, therefore the transition between the mass eigenstates cannot occur as shown in Fig.1.3.

A more general formulation for the survival probability was provided by Parke 1986

[55] for a neutrino in a non homogeneous medium:

$$P_{\nu_e \to \nu_e} = \frac{1}{2} + \left(\frac{1}{2} - P_c\right) \cos 2\theta_0 \cos 2\theta_m \tag{1.77}$$

where, from Eq.1.65 we obtain:

$$\cos 2\theta_m = \frac{\Delta m^2 \cos 2\theta_0 - 2EV_{CC}}{\Delta m_m^2} \tag{1.78}$$

while P_c defines the probability that, in the resonant point, it occurs the transition between the mass eigenstates $\nu_1 \leftrightarrows \nu_2$:

$$P_c = \frac{e^{-(\pi\gamma/2)F} - e^{-(\pi\gamma/2)(F/\sin^2\theta_0)}}{1 - e^{-(\pi\gamma/2)(F/\sin^2\theta_0)}}. \tag{1.79}$$

F depends on the density profile of the matter. In solar case the matter density varies as an exponential, therefore:

$$F = 1 - \tan^2\theta_0. \tag{1.80}$$

The adiabatic parameter in the Sun has a very large value as showed above, therefore from Eq.1.79, $P_c = 0$. This means that the neutrino states produced in a given mass eigenstate ν_i $(i = 1, 2, 3)$ at begining, will exit the solar surface in the same eigenstate (Fig.1.3).

We have an adiabatic evolution in the Sun because of the low energy of neutrinos. Particular cases take place in the supernova or neutron star, in which the matter density is very large with respect to the solar case.

The matter term depend from the matter density through the neutrino travel. In the solar core the matter density is $\rho_e(x) \simeq 150\, g \cdot cm^{-3}$ $(V_{CC} \gg \Delta m_0^2 \cos 2\theta_0)$ while it takes much more smaller values close to the solar surface, where the densities are similar to the vacuum value $(\Delta m_0^2 \cos 2\theta_0 > 2EV_{CC})$. The resonance occurs in the Sun when the following identity is satisfied:

$$2EV_{CC} = \Delta m_0^2 \cos 2\theta_0. \tag{1.81}$$

The crossing of the neutrinos through the resonance point is fundamental to explain the disappearence of solar neutrinos observed on the Earth. Starting from Eq.1.68, if the relation $2EV_{CC} = \Delta m_0^2 \cos 2\theta_0$ is verified, we have that:

$$\tan 2\theta_m \to \infty \qquad \text{and} \qquad \theta_m = 45^\circ,$$

that is the mixing between the flavour states is maximized independently from the real value of the mixing angle in vacuum θ_0.

The resonance depends obviously also on the neutrino energy, in particular for neutrino energies smaller that $E_\nu < 2MeV$, the mixing angle is equal to the vacuum $\theta_m = \theta_0$. Therefore the survival probability is:

$$P_{\nu_e \to \nu_e} = 1 - \frac{1}{2}\sin^2 2\theta_0. \tag{1.82}$$

For $E_\nu \geq 2MeV$ the survival probability becomes:

$$P_{\nu_e \to \nu_e} = \frac{1}{2} + \frac{1}{2}\cos 2\theta_0 \cos 2\theta_m. \tag{1.83}$$

In the case of high energy for the solar neutrino ($E_\nu \gg 2MeV$) as for the ^{8}B and hep neutrino ($E_\nu \simeq 15MeV$), the survival probability becomes:

$$P_{\nu_e \to \nu_e} \simeq \sin^2 \theta_0 \tag{1.84}$$

as shown in Fig.1.1.

1.2.3 Earth Regeneration

The Earth flavour regeneration is an effect due to the density of the Earth internal structure. During the day time the solar neutrino crosses only the atmosphere and a tiny layer of the crust, therefore these effect are completely negligible. But during the night time, starting from the sunset, the interaction of the neutrino flavour states with the matter electron density are not negligible. The Earth density reaches about 13 g/cm^3 that is close to a tenth of solar core density. Therefore the effect on flavour neutrino state are observable for neutrino energies greater than 1 MeV, as already confirmed by Borexino experiment in which no Day/Night asymmetry in the Beryllium neutrino flux has been observed [18]. The survival probability for solar electron neutrino is given in Eq.1.77. In general for three flavour case, assuming that $P_c = 0$ for solar/earth cases, the survival probability is:

$$P_{ee}^D = \cos^4 \theta_{13} \left(\frac{1}{2} + \frac{1}{2} \cdot \cos \theta_{12} \cdot \cos \theta_\odot \right) + \sin^4 \theta_{13} \tag{1.85}$$

where $\theta_\odot = \theta_m$ is evaluated in the resonance point inside the solar core. During the night time the neutrino flux passes across the earth interior and some of the previously oscillated neutrinos come back with electron flavour, increasing the number of electron neutrinos observed in the experiments. In general we can write the total survival probability in the Sun+Earth ($\odot + \oplus$) system as:

$$P_{ee}^{\odot+\oplus} = P_{e1}^{\odot} \cdot P_{1e}^{\oplus} + P_{e2}^{\odot} \cdot P_{2e}^{\oplus} \tag{1.86}$$

Starting from day time probability P_{ee}^{D}, we have for the night time total probability:

$$P_{ee}^{N} = P_{ee}^{D} - \cos 2\theta_\odot \cos^2 \theta_{13} \langle f_{reg} \rangle_{zenit} \tag{1.87}$$

where $\langle f_{reg} \rangle_{zenit}$ represents the average regeneration effect of the earth given by:

$$f_{reg} = P_{2e}^{\oplus} - \sin^2 \theta_{12} \cos^2 \theta_{13} \tag{1.88}$$

where P_{2e} is the transition probability of the second mass eigenstate to ν_e in the earth [50, 51].

1.3 Standard Solar Model and Neutrino Sources

1.3.1 The Standard Solar Model

The Sun is a star in the main sequence with a mass of $M_\odot = 1.9984 \times 10^{33}\ g$ with a age of $t_\odot = 4.57\ Gyr$, therefore the large part of energy produced by nuclear reaction is due to Hydrogen burning in the central core. The internal structure is characterized by a radiative central region (about 97% of the total mass), in which there is a slow diffusion of chemical elements and the radiative gradient of temperature is dominant. The more external layers of the solar structure, about 3% of the total mass, is occupied by the convective envelop where the convective beehives mix continuously the stellar plasma homogenizing the distribution of the chemical elements.

The solar model describes the time evolution of a star with one solar mass $M = 1\ M_\odot$ for a time interval equal to $t_\odot$ by reproducing the measured values of the main physical quantities:

- Solar Radius $R_\odot = (6.95508 \pm 0.0003) \times 10^{10}$ cm;
- Solar Luminosity $L_\odot = (3.844 \pm 0.015) \times 10^{33}$ erg s^{-1};
- Metallicity $(Z/X)_\odot$ of the chemical set used to define the solar model to reproduce the actual values of solar photosphere.

These quantities are obtained by solving a system of differential equations [82] for the pressure, radius, luminosity and temperature plus another one for the chemical evolution depending also on the time. The thermodynamic conditions of the plasma are described by the equation of state (EOS) [31, 32, 33]. Another important parameter in the solar model is the mixing length α, that is the distance in which a single cell of the solar structure lose its identity and its physical features of pressure and temperature. Varying the initial metallicity Z_i and initial Helium composition Y_i, along with the value of the mixing length α, the model tries to reproduce the actual physical features of the Sun by minimizing each observable with a precision of $\Delta X_i/X_i^{exp} \simeq 10^{-4}$. The information about the chemical abundances present in the Sun comes mainly from two very different sources: the photosphere spectral analysis and the analysis of chemical abundances of the chondrite meteorites of type CI [83].

Both kinds of analysis present advantages and disadvantages. The spectroscopic analysis of solar photosphere gives information about several elements, but the abundances are photosphere model depending, namely the way with which we reproduce the absorption line present in the spectrum. The analysis of chondrite does not provide a complete information about the lighter elements as H, He, C, N, O, and Ne, because their are volatile and therefore the meteorites are depleted of.

As results of this model we have the initial distribution of chemical elements in the pre-sequence state of the Sun X_i, Y_i, Z_i (very important in order to study the chemical environment in which the solar structure is born and also chemical evolution of this galaxy region), the depth of the convective envelope, measured also by means of helioseismological data, the density distribution of the proton, neutron and electrons in the solar structure, along with the temperature distribution and finally, related to temperature and chemical distributions the neutrino production distribution and relative

Source	BPS08(GS)	BPS08(AGS)	Difference
pp	$5.97(1 \pm 0.006)$	$6.04(1 \pm 0.005)$	1.2%
pep	$1.41(1 \pm 0.011)$	$1.45(1 \pm 0.010)$	2.8%
hep	$7.90(1 \pm 0.15)$	$8.22(1 \pm 0.15)$	4.1%
^{7}Be	$5.07(1 \pm 0.06)$	$4.55(1 \pm 0.06)$	10%
^{8}B	$5.94((1 \pm 0.11)$	$4.72(1 \pm 0.11)$	21%
^{13}N	$2.88(1 \pm 0.15)$	$1.89(1\ ^{+0.14}_{-0.13})$	34%
^{15}O	$2.15(1\ ^{+0.17}_{-0.16})$	$1.34(1\ ^{+0.16}_{-0.15})$	31%
^{17}F	$5.82(1\ ^{+0.19}_{-0.17})$	$3.25(1\ ^{+0.16}_{-0.15})$	44%
Cl	$8.46^{+0.87}_{-0.88}$	$6.86^{+0.69}_{-0.70}$	
Ga	$127.9^{+8.1}_{-8.2}$	$120.5^{+6.9}_{-7.1}$	

Table 1.1: Predicted solar neutrino fluxes from solar models. The table presents the predicted fluxes, in units of $10^{10}(pp)$, $10^{9}(\,^{7}\mathrm{Be})$, $10^{8}(pep, \,^{13}\mathrm{N}, \,^{15}\mathrm{O})$, $10^{6}(\,^{8}\mathrm{B}, \,^{17}\mathrm{F})$, and $10^{3}(hep)$ $\mathrm{cm}^{-2}\mathrm{s}^{-1}$. Columns 2 and 3 show BPS08 for high and low metalicities; and column 4 the flux differences between the models.

rates.

1.3.2 Solar Neutrino Sources

Looking at Tab.1.1 we observe the effect of different chemical composition on neutrino fluxes generated in the Sun by nuclear reactions. A different chemical composition of solar structure means a different metallicity and then a different temperature in solar core.

These have effects also on nuclear reaction rates and on densities of the solar core.

This is called also the solar metallicity problem in which only by means of neutrino fluxes measurement we can find a solution. The solar metallicity determine only a small variation in the solar neutrino fluxes about 10% in the ϕ_{ν}^{Be7} case. But the sum of the uncertainties of physical input in the solar model plus the uncertainties in solar neutrino detectors do not permit us to distinguish between two solar models

with different metallicity defined in GS98 [83] and AGS05 [84]. An update of the Oxygen abundances is done in AGSS09 [85] in which we have better agreement with helioseismological data with respect to AGS05 but without important changes in the values of solar neutrino fluxes shown in Tab.1.1.

Only the CNO neutrinos have important changes in the flux with a difference of about 30-35% between two models.

Presently the only experiment potentially able to perform the measurement of the CNO flux is Borexino. The stars in hydrogen burning phase ($H-burning$) as the Sun releases the nuclear energy by means of fusion of 4 hydrogen nuclei in one of Helium. In the solar case this process is done mainly by means of the so called *pp*-chain that produces about the 99% of the total energy and only for the 1% by mean of the bi-cycle of the CNO. The *pp*-chain starts with the reaction

$$p + p \rightarrow^2 H + e^+\nu_e \quad (1a) \qquad (BR \sim 99.75\%) \tag{1.89}$$

in which is produced the so called ν_{pp} with a very small energy ($E_{pp} \leq 0.42\, MeV$) but with most intense flux ($\phi_{pp} \sim 10^{10}$ cm^{-2} s^{-1}), about the 98% of total flux. Together this reaction, with a smaller branching ratio (BR $\sim 0.25\%$), there is also the electron capture by two protons:

$$p + p + e^- \rightarrow^2 H + \nu_e \quad (1b) \tag{1.90}$$

in this case the neutrino is monochromatic with a energy E_{pep}=1.442 MeV with a flux of $\phi_{pep} \sim 10^8$ cm^{-2} s^{-1}.

The Deuterium ^{2}H (or D) produced in these reaction react in a very fast way with another proton by producing the helium ^{3}He:

$$^2H + p \rightarrow^3 He + \gamma \quad (2) \tag{1.91}$$

From the following reactions done by the Helium it originates the four channels of the *pp*-chain, that is the $pp-I$:

$$^3He +^3 He \rightarrow^4 He + 2p \quad (3) \qquad (BR \sim 86\%) \tag{1.92}$$

the remaining 14% is done by means of the reaction:

$$^3He +^4 He \rightarrow^7 Be + \gamma \quad (4) \tag{1.93}$$

from which it descends the $pp-II$ channel:

$$^7Be + e^- \rightarrow^7 Li + \nu_e \quad (5) \tag{1.94}$$

done by the 98.89% of Beryllium produced and that generates also the neutrino ν_{Be7} observed in Borexino with a flux of the order $\phi_{Be7} \sim 10^9$ cm^{-2} s^{-1} and a monochromatic energy of $E_{Be7} = 0.862$ MeV. About 10% of the neutrinos produced by this reaction is emitted at lower energy ($E_{Be7^*} = 0.386$ MeV) due to a meta-stable state of the ^{7}Li nucleus.

A small part of the remaining Beryllium makes a reaction with the protons producing the $pp-III$ channel:

$$^7Be + p \rightarrow^8 B + \gamma \quad (6) \qquad (BR \sim 0.11\%) \tag{1.95}$$

The ^8B produced in this reaction is not stable and then it decaies by means of β^+ channel producing the ν_{B8} neutrino ($\phi_{B8} \sim 10^6$ cm^{-2} s^{-1}) with a maximum energy of $E_{B6} \leq 16$ MeV.

$$^8B \rightarrow^8 Be + e^+ + \nu_e \quad (7) \tag{1.96}$$

The last channel of the *pp*-chain is a very rare reaction with a BR$\sim 2 \times 10^{-5}\%$ with the highest emitted energy $E_{hep} \leq 18.55$ MeV:

$$^3He + p \rightarrow^4 He + e^+ + \nu_e \quad (8). \tag{1.97}$$

The neutrino flux for this reaction is very low about $\phi_{hep} \sim 10^3$ cm^{-2} s^{-1} The total energy produced in the *pp*-chain is equal to the difference between the four proton masses and the final nucleus of Helium (^{4}He) produced at the end of the process. Part of this energy is lost by means of the kinetic energy of the neutrinos.

In solar core it is present also a quantity of the Carbon, Nitrogen and Oxygen that produces also the ^{4}He by means of the CNO cycle. Also this cycle gets four nuclei of hydrogen and transforms it in the final ^{4}He nucleus by means of the proton capture. During this cycle they are produced three neutrino spectra that, after the ν_{Be7} are the most intense fluxes of neutrinos. In Tab.1.2 we summarize the main reactions and relative maximum energy for each neutrino spectrum.

Reazioni *CNO cycle*	Label	Energia ν (MeV)
$\mathbf{^{12}C + p \rightarrow\ ^{13}N} + \gamma$		
$^{13}N \rightarrow\ ^{13}C + e^{+} + \nu_e$	N13	$\leq 1.2 MeV$
$^{13}C + p \rightarrow\ ^{14}N + \gamma$		
$\mathbf{^{14}N + p \rightarrow\ ^{15}O} + \gamma$		
$^{15}O \rightarrow\ ^{15}N + e^{+} + \nu_e$	O15	$\leq 1.732 MeV$
$^{15}N + p \rightarrow\ ^{12}C + \alpha$		
$^{15}N + p \rightarrow\ ^{16}O + \gamma$		
$^{16}O + p \rightarrow\ ^{17}F + \gamma$		
$^{17}F \rightarrow\ ^{17}O + e^{+} + \nu_e$	F17	$\leq 1.732 MeV$
$^{17}O + p \rightarrow\ ^{14}N + \alpha$		

Table 1.2: Scheme of the nuclear reaction of the CNO bi-cycle with relative end-points of spectral energies.

The CNO fluxes are much more sensitive to the metallicity variation also because the efficiency of these reaction are highly sensitive to temperature variation in the solar core.

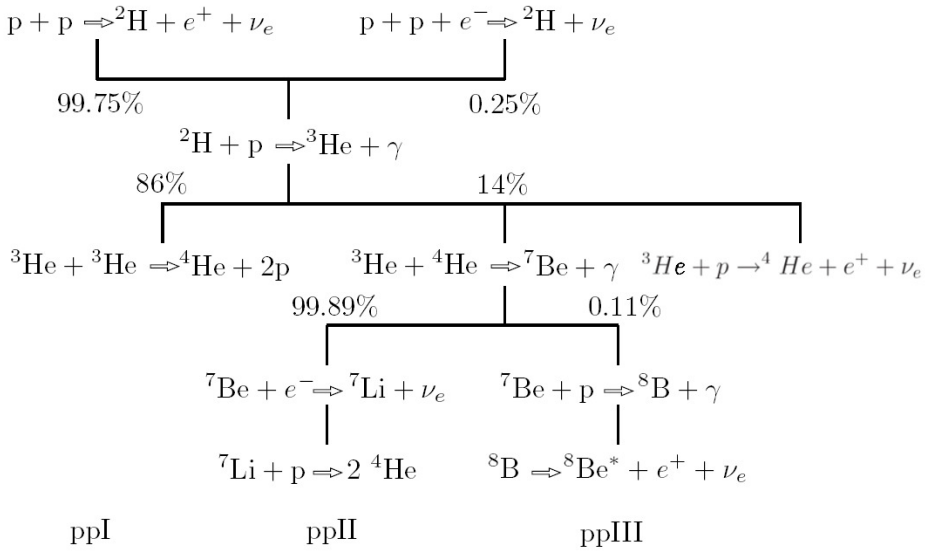

Figure 1.4: *pp*-chain reactions.

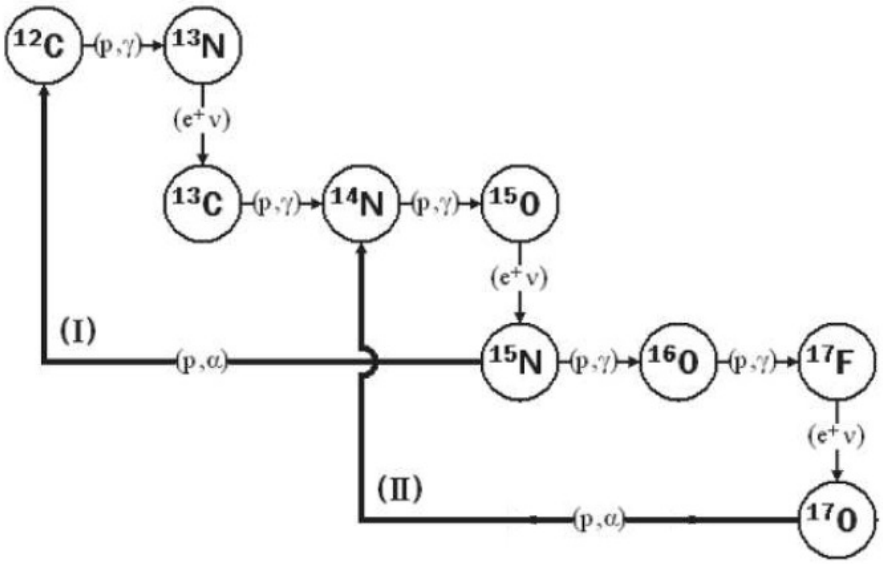

Figure 1.5: Bi-cycle CN-NO reactions.

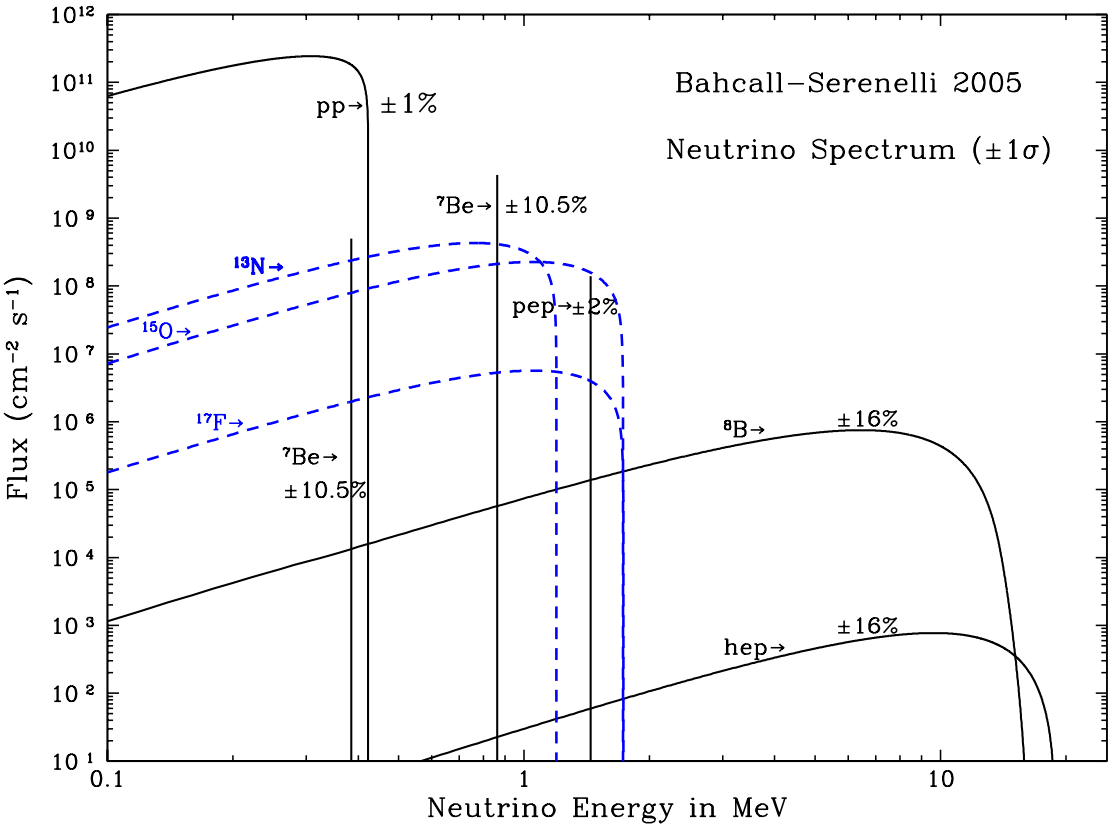

Figure 1.6: Total neutrino spectra generated in the solar core by nuclear reactions.

Chapter 2

Borexino Experiment

2.1 Introduction

The particular conditions of low background radioactivity and the innovative technique adopted to detect the neutrino-electron elastic scattering events, based on mineral liquid scintillator, make Borexino the only experiment able to detect in real time the solar neutrinos at low energy. The threshold energy of detector is posed to $E_{thr} > 250\,keV$, because of the presence of ^{14}C background of beta events present in the liquid scintillator.

The Borexino detector [16] is composed by a set of concentric shells of increasing radiopurity with, in the center, the inner scintillating core, as shown in Fig.2.2. The liquid scintillator is a mixture of pseudocumene (PC,$1,2,4-trimethylbenzene$) and PPO ($2,5-diphenyloxazole$, a fluorescent dye) at a concentration of 1.5 g/l [20]. The scintillator mass (278-ton) is contained in a 125 μm thick spherical nylon Inner Vessel (IV) [19] with 4.25 m radius surrounded by 2212 photo-multipliers (PMTs). A second 5.5 m radius nylon Outer Vessel (OV) surrounds the IV, acting as a barrier against radon and other background contaminations originating from outside. The region between the IV and the OV contains a passive shield composed of PC and 5.0 g/l (later reduced to 3.0 g/l) of DMP ($dimethylphthalate$), a material that quenches the residual scintillation of PC, so that the scintillation signals arising in this region are suppressed and, the only signals present, are those coming from the center of the IV

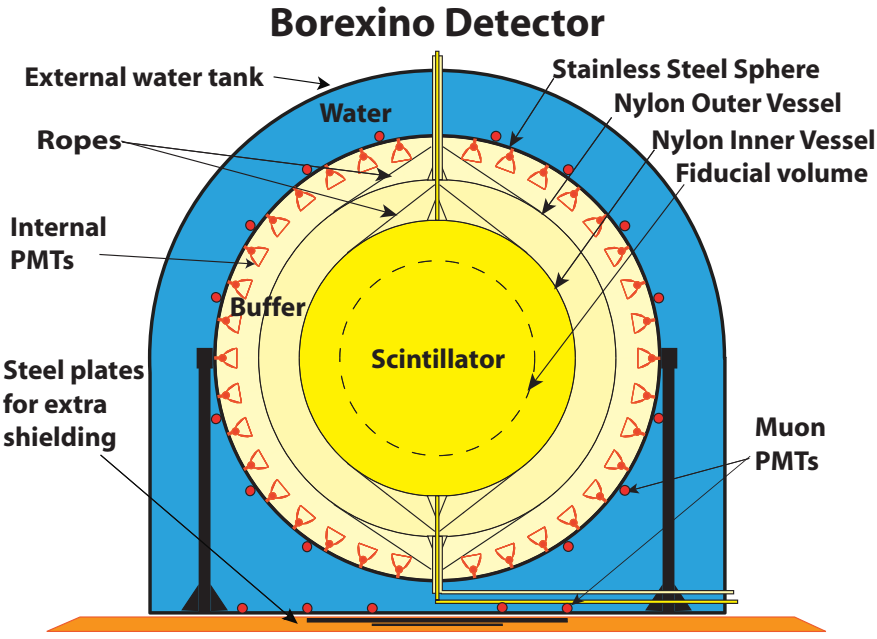

Figure 2.1: Internal structure of Borexino detector.

[22]. A 6.85 m radius the Stainless Steel Sphere (SSS) encloses the central part of the detector and serves also as a support structure for the 2212 8" PMTs (ETL 9351) PMTs.

The region between the OV and the SSS is filled with the same inert buffer fluid (PC plus DMP) which is layered between the IV and the OV. Finally, the entire detector is contained in a tank (9 m radius, 16.9 m height) filled by ultrapure water. The total liquid passive shielding of the central volume from external radiation (such as that originating from the rock) is thus 5.5 m of water equivalent (m.w.e). The water tank serves also as an active veto (Outer Detector OD) allowing the detection of the Čerenkov light induced by muons crossing the detector. For this purpose 208 PMTs are installed on the external side of the SSS [13].

2.2 Neutrino induced events

The solar neutrino particles are detected by means of elastic scattering with the electrons of the liquid scintillator. The incoming neutrino, in the scattering process lost

part of initial energy E_ν, that is transfered to the electrons and, by mean of recoil, produce the isotropic scintillation light signal. Therefore we lose any spatial information about the initial direction of neutrinos. The endpoints of neutrino spectra are given by:

$$T_e^{max} = \frac{E_\nu}{1 + \frac{2m_e c^2}{2E_\nu}} \tag{2.1}$$

where E_ν is the initial neutrino energy. In the case of ^7Be neutrino ($E_\nu = 0.862\,MeV$) and for the *pep* ($E_\nu = 1.44\,MeV$) the endpoints of recoil spectra are at T_e^{max} is $0.665\,MeV$ and $1.22\,MeV$ respectively. The cross section of this reaction is provided by standard electroweak theory. At high energies (for ^8B and *hep* neutrino) we have to take into account of the radiative corrections that reduce the probability of interaction of about 4% [58], instead at lower energies these corrections are negligible. Borexino can detect neutrinos of all flavors, but ν_e have a larger cross section than ν_μ and ν_τ, because ν_e interact through both charged and neutral current interactions, while the other one interact only via the neutral current. The ratio of the cross sections is about $\sigma_x/\sigma_e = 0.27$ for pp neutrinos, $\sigma_x/\sigma_e = 0.21$ for ^7Be neutrinos and $\sigma_x/\sigma_e = 0.15$ for neutrinos with energy higher that 5.5 MeV.

$$R = N_e \int dE' \frac{d\phi_\alpha}{dE'_\nu} \left[\sigma_e(P_{ee} + (1 - P_{ee})\sigma_x\right] \tag{2.2}$$

where N_e is the number of target electrons and $d\phi_\alpha/dE$ is the differential energy spectrum of solar neutrinos ν_α.

2.3 Background events

The Borexino experiment is located in the Hall C of the underground laboratory where the radioactivity of the rocks is much more lower with respect to other underground laboratory sites. The shielding provided by Monte Aquila with 1400 m of rocks ($\sim$ 3300 m.w.e. – *meters of water equivalent*) reduce the muon flux of a factor of 10^6 times ($\sim$ 4000 m^{-2} d^{-1}) identified by means of muon veto of outer detector (OD) [23]. Since the very rare neutrino events are practically indistinguishable from other ionizing events

Solar ν	GS98 Flux 10^{10}[cm^{-2}s^{-1}]	AGSS09 Flux 10^{10}[cm^{-2}s^{-1}]	e^- recoil end point [MeV]	Rate [cpd/100 tons]	Main background
pp	5.98 (1±0.006)	6.03 (1±0.006)	0.26	133	^{14}C
^{7}Be	5.00 (1± 0.07)	4.56 (1± 0.07)	0.665	47.3 ± 3.4	^{85}Kr, ^{210}Bi
pep	1.44 (1± 0.012)	1.47 (1± 0.012)	1.22	2.0 ± 0.4	^{11}C, ^{210}Bi
CNO	5.24 (1± 0.84)	3.76 (1± 0.60)	1.52	5.4 ± 0.8 ($3.8^{0.6}_{-0.5}$)	^{11}C, ^{210}Bi
^{8}B	5.58 (1± 0.14)	4.59 (1± 0.14)	17.72	0.49 ± 0.05	^{208}Tl, ext γ

Table 2.1: The solar neutrino flux, the expected neutrino interaction rate in Borexino and the main isotopes producing background. We report the fluxes of neutrinos calculated with the High Metallicity Solar Model (GS98SSM) and the ones obtained with the Low Metallicity model (AGSS09). The rate calculations are based on the high metallicity SSM using the MSW–LMA oscillation parameters from [10]. For the CNO neutrinos the interaction rate obtained with the low metallicity SSM is also reported. The last column lists the most relevant background component in the same energy region of recoil energy spectrum.

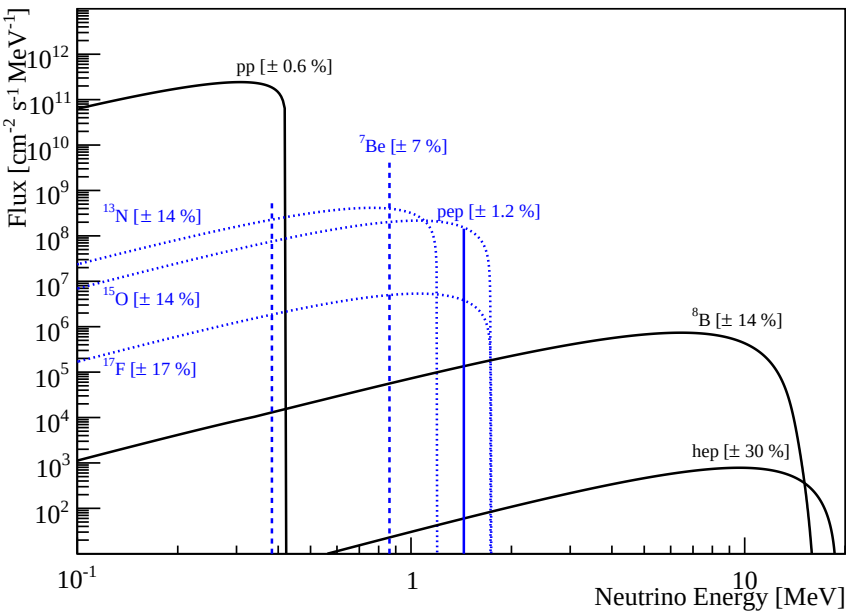

Figure 2.2: Solar neutrino spectrum.

produced by natural radioactivity at the same energy (250-800 keV), extremely high radiopurity standards must be met by the experiment. The main residual contaminates present in the fiducial volume have a maximum spectral energy lower than ($T_e < 2.6$ MeV). In several case we can eliminate their contribution by mean of identification of the events (fast coincidence or random events) but also because generated by muons

that traveling across the detector (i.e. ^{11}C events). Another way to identify the α-like events by β-like events (in which are present also the neutrino events) is through the pulse shape of the signal event. To perform all these identifications and selection has been developed a system of 15 *Standard Cuts* via software able to make a filtering of data with which to perform the analysis.
In Fig.2.3 is visible an example of spectral background population present in the Borexino spectrum and a typical effect of software filtering for the ^{11}C. In this case the reduction has been done of 98% [92]. The main components observable in the spectrum are:

^{14}C

The ^{14}C is produced in upper atmosphere layers by interaction of cosmogenetic neutrons with nitrogen. It has a half-life of 5730 years hence it is continuously generated by cosmic ray flux. The beta emission has an endpoint at $E_\beta = 156keV$. To reduce its contamination the liquid scintillator of Borexino is produced only with petroleum extracted from deeper underground sites, reducing in this way of a factor $\sim 10^{-18}\, g/g$ the contamination compared to the usual values [94]. Even with the large reduction in contamination, ^{14}C is by far the largest background in Borexino and it determines the lowenergy threshold of the detector. The ^{14}C rate is roughly 40 counts per second (cps) /100 *tons* (75 000 times higher than the expected ^{7}Be signal rate), though a hardware trigger threshold at 50 keV reduces the trigger rate to roughly 29 cps in the IV.

^{238}U and ^{222}Rn

The ^{238}U is a primordial radioactive isotope with a half life of 4.5 billion years. It is the most common isotope of uranium, with a natural abundance of 99.3%. The concentration of contaminants of the ^{238}U chain in secular equilibrium can be measured by identifying the fast decay sequence ^{214}Bi – ^{214}Po:

$$^{214}\mathrm{Bi} \rightarrow {}^{214}\mathrm{Po} + \mathrm{e}^- + \bar{\nu}_\mathrm{e} \tag{2.3}$$

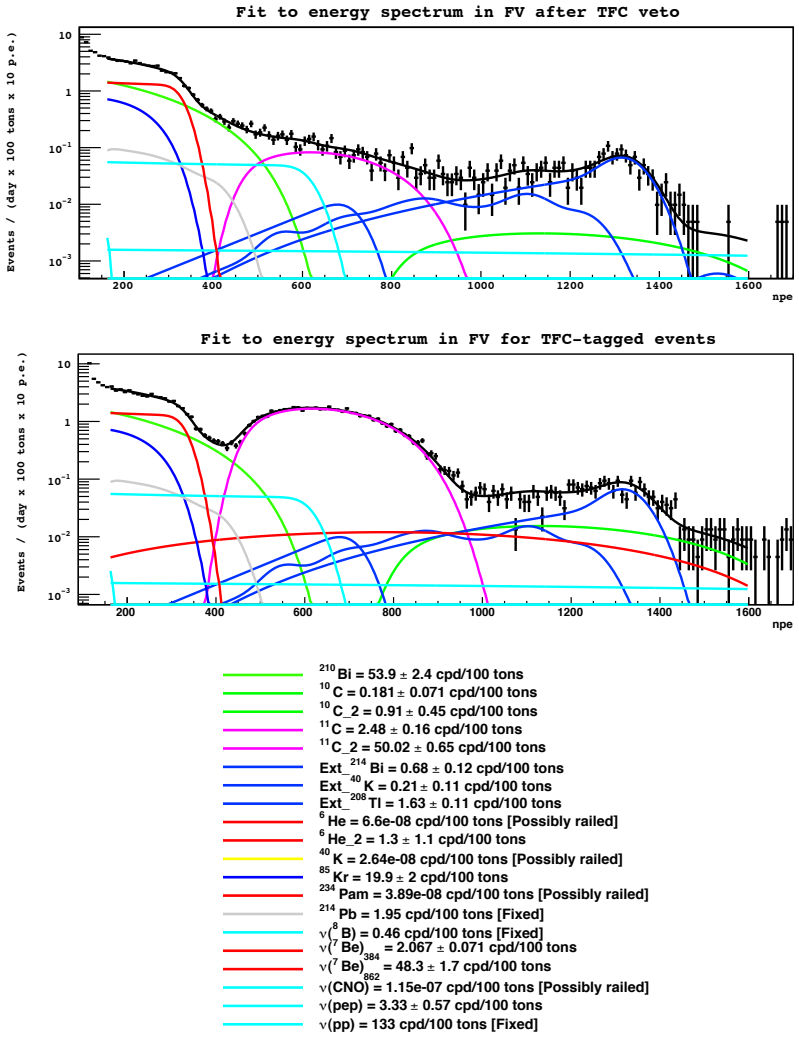

Figure 2.3: List of background components present in the Borexino spectrum after the Standard cuts. In the upper figure the ^{11}C spectrum (magenta) is reduced by means of three fold coincidences [24, 92]. In both the figures have been subtracted the monoenergetic peak of ^{210}Po (α-particle) by mean of statistical subtraction.

$$^{214}\mathrm{Po} \rightarrow {}^{210}\mathrm{Pb} + \alpha, \tag{2.4}$$

with $\tau = 237$ μs, Q of the ^{214}B–decay equal to 3.272 MeV and α energy of 7.686 MeV that offers a delayed coincidence tag. However, these two isotopes are ^{222}Rn daughters and the hypothesis of secular equilibrium is often invalid due to radon diffusion through surfaces or the possible contamination of the scintillator with radon coming from air. The ^{238}U concentration in the scintillator has been inferred from the asymptotic ^{214}Bi –

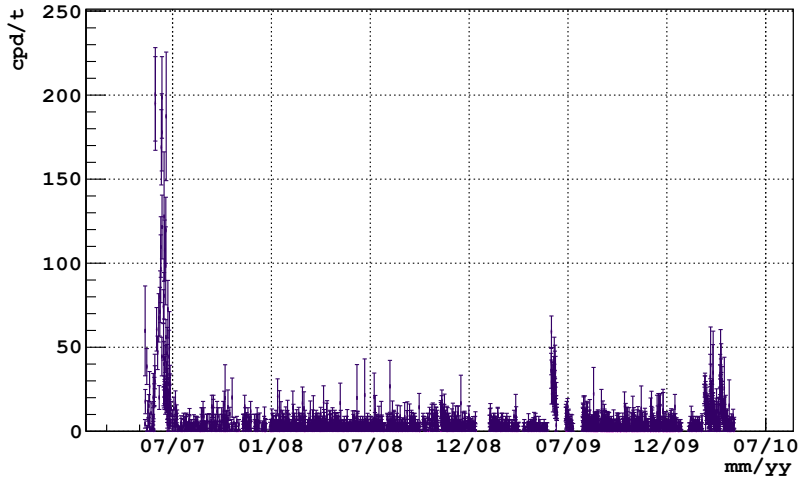

Figure 2.4: ^{214}Bi – ^{214}Po events during the whole data taking. The peak are present in coincidence of some operations within the detector as refilling or calibration campaigns in which have been inserted some tools from the external clean rooms. The radon present in the air had increased for few days the contaminations of Radon.

^{214}Po rate in the FV in absence of operations. The mean event rate in the FV in the period from May 2007 to May 2010 is (1.72 ± 0.06) cpd/100 tons while the mean asymptotic rate during periods far from any detector operation is (0.57 ± 0.05) cpd/100 tons. This last number has been used to evaluate the intrinsic ^{238}U contamination of the scintillator assuming secular equilibrium in the radioactive chain. The resulting contamination of (5.3 ± 0.5) × 10^{-18} g/g. This is 20 times lower than the target design of Borexino. Figure 2.4 shows the ^{214}Bi – ^{214}Po rate versus time in the whole scintillator volume.

^{11}C

The ^{11}C is the dominant cosmogenic background in Borexino and the biggest challenge for the measurement of *pep* and CNO neutrinos. About 95% of this nuclide is produced by cosmogenic muons through a reaction resulting in the emission of free neutrons:

$$\mu + {}^{12}C \rightarrow \mu + {}^{11}C + n\cdot \tag{2.5}$$

Consequently, ^{11}C decays with a mean life $\tau = 29.4$ min via positron emission:

$$^{11}C \rightarrow {}^{11}B + e^{+} + \nu_{e}. \tag{2.6}$$

The total energy released in the detector is between 1.02 and 1.98 MeV (β^{+} with Q–value of 0.96 MeV plus 2×0.511 MeV γ–rays from e^{+} annihilation) and lies in the energy region of interest for the detection of electron recoils from *pep* neutrinos. In the Borexino scintillator, neutrons (produced also together with ^{11}C, see Eq. 2.5) are captured with a mean lifetime of (254.5 $\pm$ 1.8) μs [13]) on Hydrogen, producing characteristic 2.22 MeV γ rays. The muon flux in the underground laboratory is about 1.2 $\mu m^{-2} h^{-1}$ that produce (30 $\pm$ 5) cpd/100ton. This element is produced continuously by spallation of ^{12}C by mean of cosmic muons, therefore is not possible perform a filtering operations to reduce its contribution into the spectrum. Instead, a very powerful method is by means of software tagging veto on ^{11}C events, by using the time and spatial coincidence of reaction chains described in Eqs.2.5, 2.6 after the muon event.
Within the detector are produce also several light radioactive elements from muon transition, their residual counts after a temporal cut of 300 ms, summarized in Tab.2.2, are negligible with respect to other backgrounds.

^{210}Pb

^{210}Pb is a β–emitter in the ^{238}U decay chain. Due to its long half–life (22 years) and tendency to adsorb on to surfaces, it is often found out of the secular equilibrium with the ^{222}Rn section of the chain above it. While ^{210}Pb itself is not a problem, since its end–point (Q–value = 63.5 keV) is well below the energy region of interest for solar neutrinos, its daughters, ^{210}Bi and ^{210}Po, are a major source of background in Borexino.

^{210}Bi

^{210}Bi is a β emitting daughter of ^{210}Pb with 5 days half–life. Its spectrum (Q–value = 1.16 MeV) spans through the energy range of interest for both ^{7}Be and *pep* – CNO solar neutrinos and it does not exhibit any specific signature (except its spectral shape)

Isotope	Q–value (E_γ) [MeV]	Residual rate [cpd/100tons]	rate at 1.44 MeV [cpd/100tons/MeV]
n	2.22	< 0.005	0
^{12}B	13.4	$(7.1 \pm 0.2) \times 10^{-5}$	$(2.49 \pm 0.07) \times 10^{-6}$
^{8}He	10.6	0.004 ± 0.002	$(2.6 \pm 1.2) \times 10^{-4}$
^{9}C	16.5	0.020 ± 0.006	$(1.6 \pm 0.5) \times 10^{-3}$
^{9}Li	13.6	0.022 ± 0.002	$(1.4 \pm 0.1) \times 10^{-3}$
^{8}B	18.0	0.21 ± 0.05	0.017 ± 0.004
^{6}He	3.5	0.31 ± 0.04	0.15 ± 0.02
^{8}Li	16.0	0.31 ± 0.05	0.011 ± 0.002
^{11}Be	11.5	0.034 ± 0.006	$(3.2 \pm 0.5) \times 10^{-3}$
^{10}C	3.6	0.54 ± 0.04	0
^{7}Be	0.48	0.36 ± 0.05	0

Table 2.2: Expected rates of cosmogenic backgrounds considering the 300 ms cut performed after every muon.

that would help its identification. The ^{210}Bi is measured only through the spectral fit. At the start of data taking, following the initial filling of the detector, the ^{210}Bi rate obtained through the spectral fit was (10 ± 6) cpd/100 tons. However, over time, the ^{210}Bi contamination has been steadily increasing and at the start of May 2010 the rate was $\simeq$75 cpd/100 tons. The reason for this increase is not currently fully understood but it seems correlated with operations performed on the detector and the possible convective motion due to temperature variation that picked up from nylon surface this element putting in the center of detector.

The Empirical Mode Decomposition introduced in the next sections, seems to be able to extract the time function (also called *"trend"*) that describe the time variation of this background (see Figs.2.5 a and b).

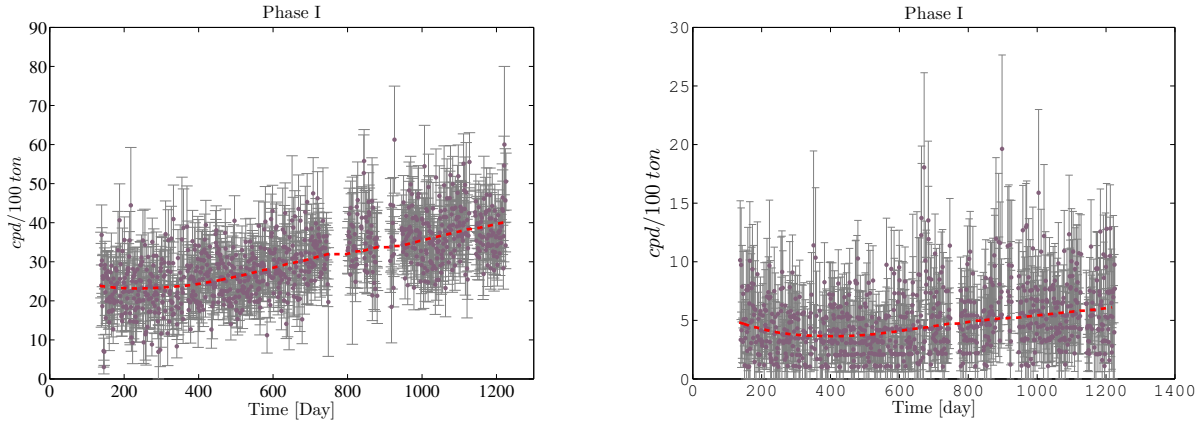

(a) a

(b) b

Figure 2.5: In figure a we observe the ^{210}Bi trend observed in the so called Be7 shoulder energy window (145-380 npe). The same trend have been observed in the so called Bismuth valley energy region (390-450 npe) populated mainly from ^{210}Bi events.

^{210}Po

^{210}Po is a mono–energetic 5.3 MeV α emitter (138 days half–life) but the strong ionization quenching of the scintillator brings its spectrum in the ^{7}Be energy region. It is produced in at final steps of Radon chain as daughter of ^{210}Bi but its concentration is much more larger than the ^{210}Bi maybe because of contamination in the pipes of storage plants. The contamination from the plant is visible each time some operation are done on the liquid scintillator as shown in the time variation of the count rates in Fig.2.6. The pulse shape of α-decay emitted from this element is more larger than the usual β-event. This offers a way to distinguish with a certain approximation by means of pulse shape discrimination defining a new parameter called Gatti's parameter that we will discuss later in the next section. By mean of this parameter has been possible to follow the spatial distribution of alpha events during the three year of data taking, observing a slow mixing effect, related to convective motions, that could explain also some fluctuation in the data for the seasonal analysis.

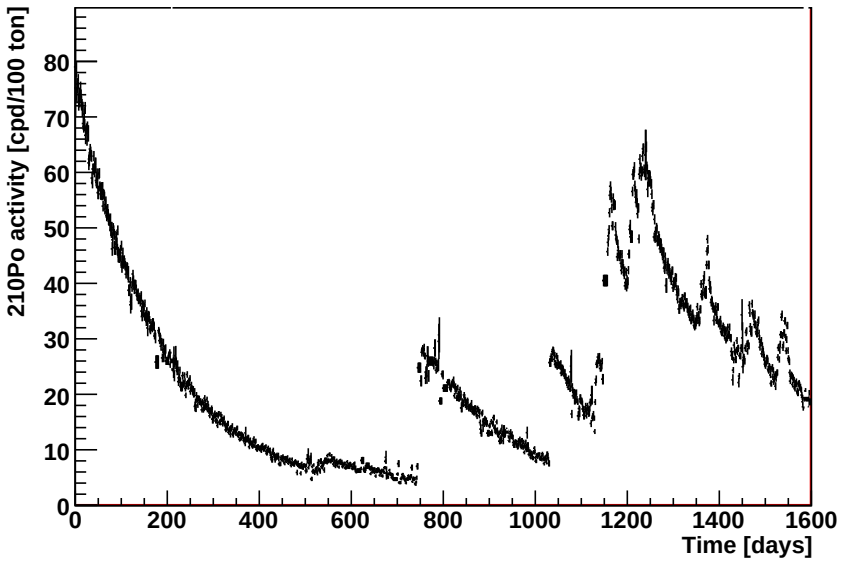

Figure 2.6: Time variation of ^{210}Po count rates during 5 years of data taking. Are well visible the strong increases of count rates during the refilling or water extraction operations performed between 2009-2011 and also the exponential shape of the decay.

^{85}Kr

The isotope ^{85}Kr is a β–emitter with 0.687 MeV end–point (99.57% branching ratio) and 10.7 years half–life. Its spectral shape is very similar to the ^{7}Be recoil spectrum and it is one of the most important backgrounds in the ^{7}Be analysis. It is present in air at the average concentration of $\sim$1 Bq/m^3 thus even extremely small air exposures during the filling operations could give rise to a significant contamination in the scintillator. With the small branching ratio of 0.43%, ^{85}Kr decays into the meta–stable ^{85m}Rb emitting a β particle with maximum kinetic energy of 173 keV. The ^{85m}Rb then decays to the ground state ^{85}Rb by emitting a 514 keV γ ray with 1.46 μs half–life. This fast $\beta - \gamma$ sequence is the signature used to obtain a measure of the ^{85}Kr concentration independent from the one resulting from the spectral fit. Performing a measurements by mean of identification of ^{85}Kr decay coincidence [108], we observe 29.9 net events in 750 days and in a FV of 156.2 tons ($R < 3.5$ m) correspond to a ^{85}Kr contamination of (30.4 $\pm$ 5.3 (stat) $\pm$ 1.5 (syst)) cpd/100 tons where the systematic error is mostly coming from the FV definition and the efficiency of ^{85}Kr–β energy cut.

^{232}Th

^{232}Th is a primordial isotope with a half-life of 14 billion years and a abundance of 100%. The main decays branches of the ^{232}Th include 6 α and 4 β decays. The fast decays sequence $^{212}Bi \rightarrow ^{212}Po + e^- + \bar{\nu}_e$, $^{212}Po \rightarrow ^{208}Pb + \alpha$ (τ= 433 ns) allows to estimate the ^{220}Rn (thoron) content of the scintillator and, as before, to infer the ^{232}Th contamination. The ^{212}Bi is a β emitter with Q=2.252 MeV and the α of ^{212}Po decay has 8.955 MeV energy. The $^{212}Bi - ^{212}Po$ events are selected within gates having two clusters surviving the muon cut and reconstructed with a distance of 1 m and a time delay between 400 ns and 1732 μs (four times the lifetime of the decay). The 400 ns value ensures that the efficiency of the clustering algorithm is 100 % at the energies of interest.

The energy region of the first candidate is selected to be ¡ 2.4 MeV and that of the second one is required to be in the range 0.9-1.3 MeV. The cut efficiency is 34%. The mean counting rate of the events reconstructed within a sphere of 3.3 m radius during periods far from any detector operation (611 days of lifetime) is (0.13 ± 0.03) cpd/100 tons and it corresponds to a scintillator ^{232}Th contamination of $(3.8 \pm 0.8) \cdot 10^{-18} g/g$ at equilibrium.

2.4 Scintillator Properties

The Organic liquid scintillator used as sensitive material in Borexino detector has a benzene ring structure. The real target for the neutrinos are the electrons of this liquid scintillator that, if hit by a neutrino or emitted by mean of a β-decay, it travels in the liquid scintillator exciting the valence electrons of the orbitals π and σ of the benzene rings. The scintillation light emission is due to the transition from the excited level to the ground state of the π electrons. The de-excitation of the σ electrons occurring by means of thermal process.

The excited electrons can lead to single or triplet states. The singlets states have a 1 eV as separation in energy, instead the vibrational state around 0.15 eV. When excited the state fall back in lower states (for example from the singlet state $S_{12} \rightarrow S_{10}$) with

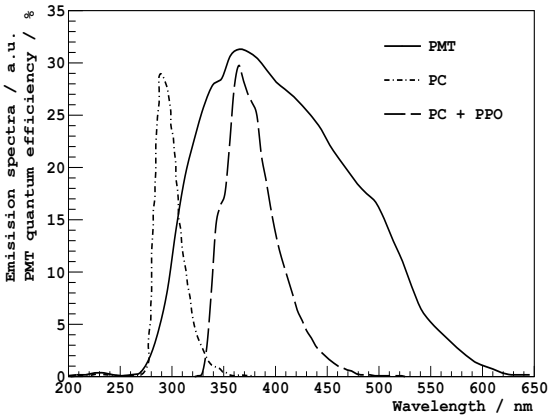

Figure 2.7: Mean darknoise rate per PMT in counts per second as a function of time starting from May 16th, 2007.

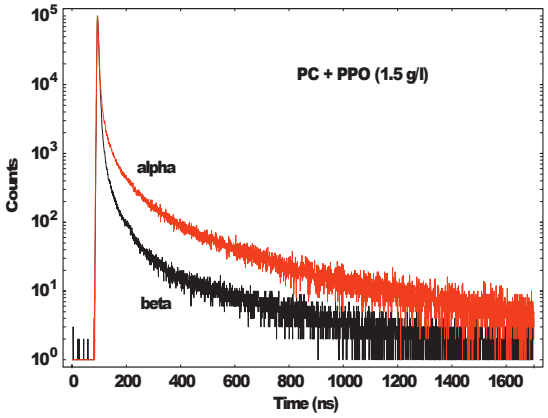

Figure 2.8: Example of a data acquisition gate with two separated clusters.

a time scale of 1–10 ns by so called *fluorescence* process that is the main scintillation process.

The triplet states have longer time scale by mean of phosphorescence process with time scale of the 1–10 ms, but the wavelengths of photons emitted are longer than the fluorescence emissions, therefore are not relevant in the scintillation process. Some time two triplet states can recombine in two singlet states performing the florescence process, also called delayed florescence that is the responsible of the larger pulse shape of α-like events.

In order to shift the wavelength of photons at lower values (higher frequency), in which the PMTs have the maximum of the sensitivity, together with the pseudocumene, PC (1,2,4-trimethylbenzene, $C_6\,H_3\,(CH_3)_3$), has been added the PPO (2,5-diphenyloxazole, $C_{15}\,H_{11}NO$) with a concentration of 1.5 g/l. With this concentration the PPO increase the light emission of a factor of 20 time, with respect to the PC. This correspond to a light yield equivalent of 500 photoelectrons at 1 MeV, with a energy resolution of 5% at 1MeV.

2.4.1 Quenching Effects

In order to define a relation between the energy deposited by the charged particles and the light emitted by the molecules, we have to take into account all possible processes with which the molecules can dissipate their exciting energy, in which the light emission is just one of several ways. For example the non radiative recombination processes are function of ionized molecules, therefore they occur much more often for those particles with a large value for $\mathrm{d}E/\mathrm{d}x$. These are called *"quenching effects"* and are responsible for the reduction of the deposited energy down to the energy one actually observes. For α particles in Borexino, the observed number of photons is approximately less than 10% of that expected from an equal energy β. To describe the non linear processes, to convert the deposited energies in emitted light, Borexino use the Birks parametrization [6, 7], in which the light emission per unit length, depend on energy loss by means of two parameters in according with the semi-empirical relation:

$$\frac{\mathrm{d}L}{\mathrm{d}x} = \frac{Ly\frac{\mathrm{d}E}{\mathrm{d}x}}{1 + kB\frac{\mathrm{d}E}{\mathrm{d}x}} \tag{2.7}$$

where Ly is the light yield or absolute scintillation efficiency that is defined as the fraction of incident energy converted to the photons. $kB \cdot \frac{\mathrm{d}E}{\mathrm{d}x}$ is the density of the ionized molecules along the track and k is the fraction of these that undergo in quenching effects. The kB parameter is called Birks parameter and is treated as a single parameter characteristic of the liquid scintillator used and must empirically determined, but is the same for different type of particle [8]. In Borexino, the scintillator light yield is of the order of 10000 photons/MeV. The values estimated for kB in Borexino internal note ranging from $kB \simeq 0.015 cm/MeV$ in the laboratory test to $kB \simeq 0.010 cm/MeV$ in CTF[1] data.

[1]Counting Test Facility (CTF) was the first prototype of Borexino experiment. Now in the same water tank it is going to build a new DarkSide50 experiment for Dark Matter Search

2.5 Acquisition System and Event Reconstruction

2.5.1 Electronics and Data Acquisition System

What Borexino observe is the light emitted from each event occurred inside the Inner Vessel and the arrival time of the photons to each PMT (*photomultiplier* or photo-tube). Every PMTs are AC coupled[2] to an electronic chain realized by an analog front–end followed by a digital circuit. The Borexino trigger fires when a minimum number of PMTs are hit at least one photo-electron within a time window of 100 ns. Typically, K was set in the range 25 to 30 in the data runs considered, corresponding approximately to an energy threshold ranging between 50 and 60 keV. In case of trigger, the time and the charge of each hit detected in a time gate of predefined length are acquired and stored. Initially, in the first months of operation, the gate length was 7.2 μs and later was enlarged to 16 μs. The dead time between two consecutive gates is 1.2 μs. The hit time is measured by a Time to Digital Converter (TDC) with about 0.5 ns resolution which is smaller than the intrinsic 1 ns time jitter of the PMTs. A dedicated sub-ns 394 nm pulsed laser system is used to equalize the time response of all the PMTs [17] via a set of optical fibers that reach every PMT. The typical accuracy of the time equalization is better than 0.5 ns and the time calibration procedure is performed at least once a week. A similar system based on a set of LEDs is employed for the outer detector. The dark noise rate is typically 400 - 500 kHz originating on average 15 hits in the 16 μs acquisition gate (see Fig. 2.9.a). A proper software (called clustering algorithm) recognizes within the gate the group of hits belonging to a single scintillation event (here called clustered hits). The cluster duration is 1.5 μs. Fast radioactive decays or random coincident events detected in a single trigger gate are separated by the clustering algorithm. Delayed coincidences separated by more than the gate width (16 (7.2) μs) are detected in two separate events. Figure 2.10.b shows an event with two clusters. A dedicated trigger was developed for cosmogenic neutron detection. After each muon passing and triggering both the OD and the ID, a 1.6 ms wide acquisition gate is opened, regardless of the neutron presence. This

[2]Both signal and High Voltage of power supply travel on the same cable

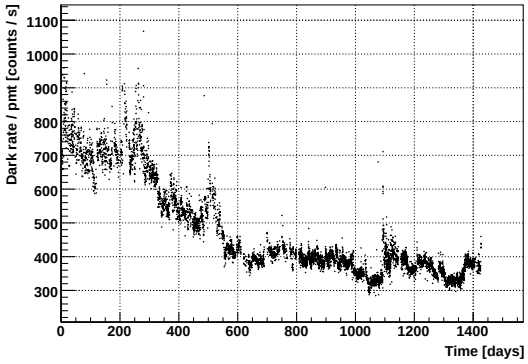

Figure 2.9: Mean darknoise rate per PMT in counts per second as a function of time starting from May 16th, 2007.

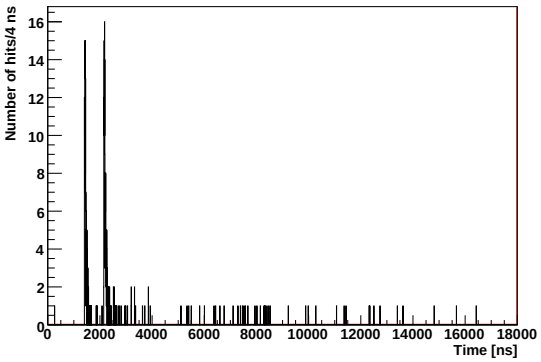

Figure 2.10: Example of a data acquisition gate with two separated clusters.

length is sufficient since it corresponds to more than six times the neutron capture time. Neutrons are searched for as clusters in this dedicated long trigger as well as clusters within the muon gate itself. The dead–time between the muon and neutron trigger is (150 ± 50) ns. More details about the neutron detection can be found in [13].

2.5.2 Energy Reconstruction

Borexino works mainly in the single photoelectron regime, therefore each PMT detects mostly a single or just a few hits in a single event. We define four energy estimators called N_p, N_h, N_{pe}, and N_{pe}^d. The N_p variable is the number of the PMTs detecting at least one hit, while the N_h is the total number of detected hits taking into account the channel dead time already discussed above. They are computed starting from the measured values N_p^{meas} and N_h^{meas}

$$N_p^{meas} = \sum_{j=1}^{N'} p_j \tag{2.8}$$

$$N_h^{meas} = \sum_{j=1}^{N'} h_j \tag{2.9}$$

where p_j can only be 0 or 1 while h_j can assume the values 0 or 1, 2,...n if the photomultiplier j detects 1, 2,...n hits and N' is the number of correctly working channels. N' is smaller than the total number of installed PMTs because of temporary electronics

problems and due to the PMT failures. N' is evaluated at nearly event–by–event basis based on the laser calibration events acquired during the run. The N_p and N_h variables are then obtained after normalizing the measured values to $N_{tot} = 2000$ working channels through the relations:

$$N_p = \frac{N_{tot}}{N'(t)} N_p^{meas} = f_{eq}(t) N_p^{meas} \tag{2.10}$$

$$N_h = \frac{N_{tot}}{N'(t)} N_h^{meas} = f_{eq}(t) N_h^{meas} \tag{2.11}$$

in which the time dependent equalization function $f_{eq}(t)$ is defined as $f_{eq}(t) = \frac{N_{tot}}{N'(t)}$. The third energy variable, N_{pe}, is the total number of photoelectrons (pe) collected within the clustered hits. First, the mean position of the single photoelectron for each channel is determined as described in the next section. When an event occurs, the total charge output from each PMT is integrated for 80 ns and digitized. The estimated number of photoelectrons (ratio of the integrated total charge to single photoelectron mean) is then summed over all the channels to get N_{pe}^{meas} and then the normalization to N_{tot} working channels is performed:

$$N_{pe}^{meas} = \sum_{j=1}^{N''} \frac{C_j^{ADC}}{C_j^{Peak}} \tag{2.12}$$

$$N_{pe} = \frac{N_{tot}}{N''(t)} N_{pe}^{meas} = c_{eq}(t) N_{pe}^{meas} \tag{2.13}$$

where C_j^{ADC} is the ADC channel corresponding to the measured charge of the PMT j and C_j^{Peak} is the ADC channel corresponding to the single photoelectron peak of the same PMT; N'' is the number of channels with valid charge data. We note that the number of channels with working ADC's and charge readout is normally fewer than N' by a few tens of channels; $c_{eq}(t)$ is a time dependent charge equalization function defined within Eq. 2.13.

An additional variable similar to N_{pe} but calculated subtracting the total number of hits due to dark noise during the signal duration is also used: it is an estimate of the true number of photoelectrons produced during each event. We call this variable N_{pe}^d and it is defined as:

$$N_{pe}^d = c_{eq}(t) \left(\sum_{j=1}^{N''} \frac{C_j^{ADC}}{C_j^{Peak}} - d \right) \tag{2.14}$$

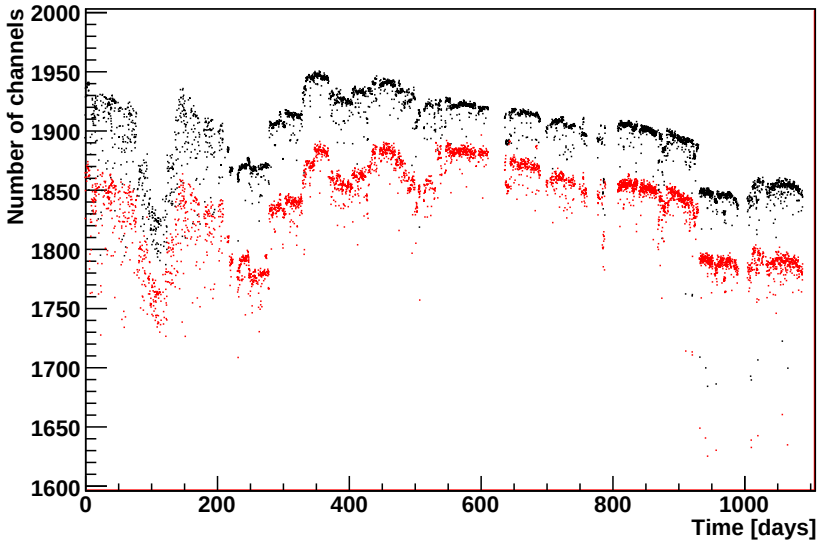

Figure 2.11: The number N' (black) and N'' (red) of available channels for the computation of $N_h(N_p)$ and N_{pe} energy estimators, respectively, as a function of time starting from May 16th, 2007 (day0).

We note that for the purposes of noise reduction, we also define an additional variable N_{pe-avg} which only differs from N_{pe} in which the sum is carried over all usable channels N' for which a correct charge measurement is not required. For those channels that do not have a working ADC or charge readout, the charge is estimated as the average charge of all other (valid) hits in a 15 ns window around the hit. Figure 2.11 shows N' and N'' as a function of time during the data taking. The different estimators are not independent and the precise relation between them and the true energy deposit inside the scintillator is one of the key elements determining the accuracy of the solar neutrino measurement in Borexino. Note that in the energy region of interest in this paper the two estimators N_p and N_h are very similar.

2.5.3 Position reconstruction

The position reconstruction algorithm uses the photon time arrive at the first PMT $(r_j,\, t_1^j)$ where $\vec{r}_j$ is the position vector of the j^{th} PMT which detected its proper first hit at the time t_1^j (note that each hit PMT can detect more than one photoelectron

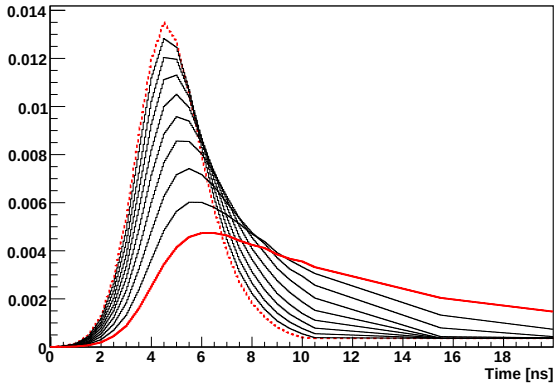

Figure 2.12: Emission probability density functions for scintillation photons for increasing values of the charge collected at the phototubes: from a minimum of 1 photoelectron (red solid curve) to a maximum of 10 photoelectrons (red dashed curve).

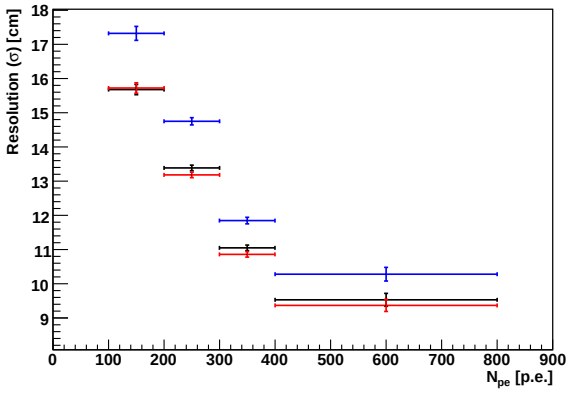

Figure 2.13: Resolution (σ) of the reconstructed x (red), y (black), and z (blue) coordinates as a function of energy (in number of photoelectrons). This was obtained for calibration source events located in the center of the detector.

during the same event).

The algorithm subtracts from each measured time t_1^j a position dependent time–of–flight T_{flight}^j

$$T_{flight}^j(\vec{r}_0, \vec{r}_j) = \mid \vec{r}_0 - \vec{r}_j \mid \frac{n_{eff}}{c} \tag{2.15}$$

and then it maximizes the likelihood

$$\mathcal{L}_E(\vec{r}_0, t_0 \mid (\vec{r}_j, t_1^j)) = -\sum_{j=1}^{N_{\text{hits}}} \log\left[\text{pdf}_q\left(\frac{|\vec{r}_0 - \vec{r}_j|}{c/n_{eff}} - (t^j + t_0)\right)\right] \tag{2.16}$$

providing the position $\vec{r}_0$ and time t_0 of the event. The quantity n_{eff} is called effective refraction index and it is used to define an effective velocity of the photons. It is a single parameter that globally takes into account the fact that photons with different wavelengths travel with different group velocity and that photons do not go straight from the emission to the detection points but they can be scattered or reflected. The value $n_{eff} = 1.68$ was determined using the calibration data [93]. Note that n_{eff} is larger than the actual index of refraction of pseudocumene measured at 600 nm to be $n_{\text{PC}} = 1.50$. The pdf_q in the likelihood is the probability density function that the scintillator emits a photon at a time between t and $t + dt$ for a given total number of detected photoelectrons. $\mathcal{L}_E$ depends on the energy of the event as Fig. 2.12 shows. The

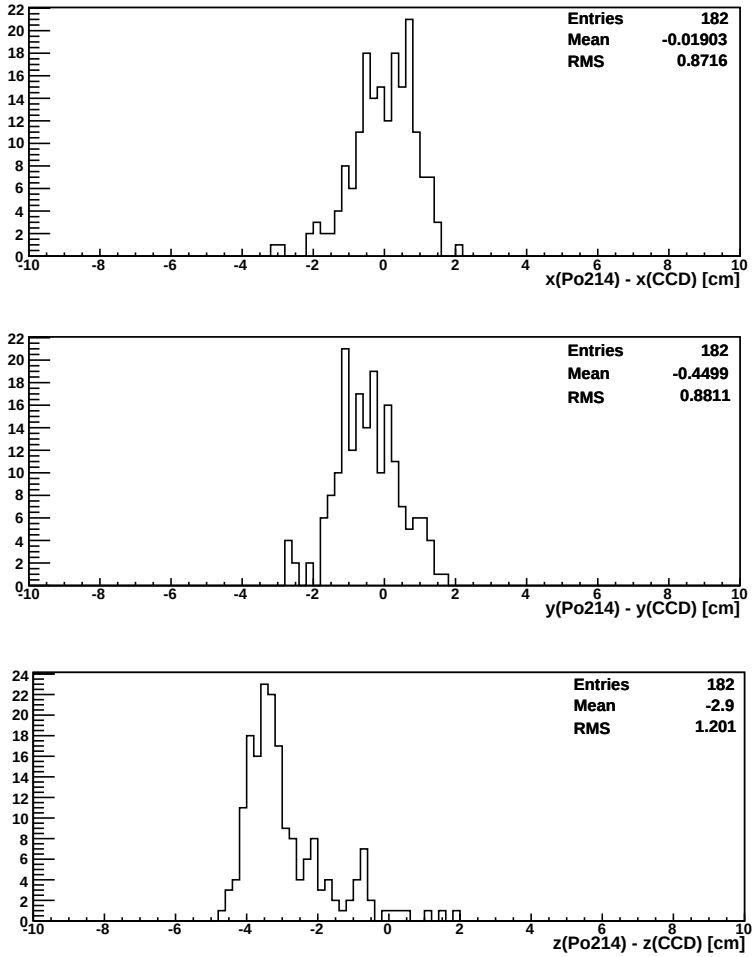

Figure 2.14: Difference of the reconstructed (^{214}Po) and nominal (CCD) coordinates x (top), y (center) and z (bottom) for the radon source data.

data collected during the calibration campaign has allowed to map in a capillary way the performance of the position reconstruction code as a function of energy and position. In particular, the position reconstruction resolution ($\sigma_{\vec{r}_0}$) has been studied for different energies and positions. As an example, Fig. 2.13 shows the dependency of $\sigma_{\vec{r}_0}$ on energy for events in the center: the resolution for coordinates x and y ranges from 15 cm at lower energies ($\simeq$150 photoelectrons corresponding to approximately 300 keV) to 9 cm at higher energies ($\simeq$500 photoelectrons corresponding to approximately 1 MeV). The z coordinate is reconstructed with a slightly worse resolution as expected since the phototube coverage in z has a larger granularity. The nominal and reconstructed

source position have been compared for all the collected calibration data. The nominal position of the source is obtained independently by a system of 7 CCD cameras mounted on the Stainless Steel Sphere. Figure 2.14 shows, as an example, the difference between the mean value of the reconstructed coordinate x, y, and z and the corresponding nominal value for events due to ^{214}Po alphas from the Rn chain. The coordinates x and y are well reconstructed: the sigma of the distribution is ~ 0.8 cm with tails which extend at maximum to 3 cm (note that the contribution of the uncertainty on the CCD position contributes is not disentangled). The z–coordinate shows instead a systematic shift of $\sim$3 cm downwards with respect to the nominal position. The origin of this shift is unclear: it is not related to the algorithm itself, since the reconstruction of Monte Carlo simulated data doesn't show the same effect. It could be due to a small variation of the index of refraction as a function of z due to the gradient in temperature (and therefore in density) of the scintillator. In any case, the contribution of this shift to the systematics of the fiducial volume determination is negligible (less than 0.2 %)

2.5.4 Inner Vessel Shape Reconstruction

In the ^7Be neutrino analysis we used a rigid fiducial volume (FV) defined by means of events position reconstruction in the Cartesian coordinates where the zero point of axises are posed in the center of detector. To select the events inside the fiducial volume was done a simply selection on event position defining a radius $r = 3.21$ m and performing two cuts at $z = \pm 1.67\, m$. This method defines a *rigid* fiducial volume in the center of detector shown in Fig.2.15 with dashed blue line. Unfortunately, after the leak occurred on the April of 2008, the shape of IV has not been constant in time, losing its original spherical shape. The maximum deformation is present in dataset taken between January and March 2009, when it was stabilized with several refilling operations using new PC (Pseudocumene) and purifying the buffer [16].
In the neutrino ^7Be analysis this problem was not much important because the dimension of FV was more than 1 meter far from the vessel surface ($r_{FV} = 3.021m$ and $r_{IV} = 4.25m$), then also in the case of maximum deformation of the vessel ($40\, cm$ with respect to the initial position) the effects were negligible.

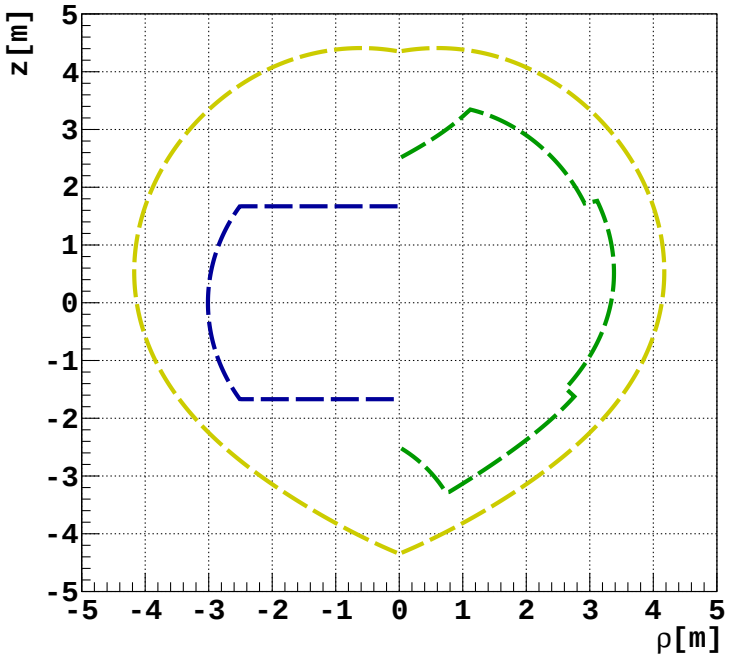

Figure 2.15: Fiducial volumes and shape of inner vessel. The dashed blue line is the Standard FV selected for the Be7 neutrino analysis, the dashed green line is the last FV selected for the Seasonal analysis.

In order to define a new bigger Fiducial Volume (FV), as request to increase the statistics in case of Seasonal Variation Analysis (SVA) of ν ^{7}Be or in the case of geo-neutrinos flux measurement, we will have to define a new algorithm to locate the surface of inner vessel (IV) in Borexino experiment for each weekly data set (named DST).

To identify the position of IV, we can use the background events of Bismuth (^{210}Bi) present in large quantity on nylon of inner vessel.

We select a window energy in which are present mainly the Bismuth events, also called "Be7-valley", between $390 - 450$ *npe* in `m4charge_noavg` or, as in the case of variable used for the data selection `m4s.laben__hitdist__npe_aver_corrected`, between $290 - 350$ *npe*.

In Fig.2.16 we show the time evolution of counts in different energy window candidates to identify the vessel profile. Although in order to define the shape of vessel the energy window of external background (peak energy $E_{^{208}Tl} = 2.6$ MeV) is the best one, there

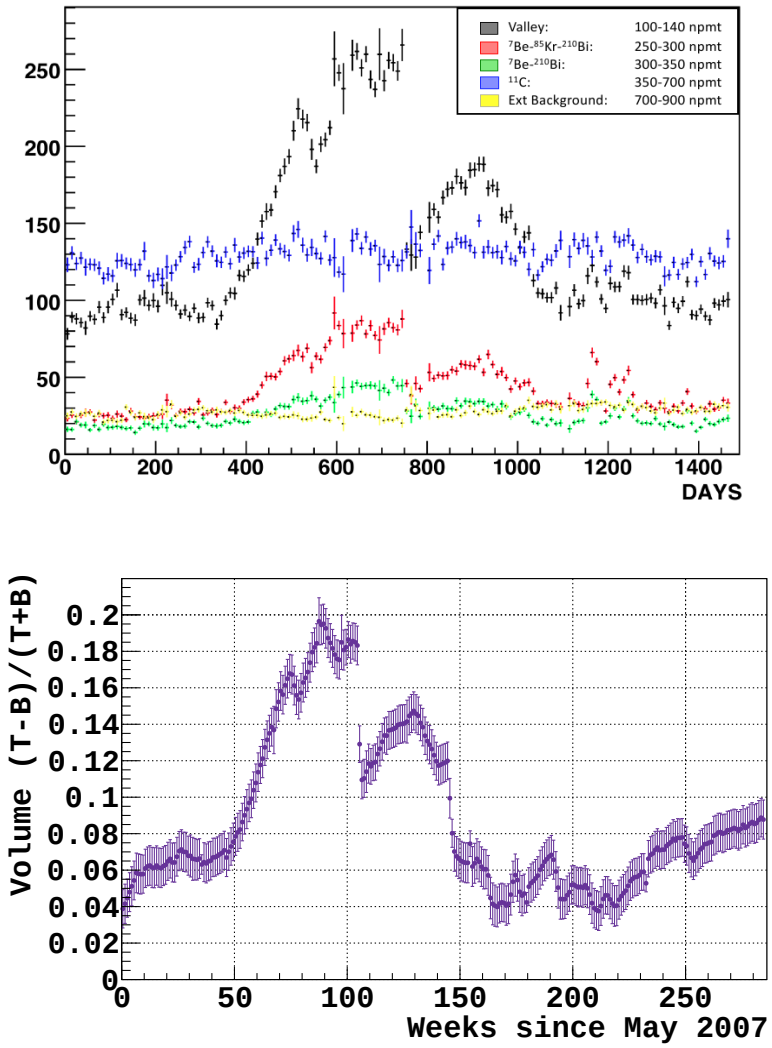

Figure 2.16: Time evolution of different energy windows with radius cut to $r = 4$ m and energy variable `m4s.laben__hitdist__npe_aver_corrected`. Comparing the counts rate of the low energy windows (from ^{14}C to ^{210}Bi-valley) with the difference between the volume of top and bottom half of total volume, we observe a strong correlation. This effect shows the real contribute to the distortion of data is provided by vessel shape deformations.

is in a little number of events; also summing the data of three DSTs as we are doing in this method.

Another potentially useful energy window, could be the so-called "^{14}C-valley" between two peaks of ^{14}C and ^{210}Po. Once given the high number of data we could identify the vessel shape even run by run. The problem, in this case, is that the spatial resolution

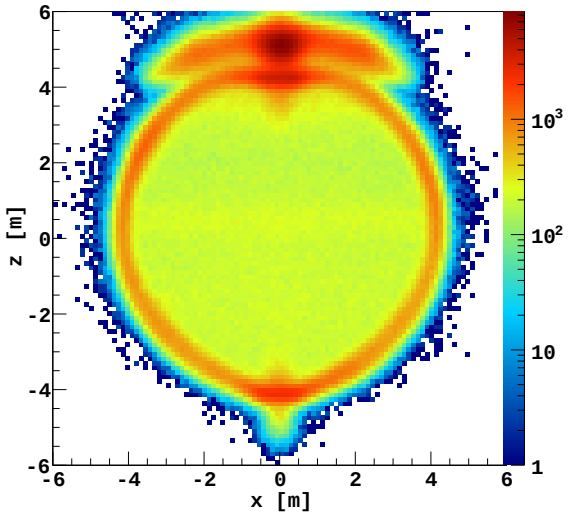

Figure 2.17: Radial distribution for ^{14}C events in energy range taken only in one run using a *y-slice* $(-0.50; 0.50)$ m included.

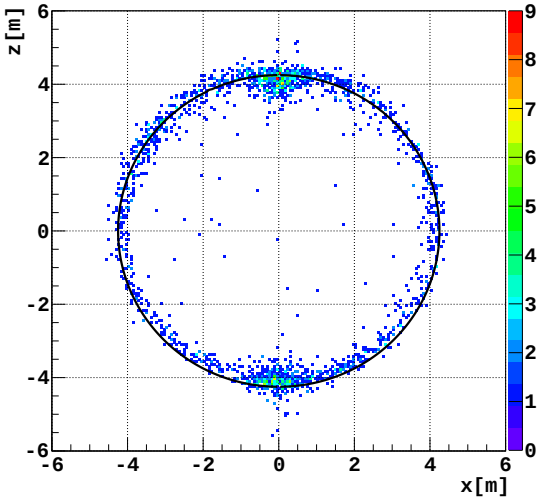

Figure 2.18: Radial distribution for ^{210}Bi events in energy range between $290 - 350$ npe. It is possible to see as the Bismuth defines very well the contour of vessel that is shifted toward the top side of the nominal position.

is too low to obtain information about the vessel profile, as showed in Fig.2.17.

Finally, the range of energy in which it is possible to see the vessel profile with a good spatial resolution, it is the Bismuth valley.

Summing the data of three DSTs, we obtain the profile showed in Fig.2.18.

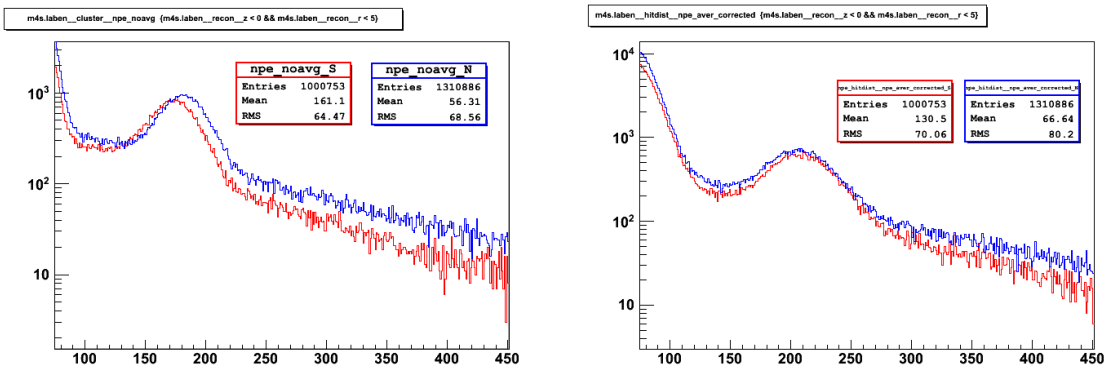

(a) `m4s.laben__cluster__npe_noavg` (b) `m4s.laben__hitdist__npe_aver_corrected`

Figure 2.19: In the figure a) we show the difference between Top (*Blue line*) and Bottom (*Red line*) region of detector using the charge variable of ^7Be. We can observe that there is a shift in Light Yield between Top and Bottom region. In Figure b) we can see the same data, but in *"hitdist"* variable. In this case the shift is negligible or absent.

In order to select the data, before to do a selection in energy, we performed these preliminary cuts:

- `m4s.laben__recon__valid` $== 1$;
- `m4s.muon_num_events` < 25;
- $3.4\,m > r > 7.0\,m$;
- therefore the energy selection:
  $290npe <$`m4s.laben__hitdist__npe_aver_corrected`$< 350npe$ (Bismuth valley).

The choice of the energy variable `m4s.laben__hitdist__npe_aver_corrected` it is due to its response stability between Top and Bottom side of detector.
At the end of the cuts, we plot the data on a 2D histogram with the radial position of each event given by $r = \sqrt{x_i^2 + y_i^2 + z_i^2}$ vs. the angle between the "z-axis" and the "*radius*" $\theta = \arccos(z/r)$ as it is showed in Fig.2.20.
The 3D-histogram shows the morphology of data distribution (figs.2.20.b and 2.20.d). From these two kinds of distributions we can start to make a fit of data, using a two-dimensional function $R_{shape}(\theta)$.

Normal case without leak

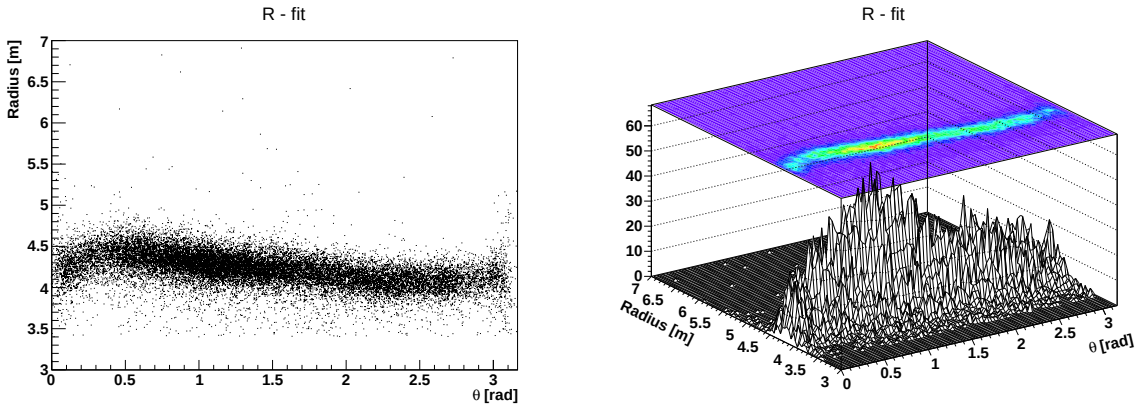

(a) 2D-View (b) 3D-View

Leak case with maximum of luminosity of leak

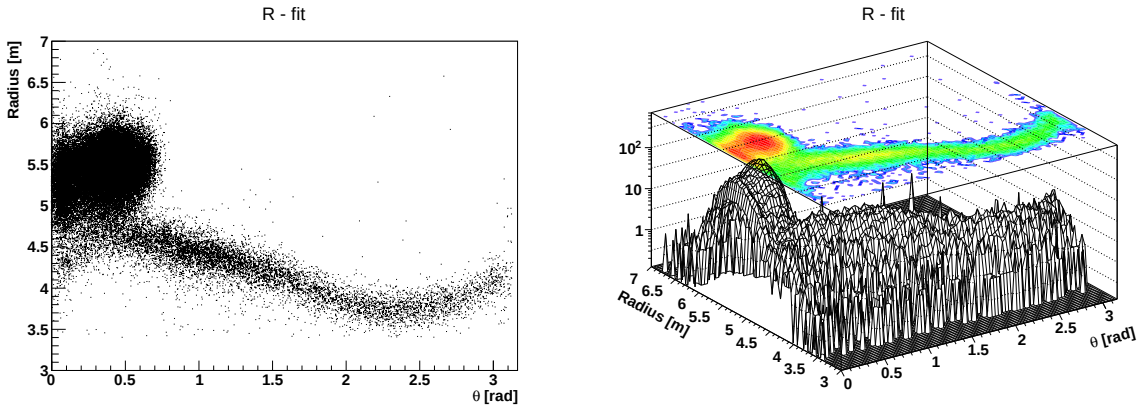

(c) 2D-View (d) 3D-View

Figure 2.20: In the figure a) and b) we show the 2-dimensional and 3-dimensional histograms with the events surviving to the cuts that draw the contour of the nylon vessel in the standard case. At radius larger than 4.7 m we are in the buffer region where the scintillation it is quenched by dimethylphthalate (DMP) with a concentration of about $2g/l$. In figure c) and d) we show the same histograms in the case of maximum deformation of vessel where is present also the leak at its maximum luminosity. This blob of events is due to the leak of liquid scintillator in the buffer region and could be represented by a two-dimensional Gaussian function.

In a general slice $R(\theta_i)$ of this distribution, we have that the event profile crosses the nylon of the vessel like a Gaussian distribution showed in fig.2.21.a Because of the leakage at top side of detector ($\theta \sim 0°$) we observe two possible situations: the scintillating counts rate in the buffer region are dominants with respect to the ^{210}Bi on the nylon vessel (fig.2.21.b), or the two peaks are well separate (fig.2.21.c). Therefore

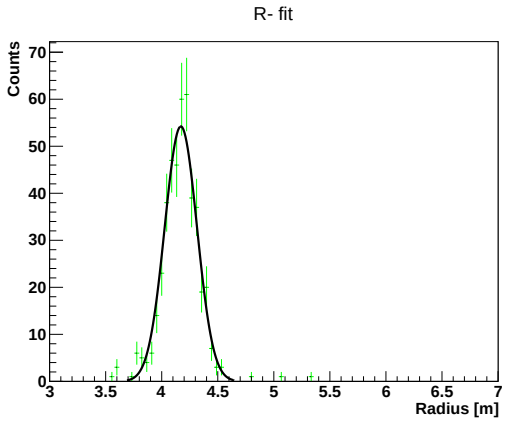

(a) Single Gaussian Function

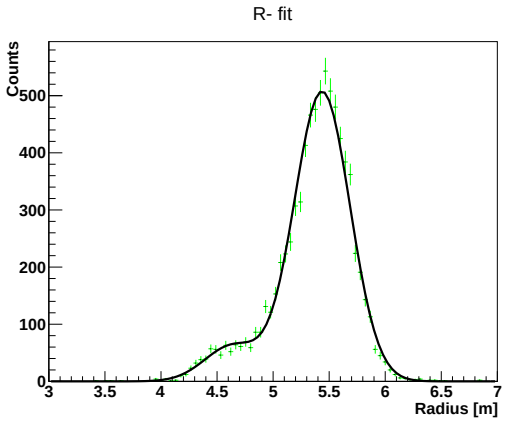

(b) Double Gaussian Function with overlapping

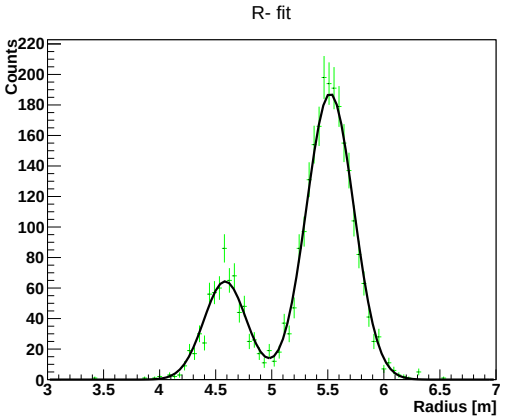

(c) Double Gaussian Function separate

Figure 2.21: These are two general sections at the angle θ_i (a) and at angle $\theta < 30°$ (b) of distribution of events fitted by Gaussian function.

to locate the profile of vessel, we have to use a 2-dimensional function and then we have to add another Gaussian to reproduce the leak distribution.

Finally, in order to define a vessel profile, we used a Fourier-like expansion in which we set the boundary conditions:

$$R_{shape}(0) = R_{shape}(\pi) = 4.25\, m. \tag{2.17}$$

This constraint it is very important, because the positions of two end-points of the vessel are two well known points.

The function used to perform the fit is the following:

$$R_{shape}(r,\theta) = N_0(\theta)\exp\left[\frac{(r-\mu(\theta))^2}{\sigma^2(\theta)}\right] + \sum_{i=1}^{2} G_i(r,\theta) \tag{2.18}$$

where r and θ are positions of each event on histogram plane, $N_0(\theta)$ is normalization factor defined as a $3th$-degree polynomial on θ, $G_i(r,\theta)$ are two bi-dimensional Gaussian functions[3], $\sigma(\theta)$ it is a linear function on θ:

$$\sigma(\theta) = \sigma_0 + \sigma_{01}\cdot\theta \tag{2.19}$$

where σ_{01} it's very small ($\sim 10^{-4}\,m$).
Finally the function $\mu(\theta)$ is defined as:

$$\mu(\theta) = R_0 + A_1\cos\left(\frac{\theta}{2}\right) + B_1\sin\left(\frac{\theta}{2}\right) + \sum_{n=2}^{5}\left(a_n\cos\left(n\frac{\theta}{2}\right) + b_n\sin\left(n\frac{\theta}{2}\right)\right) \tag{2.20}$$

where $R_0 = 4.25\,m$, A_1 and B_1 are defined as:

$$A_1 = -a_2 - a_3 - a_4 - a_5 \;\text{ and }\; B_1 = a_2 - a_4 + b_3 - b_5. \tag{2.21}$$

in which a_n and b_n are the coefficients of the Fourier series.
In Fig.2.22 we show the results of the fit with this function. In the case where the leak is not present the two-dimensional Gaussian functions was switched off by using only the first term of eq.2.18.
In order to perform the fit, we defined a χ^2_{Tot} function as follow:

$$\chi^2_{Tot} = \chi^2 + \frac{(\pi R_0 - L_{IV})^2}{\sigma_R^2} \tag{2.22}$$

where the second term in the right-hand side of the equation is a penalty term that take into account the inextensibility of the vessel balloon. The L_{IV} is the length of balloon profile of Inner Vessel, defined as:

$$L_{IV} = \int_0^{\pi} d\theta\sqrt{\left(\frac{dR(\theta)}{d\theta}\right)^2 + R^2(\theta)}. \tag{2.23}$$

[3]two of these functions are necessary only in case of `dst_2009_Jan_25` where is present a double peak.

Normal case without leak

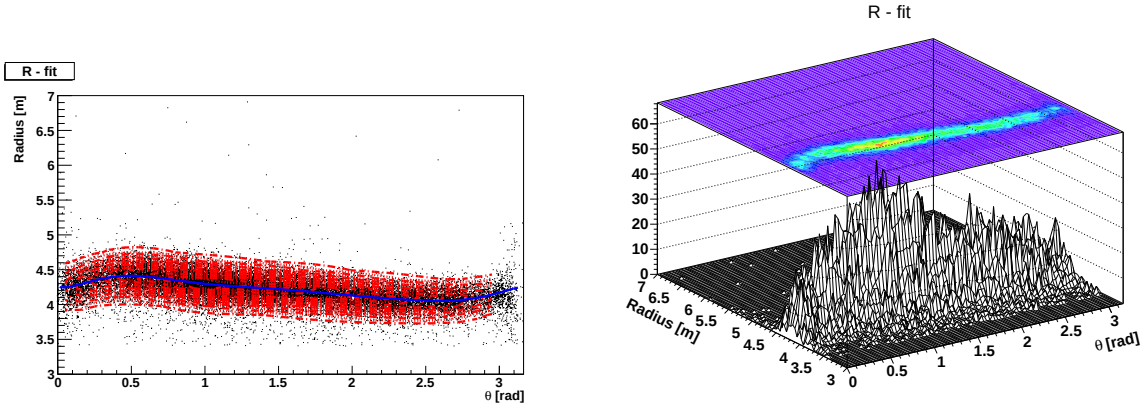

(a) 2D-View (b) 3D-View

Leak case with maximum of luminosity of leak

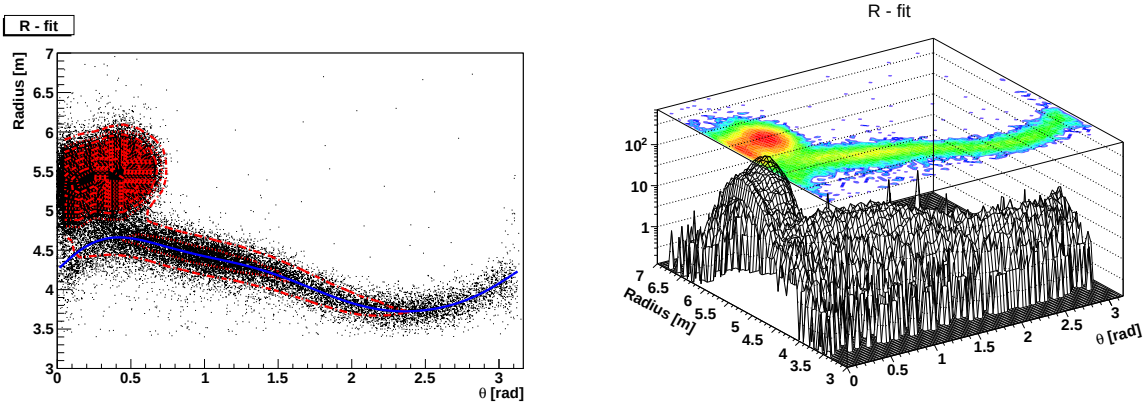

(c) 2D-View (d) 3D-View

Figure 2.22: Results of the fit for standard case (Figure **a**) and with the presence of leak spot. The red region present in figures a) and c) are the 2D function that describes the different distributions of data. The blue line is the Fourier-like function that describes the real profile of IV. Also in presence of the blob, due to leakage in the top side of the detector, the profile of the nylon vessel is well described by blue line.

2.5.5 Fiducial Volume Selection

In the previous paragraph we defined a method to locate the nylon vessel depending on the weekly dataset. To define a fiducial volume we have to perform a cut starting from the vessel profile, choosing a fixed distance from it.

We define this distance from IV as the radius of a circle tangent just in a one point to

IV profile. By moving the circle on this profile, we can use the coordinates of the center of small circle (r_0, ϕ) to determine the position of a new surface in polar coordinates that describes the new Fiducial Volume region.

The circle equation in polar coordinates is written as:

$$C(\theta, r_0, \phi) = \frac{1}{2}\left(\sqrt{2}\sqrt{2R^2 - r_0^2\left(1 - \cos(2(\theta - \phi))\right)} + 2r_0 cos(\theta - \phi)\right) \tag{2.24}$$

where R is the radius of circle, namely the distance from vessel, r_0 is the coordinate of the center of the circle and ϕ is the angle where we want to find the solution of the following system by varying the angle θ. In order to find the tangent circle to the vessel profile, we have to impose the following two condition for a given angle ϕ:

$$\begin{cases} C(\phi) = \mu(\phi), \\ \\ \dfrac{dC(\phi)}{d\phi} = \dfrac{\mu(\phi)}{d\phi}, \end{cases} \tag{2.25}$$

where $\mu(\theta)$ is the inner vessel profile described by Fourier-like expansion.

The issues arise when we have to evaluate the solutions of the system (θ, r_0) at the endpoints of vessel, in which $\theta = 0$ or $\theta = \pi$. Beyond these two points our function is not defined and could take casual value (Red Line in Fig.2.23) for $\theta < 0$ and $\theta > \pi$. For this reason we cannot find any solution. To avoid this problem, we extrapolated the straight lines tangent to the vessel function in $\theta = 0$ and in $\theta = \pi$ (Magenta Line in Fig.2.23). Therefore we can use the "*Rolling Circle Method*" in order to determine the points for the new surface of Fiducial Volume (asterisk and Green Line in Fig.2.23).

In this case we divide θ angle in 6 degree steps, therefore for each step we take the central value and we find the zeros of the system between the circle and the vessel. At the end we interpolate these point, obtaining the fiducial volume. In addition, if necessary, we can perform also a Z_{cut} by switching on this option in the code. In This way we can reproduce the standard fiducial Volume ($Z_{cut} = \pm 1.67$ m) and also new kind of cuts to exclude the end-cups of the inner vessel, in order to maximize the volumes. For these reasons we summed to the $R_{FV}(\theta)$ function also another function that describes an horizontal cut at Z_{cut}-quota, but is possible to select also different shapes instead of a straight line as show in Fig.2.24 To define the final shape function

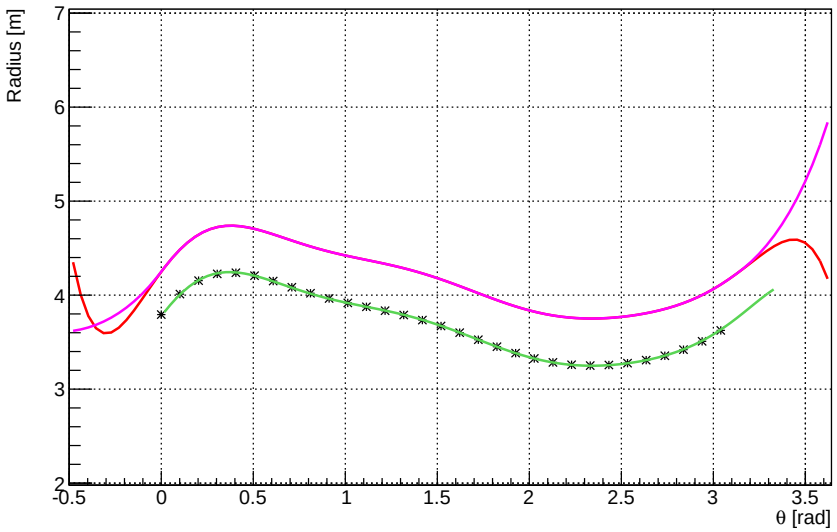

Figure 2.23: Final result of three steps method to determine new fiducial volume, fixing the distance from the inner vessel surface. In the example the distance is 0.25 m

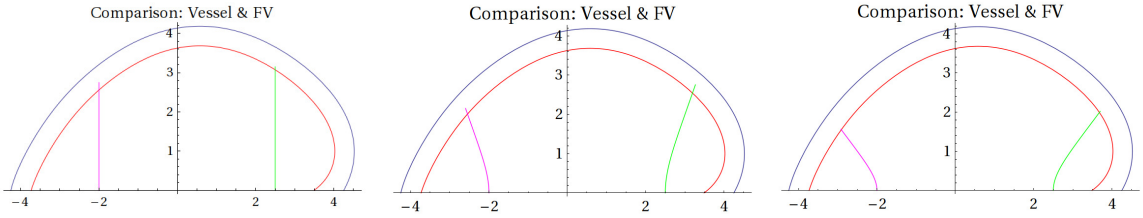

Linear: $Z_{cut}(\theta) = \pm\frac{d}{\cos\theta}$

Square: $Z_{cut}(\theta) = \frac{d}{\cos^2\theta}$

Quartic: $Z_{cut}(\theta) = \frac{d}{\cos^4\theta}$

Figure 2.24: Different shape Z_{cut} functions. The linear one correspond to the horizontal cut on Z axis where d is the fixed quota for the cut ($d_{std} = \pm 1.67$). For the Seasonal fiducial Volume has been necessary maximize the Volume to cut away only the end cup region considerably dirty with background events.

we solve before the system between the $R_{FV}(\theta)$ and $Z_{cut}(\theta)$ to obtain the intersection points $\hat{\theta}_i$, therefore we defined the new fiducial volume function as:

$$\hat{R}_{FV}(\theta) = \begin{cases} Z_{cut}(\theta) & \theta > \hat{\theta}_1 \\ R_{FV}(\theta) & \hat{\theta}_1 \leq \theta \leq \hat{\theta}_2 \\ Z_{cut}(\theta) & \theta > \hat{\theta}_2 \end{cases} \tag{2.26}$$

Now we can identify the fiducial volume profile with this new function in polar coordinates and then we can calculate the fiducial volume as the integral:

$$V_F = 2\pi \int_0^{\pi} d\theta \hat{R}^3_{FV}(\theta) \sin(\theta) \tag{2.27}$$

and the error can be evaluated as:

$$\sigma_{FV} = 2\pi \int_0^{\pi} d\theta \hat{R}^3_{FV}(\theta) \sin(\theta) \frac{\sigma_R(\theta)}{\sqrt{N_{bins} - 1}} \tag{2.28}$$

where $\sigma_R\theta$ it's the resolution of Gaussian function 2.18.

2.6 Data Selection

The solar neutrino events cannot be distinguished by background events. However a series of cuts applied on an event-by-event basis has been developed with the aim to remove the tagged background and non physical events. This series of cuts have been used to select the event in order to build the final spectrum for ^{7}Be, pep and CNO analysis. For the seasonal analysis, as already explained, the fiducial volume that has been modified with respect to the standard analysis.
Basically these cuts operate on four fundamental physical quantities measured from the Digital Acquisition System (DAQ): time, energy, position of the event and Gatti's parameter (Pulse shape). We present quickly the main variables used to perform the data selection.

2.6.1 Variable Definition

Gatti's Parameter

This parameter is defined starting from two reference pulse shapes obtained from the PMTs output signal [79, 80, 81]. By means of the study of ^{214}Bi–^{210}Po fast decay and from the ^{11}C pure events, we have been able to select three pure sample for β^- (^{214}Bi), β^+ (^{11}C) and α (^{210}Po) events. Therefore, as shown in Fig.2.25, we have build these two reference shapes that we used to evaluate the Gatti's parameter as follow: we call

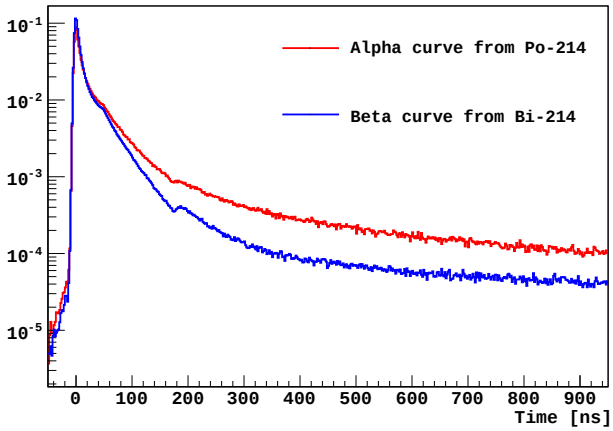

Figure 2.25: Final result of three steps method to determine new fiducial volume, fixing the distance from the inner vessel surface. In the example the distance is 0.25 m

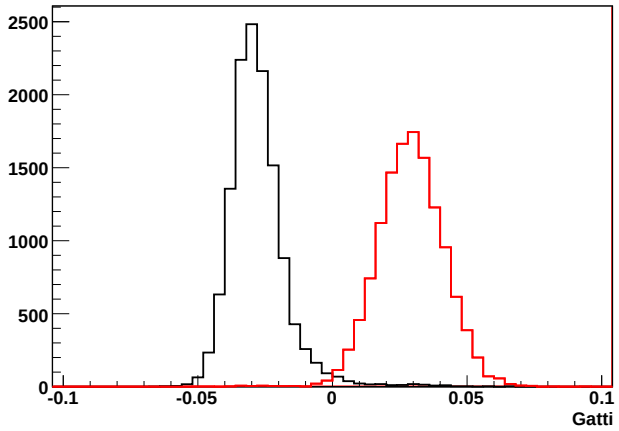

Figure 2.26: Final result of three steps method to determine new fiducial volume, fixing the distance from the inner vessel surface. In the example the distance is 0.25 m

$P_1(t)$ and $P_2(t)$ the normalized reference shapes. We rebin these reference shape in order to compare directly with the data:

$$r_{1,2}(t) = \int_{t_0+n\Delta t}^{t_0+(n+1)\Delta t} P_{1,2}(t)\mathrm{d}t \tag{2.29}$$

where n in the number of the bins and Δt the binsize. We define then the Gatti parameter as:

$$G = \sum_n e(t_n)w(t_n) \tag{2.30}$$

where $e(t_n)$ is the distributions of the time-binned distribution for the generic events measure in the experiment and $w(t_n)$ is a weight defined as:

$$w(t_n) = \frac{r_1(t_n) - r_2(t_n)}{r_1(t_n) + r_2(t_n)} \tag{2.31}$$

Also G has a proper distribution in which the mean value is:

$$\hat{G} = \sum_n r(t_n)w(t_n) \tag{2.32}$$

and a corresponding variance:

$$\sigma_G = \frac{1}{N}\sum_n r(t_n)w^2(t_n) - \hat{G} \tag{2.33}$$

that might be energy dependent. In Fig.2.26 we show the two distribution for α (Red line) and β (Black line) events. The beta events have a negative Gatti's parameter and the α events a positive Gatti's parameter. These properties have been used to cut away the ^{210}Po alpha events by mean of a double Gaussian fit and statistical subtraction.

Spherical Harmonics and anisotropy parameter

These variables are necessary to perform a correction of noisy events. We assume that each event is generated in initial point and the photoelectrons propagate in isotropic way. The angular distribution of $\cos(\theta)$ and ϕ by means of position reconstructions are developed in *Spherical Harmonics*:

$$Y_l^m(\theta,\phi) = \frac{2\sqrt{\pi}}{N_h} e^{im\phi} P_l^m(\cos\theta) \tag{2.34}$$

with $m = -1, 0, 1$ and P_l^m the Legendre polynomials and N_h is the total number of detected hits. Therefore we calculate three complex coefficients S_m:

$$S_m = \sum_{i=1}^{N_h} Y_l^m(\theta_i, \phi_i) \tag{2.35}$$

where the index runs on the hits in the cluster while θ_i and ϕ_i are the spherical coordinates of the hit PMT in a reference frame centered in the reconstructed vertex. We define the SHp variable as:

$$SHp = |S_{-1}| + |S_0| + |S_1| \tag{2.36}$$

For the anisotropy parameter β_l we take a pair of events i and j and evaluate the angle θ_{ij} between the two PMTs in which the event i^{th} and j^{th} are detected with respect to the reconstructed position of the event. The anisotropy parameter is defined as:

$$\beta_l = \frac{2}{N(N+1)} \sum_{i=0}^{N} \sum_{j=i+1}^{N} P_l(\cos\theta_{ij}) \tag{2.37}$$

where $P_l(\cos\theta_{ij})$ is the Legendre polynomial and N is the number of photoelectron.

2.6.2 Standard cuts for Events Selection

Muons Identification

As already explained the detector is provided of a outer detector (OD) and internal detector (ID). The outer detector is necessary to detect the cosmic rays in order to identify the muon events and to remove the so called daughter-muon events. A detailed discussion is present in [13]. A muon that passes in Water Tank (WT) shield emits a Čerenkov light that produce a cluster of hits in the OD PMTs. This event does trigger the OD by creating a Muon Trigger Flag (MTF) in the Muon Cluster Rack (MCR). Then we might to have three cases: first, the muon passes also in the IV producing a large amount of light with a specific pulse-shape (Inner Detector Flag, IDF), therefore this is excluded from DAQ because three of these flags have been activated; second the muon passes only through the buffer region: in this case all three flags are not active, but the muon saturate the electronics of detector. For this reason all PMTs are vetoed for 300 ms, in order to exclude all the cosmogenics decay events. The third case is when the muon passes only in the OD. In this last case the neutrons produced in the WT could penetrate inside the Inner vessel therefore a time-veto of 2 ms are sufficient to absorb the external neutrons. The total live time reduction after these cuts is equal to 1.6%.

Multiple Cluster Events

All accepted events have to deposit just one time the energy during the DAQ gate of 16 μs. If during this period the cluster algorithm does not identify any or multiple energy depositions on a single PMTs, then the event is rejected. The pile-up occurs when in the gate two or more event are too close in time to be distinguished. Therefore a condition is that each accepted event must have a single peak in the DAQ gate.

Removal of Coincidence Events

All events with mutual distance smaller than 1.5 m, in 2 ms of time window, are rejected. This cut remove all random events and the ^{214}Bi–^{214}Po events produce in the

Radon chain decay.

Check of N_{pe} quality

The quality of charge variable defined in Eq.**??** for each event is checked by means of two independent parameters: R_{pe} and R_q.
R_{pe} is defined as the ratio $R_{pe} = N_{pe}/N_{pe}^{exp}$ of number of photoelectrons measured N_{pe} and the number of photoelectrons expected N_{pe}^{exp} for a given number of PMTs hit N_p:

$$N_{pe}^{exp} = \frac{-N_{tot} \cdot \ln\left(1 - \frac{N_p}{N_{tot}}\right)}{\left[1 + g_C \cdot \ln\left(1 - \frac{N_p}{N_{tot}}\right)\right]} \tag{2.38}$$

in which N_{tot} is the total number of PMTs and g_C depend from the fiducial volume adopted, usually the value is 0.11. R_q instead is used to exclude the events that have an abnormal number of hits with a invalid charge and is defined as:

$$R_q = \frac{N_{pe}}{N_{pe-avg}} \tag{2.39}$$

where N_{pe-avg} is are the number of photoelectrons with a valid time but invalid charge, therefore the charge is taken equal to the average of other valid hits in the 15 ns time window around the hit. For a valid scintillation event this number is equal to one. The accepted ranges for these two values are:

- $0.6 < R_{pe} < 1.6$;
- $R_q > 0.5$

They are used also to suppress the noisy events.

Isotropy of light emission and Sphericity Control

In order to check the isotropic emission of the light in a scintillation event, we can use the anisotropy parameter and the Spherical Harmonics to check the features as follow:

- $\beta_l < 0.027 + \exp(1.3060.017N_{pe}) + \exp(3.1990.002N_{pe})$;
- $SHp < 0.119 + \exp(12.3570.305N_p) + \exp(0.6120.011N_p)$

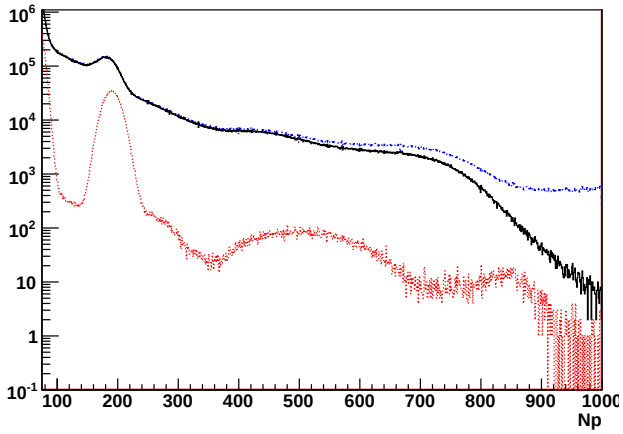

Figure 2.27: The effects of event selection are well visible in these spectra. The initial spectrum is the blue one. The first important reduction is due to muon event cut that dominate mainly at high energy (Black line). The other important reduction is due to fiducial volume cut that reduce the number of event until to obtain the red spectrum.

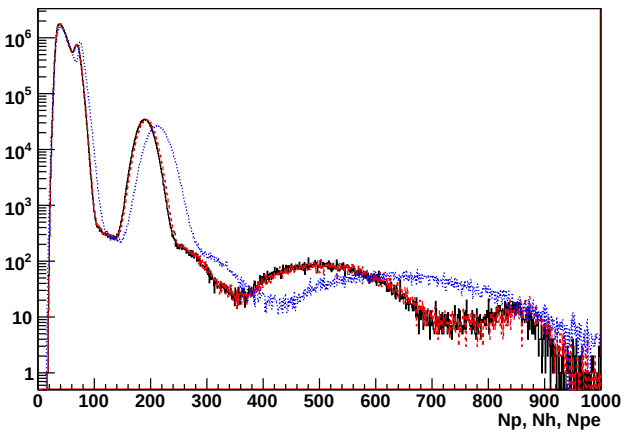

Figure 2.28: In this figure we observe the survival event to the cuts described from different energy variables: N_p (black), N_h (red) and N_{pe} (blue).

Additional noise removal

The position of a cluster which caused the trigger generation has a well defined position within the DAQ gate. The rms of the distribution of the cluster start time is ∼55 ns and features some tails. An event is accepted only if its cluster starts within a conservative 1.7 μs wide time window which has a fixed position in the DAQ gate.

Final Results

In Fig.2.27 are showed the spectra at different step of the standard cuts. The Final spectrum used in ^{7}Be analysis [91], applying the standard fiducial volume, is the red one. In the Seasonal analysis has been used the same cuts with exception of the fiducial volume larger than the standard one.

In Fig.2.28 we show the same spectrum but withe the different energy variables. In the last spectrum are well visible the Polonium peak around 200 npe in $N_{p,h}$ variable and 210 npe in N_{pe}. The Beryllium shoulder is in evidence between 240–320 npe in $N_{p,h}$

variable and between 300–400 npe with N_{pe} variable. The other important structures in the spectrum are the ^{11}C spectrum between 400-700 npe in $N_{p,h}$ and the high energy peak of the Thallium ^{208}Tl at 860 npe in $N_{p,h}$ variables. Increasing the radius of the fiducial volume we observe that the main contribution due to external background is present at these high energies.

Chapter 3

Empirical Mode Decomposition

3.1 Introduction

The Weierstrass theorem establishes that it is possible, in general, to approximate of continue functions in a close interval $[a, b]$, with a polynomial function $P_n(x)$. This polynomial is a orthogonal and complete base in the functional space for the function $f(x)$, then:

$$\lim_{M\to\infty} P_M(x) = f(x) \tag{3.1}$$

A particular polynomial set is the Fourier series expansion, in which the base is composed by orthonormal trigonometric functions $\sin^n(x)$ and $\cos^n(x)$ that are a superposition of the versor $e^{\pm inx}$:

$$f(x) = \lim_{M\to\infty} f_M(x) = \lim_{M\to\infty} \sum_{n=-M}^{M} \frac{c_n^{(M)}}{\sqrt{2\pi}} e^{inx} \tag{3.2}$$

the superscript M means that the Fourier coefficients $c_n^{(M)}$ are depending on the number of terms used in the expansion.

The convergence of Fourier series to the function $f(x)$, continue in the closed interval $[-\pi, \pi]$, is uniform only if $f(x)$ is continue and its derivative is a piecewise continue function with $f(-\pi) = f(\pi)$. In addition if $x \in [-\pi, \pi]$ and $f(x)$ is periodic, $f(x) = f(x + 2\pi)$, the convergence is uniform everywhere.

The Fourier transform could be generalized for each kind of interval $x \in [a, b]$, with $a, b \to \infty$. This is used to decompose in spectral components any kind of continue

functions. All these components are called harmonics and are preexisting for the whole sampling time, even before that their effects may be visible in the signal. In addition their frequencies are a physical system constants. What does it happen if the function is not periodic and non linear? To approximate the discontinuous points, the expansion in Fourier series generate a very high number of these harmonics, but losing the frequency resolution and overestimating the total energy associated with the spectrum. This is a really big problem related to the Fourier analysis applied on non linear and non stationary functions like noisy real dataset, where the signal-to-noise ratio is extremely low ($SNR < 0.5$).

The seasonal modulation of neutrino fluxes is an excellent periodical signal, but it is hidden in a higher statistical fluctuation of data, because of the very low statistics in the daily count rates. From Monte Carlo simulations, we found that the signal to noise ratio expected is about $SNR \sim 0.2$, therefore extremely weakly compared to the statistical noise. To perform the seasonal modulation analysis, we have to apply a numerical method able to filter out all high frequencies due to the statistical fluctuation, leaving only the expected seasonal frequency given by:

$$\nu_{Seas} = \frac{1}{365.24\,[day]} = 2.739 \times 10^{-3}\ [day^{-1}].$$

In order to extract this signal from Borexino dataset, we will apply a new empirical method introduced by Huang *et al.* 1998 [98], called *"Empirical Mode Decomposition"* (EMD), to decompose the non linear dataset in a set of oscillating mode functions called *"Intrinsic Mode Functions"* or IMF. In order to perform the extraction of these IMF we applied the numerical algorithm called *"sifting"* based on cubic-spline interpolation. It is worth to point out that there is not an analytical formulation for the IMF, as in the Fourier expansion. A key role is played by the stopping criteria of the sifting algorithm to extract each IMF. The theory poses two general criteria that each IMF must satisfy, but in the numerical algorithm there are several ways to obtain it. We took into account two criteria proposed by Rilling [103] and another one proposed by Wu and Huang [101].

Finally we used the Wu and Huang criterion for two main reasons: a poor literature found with the Rilling criteria and a slightly stronger and complete theoretical discus-

sion of Wu and Huang criterion.
In the next of this chapter we will show that IMFs are able to describe much better the real spectrum of non linear functions with higher frequency resolution. In addition we will demonstrate that these IMFs are complete and also a *"quasi-orthogonal"* base of functions for signals.

3.2 Sifting procedure and IMF definition

3.2.1 The *"sifting"* algorithm

We can think of the Empirical Mode Decomposition (EMD) as an extension and generalization of Fourier Transform (FT) for non linear and non stationary functions. Unlike the harmonics obtained with FT, in which we force to expand any continue function in terms of sine or cosine with a constant frequency for each component, the Empirical Mode Decomposition decomposes a given signal in a superposition of adaptive functions with a narrow frequency band: the Intrinsic Mode Functions (IMF).
The IMFs carries the physical information and represent, ideally, one frequency (nearly monochromatic). The IMF can be defined as the residual function obtained from reiteration of the sifting procedure, by mean of an algorithm defined for the first time by Huang [101], until to satisfy the IMF conditions. This algorithm can be summarized as follow:

1. For any data set $x(t)$ we identify all local extrema (maximal and minimal).

2. We interpolate all local maxima (minima) with a cubic spline obtaining two envelopes for the local maxima (minima) $u(t)$ ($l(t)$) Fig.3.1.

3. Therefore we take mean function between the two envelopes

$$m(t) = [u(t) + l(t)]/2. \tag{3.3}$$

4. Then we take the difference between the initial function $x(t)$ and the function $m(t)$:

$$h(t) = x(t) - m(t). \tag{3.4}$$

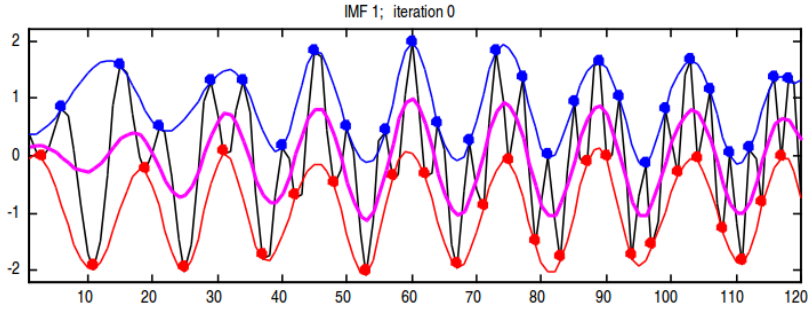

Figure 3.1: Sifting Procedure. The blue line is the cubic spline to interpolate the local maxima (blue points) and the red line the local minima. The magenta line represents the mean value of two envelopes.

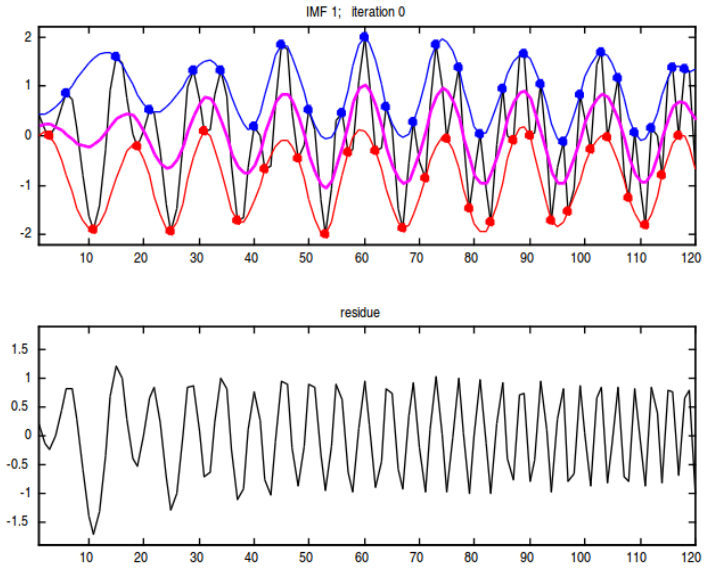

Figure 3.2: Subtraction of proto-IMF from original signal. In this case the residue do not have mean value equal to zero over all, then we have repeat the sifting procedure again.

We call $h(t)$ proto-IMF, as in Fig.3.2.

5. We have to check if the proto-IMF satisfy two conditions:

   – The number of local extrema and the number of zero-crossing points must be equal or differ at most by 1.

   – At any time the mean value between two envelopes $u(t)$ and $l(t)$ must be zero.

If the proto-IMF satisfies these two conditions and the stopping criteria as in Fig.3.3, then it is a IMF;

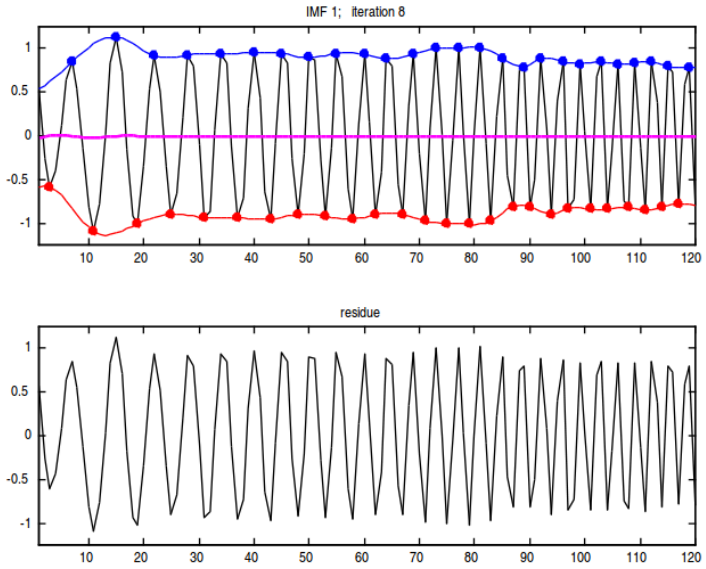

Figure 3.3: Subtraction of kth-proto-IMF from the previous one (i−1)th. In this case the residue have the mean value equal to zero over all its length, then it satisfy one of IMF criteria.

6. If the proto-IMF does not satisfy the previous conditions we iterate the point 1-5 on the function $h(t)$ as many time as needed until it satisfies the conditions and stopping criteria.

7. At the end, if the proto-IMF satisfies the condition 5, we promote it as IMF and call it $c(t)$.

8. Repeat the points 1–7 on the residue

$$r(t) = x(t) - c(t) \tag{3.5}$$

as if it is a new dataset.

9. The operation ends when the last residue contain no more that one extreme.

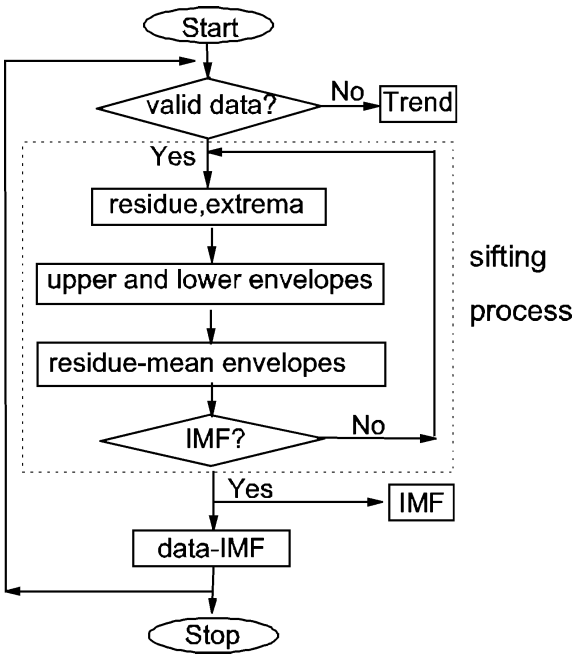

Figure 3.4: Sifting procedure scheme to extract the intrinsic mode function.

Mathematically, to obtain the first IMF, we can write the procedure as follow:

$$\begin{aligned}
&h_{1,1}(t) = x(t) - m_{1,1}(t) \\
&h_{1,2}(t) = h_{1,1}(t) - m_{1,2}(t) = x(t) - (m_{1,1} + m_{1,2}) \\
&\cdots \\
&\cdots \\
&h_{1,k}(t) = h_{1,k-1}(t) - m_{1,k}(t) = x(t) - (m_{1,1} + m_{1,2} + \cdots + m_{1,k}); \\
&\Rightarrow c_1(t) = x(t) - \textstyle\sum_{l=1}^{k} m_{1,l}
\end{aligned} \tag{3.6}$$

where $h_{1,k}$ is the k-th proto-IMF that satisfy the stopping criteria. Subsequently, we have:

$$\begin{aligned}
&x(t) - c_1(t) = r_1(t); \\
&r_1(t) - c_2(t) = r_2(t); \\
&\cdots \\
&\cdots \\
&r_{N-1}(t) - c_N(t) = r_N(t);
\end{aligned} \tag{3.7}$$

$$\Rightarrow x(t) - \sum_{j=1}^{N} c_j = r_N(t). \tag{3.8}$$

where N can be evaluated from the dataset bin number, as shown in the next section. It can be shown that, the base formed from all IMFs is a complete base for the initial function:

$$x(t) = \sum_{j=1}^{N} c_j + r_N(t) \tag{3.9}$$

In this procedure the sum of all IMFs can reproduce exactly the initial signal (completeness) and it is quite easy to implement by means of the cubic spline. But there is a question still open: what are the stopping criteria for the procedure to be closed?

3.2.2 The IMF stopping criteria and their properties

The first criterion for the sifting algorithm stoppage was proposed by Wu & Huang in 1998 [98], called Cauchy criterion, in which the sifting process stops when the Standard Deviation (SD):

$$SD = \sum_{t=0}^{T} \frac{[h_{k-1}(t) - h_k(t)]^2}{h_{k-1}^2(t)} \tag{3.10}$$

is smaller than a fixed value, usually between 0.2 and 0.3. In Eq.3.10 $h_k(t)$ are the proto-IMF at k-th step of j-th mode. In literature there are several other stopping criteria, but unfortunately there are not yet strong theoretical prescription to impose a criterion with respect to another one. Two independent studies of Flandrin *et al.* 2004 [104] and Wu & Huang 2004 [99] demonstrate that the EMD have the property of a bank of dyadic [1] filter, in particular way Wu and Huang 2004 showed that performing the sifting procedure about 10 times to extract each IMF, the algorithm behaves as a dyadic filter.

A number of iterations too high or too low can produce effect of over-decomposition or under-decomposition, in the sense that the last IMF can still have some local maximum or local minimum and not a monotonic shape.

Starting from dyadic filter properties of the algorithm, we have that the number of cycles in the latest IMF are about half of previous one extracted and so on, until the

[1] The term "dyad" simply means "two". Thus, successive bands in a dyadic filter bank are obtained using a frequency-scale factor two.

last IMF that is monotonic (*trend*). Therefore, using the Nyquist-Shannon sampling theorem [109, 110], the sampling frequency must be at most double than the higher frequency present into the signal. We can assume the inverse of temporal unit of single bin as the sampling frequency of the dataset, therefore the maximum frequency that we can observe in the data spectrum is given by Nyquist frequency:

$$\nu_{Nyq} = \frac{n_{bins}}{2\Delta t}, \tag{3.11}$$

where n_{bins} is the number of bins present in our sample and Δt is the time bin-size. From the dyadic properties of algorithm, again, we can also deduce the maximum number of IMF that can be extracted:

$$N_{IMF}^{Max} = -\lfloor \log_2 \nu_{Nyq} \rfloor \tag{3.12}$$

where the *"floor"* brackets indicate the *"lower"* integer part of logarithm: $\lfloor x \rfloor = x - \{x\}$, where $\{x\}$ is the fractional part of the real number x. In addition each IMF has a narrow spectral band that is peaked around the frequency of the main component of the signal contained in the dataset. In general we find that if in the data is present only white noise, the bounds of IMF spectrum is, at leading order, defined by the empirical relation:

$$2^{-(N_{IMF}+1)} < \nu_{IMF} < 2^{-N_{IMF}}. \tag{3.13}$$

Therefore, given an expected frequency ν, we will find this component in the IMF number N_{IMF}:

$$N_{IMF} = -\lfloor \log_2 \nu \rfloor. \tag{3.14}$$

If all IMF found follow these rules, then the dyadic filter properties are preserved.

3.2.3 Huang Method and EEMD

We found a Matlab code in RCADA official internet site[2] where are also present most of the reference papers with some application in different fields. We implemented these

[2]RCADA – Research Center for Adaptive data Analysis

(*http://rcada.ncu.edu.tw/research1_clip_program.htm*)

basic codes in a more complex program to perform the seasonal modulation analysis of solar neutrinos, also adding new functions to evaluate the initial phase and the instantaneous frequency, as we will show in the next section.
The Huang's code used can works with two kind of algorithms:

- The standard EMD algorithm, where the user can choose the number of iterations of sifting procedure to extract each IMF (we used 20 iterations for the analysis, but the default was 10).

- The so called *"Ensemble Empirical Mode Decomposition"* (EEMD) in which the standard procedure is iterate many times adding a white noise to the signal (Dithering). The standard method does not consider this procedure.

The most important step in the Empirical Mode Decomposition is the performance of the sifting algorithm, that decomposes the initial dataset in its Intrinsic Mode Functions. The standard EMD, in which this algorithm is applied just once on dataset, showed several problems related to its strong dependence from the initial conditions. In addition the mixing mode effects are observed, in which a physical signal, with a given frequency, is shared on different IMFs.
Therefore, changing the initial condition of dataset (i.e. performing another data taking or adding the white noise with a finite amplitude) the resulting IMFs change their shapes. Doing several tests $x_i(t)$, adding each time to the initial signal $x(t)$ a new set of white noise $\omega_i(t)$:

$$x_i(t) = x(t) + \omega_i(t) \tag{3.15}$$

and taking the average of IMFs for j-th mode extracted from all $x_i(t)$ (or *"ensemble"* of IMFs), the mixing mode effect disappears as well as the dependence of IMF shape from initial conditions. This method is the new improvement of EMD, called Ensemble Empirical Mode Decomposition (EEMD).
Assuming the presence of a given signal into the dataset, the statistical fluctuation can introduce some distortions. This effect is important especially if the signal to noise ratio (SNR) is particularly low.
Adding the white noise to the initial dataset, also if the SNR slightly decreases, it can

delete partially the distortions due to the statistical noise. Performing this sum several times and taking the IMF average for a given oscillating mode, the white noise eliminates the distortions of statistical noise leaving only the persistent contribution of the physical signal hidden in the dataset, or simply distorted by the statistical fluctuations. The amplitude of the white noise is a free parameter that has to be evaluated case by case. It is given by the sigma of a Gaussian distribution with mean value centred on zero, used to generate the random white noise. A too small value of its standard deviation σ_{std}, as compared with the Poissonian bin error, does not change very much the initial conditions and is not enough to delete the statistical noise.
Conversely, amplitude comparable with the statistical error, or larger, can damage seriously the information contained in the dataset. A good value used in the literature, but found also empirically by means of several simulation in the next chapter, is around $10\%\langle\sigma_{bin}\rangle$, where $\langle\sigma_{bin}\rangle$ is the average error in the dataset. We have the best performance of sifting algorithm when the dataset is continuous, but some gaps might be present. They can be filled with random events, with the same features of the data. The gap dimension must be much smaller than the length of the signal period, to preserve the information.

3.3 Instantaneous Frequency

This kind of analysis introduces a new concept of *"Instantaneous Frequency"* (IF). In the classical wave theory and Fourier analysis, we consider each signal as an superposition of sine and cosine components with well specified frequency ω, defined as the inverse of period T:

$$\omega = \frac{2\pi}{T} \tag{3.16}$$

Mathematically we define this quantity as a temporal derivative of a phase function or, in case of wavelength, as a spatial derivative of phase function:

$$\omega = -\frac{\partial\theta}{\partial t} \qquad k = \frac{\partial\theta}{\partial x} \tag{3.17}$$

Therefore we obtain the following law of wave conservation:

$$\frac{\partial \theta}{\partial x} + \frac{\partial k}{\partial t} = 0. \tag{3.18}$$

This relation is one of fundamental laws that governs all wave motions and it must be verified for all kinds of vibrational motions, beyond the trivial one of a sinusoid with a constant frequency. This can justify also mathematically the new concept of Instantaneous Frequency (IF) introduced with EMD. The Fourier analysis is able to decompose a given signal in several sinusoidal components, called harmonics. But it fails when is applied to non-stationary signal or non linear functions, producing a very high number of harmonics to approximate the original signal. Only a small number of these harmonics contains a real physical meaning, the other ones are only an mathematical artefact without any physical meaning.

To solve this problem, several numerical methods were introduced in order to decompose a non stationary signal. The most used technique is the *windowing*, in which the whole dataset is divided in smaller time windows, also with different size, and then the Fourier transform is applied, as in the wavelet, Lomb-Scargle and other numerical procedures.

These new procedures move the problem to smaller scale, but does not solve the key problem, that is: the Fourier series, by definition, converges in uniform way to a function $f(t)$, in a closed interval $[\pi, -\pi]$, if $f(t)$ is continuous and its derivative is a piecewise continuous function in this interval and have both $f(\pi) = f(-\pi)$ and $f(t) = f(t + T/2\pi)$. Then it could be applied in a right way only to continue and periodic functions. The other applications are only a forcing of linear approximation to non linear systems.

The harmonic distortions showed by Fourier analysis, can be explained as the effect of a *"intrawave"* that modulate in time the signal frequency. The intrawave is a characteristic of non stationary or non linear system, because it describes the time evolution of frequency of a system also within a period of oscillation. To describe this new entity of wave system we need to use the instantaneous frequency.

In Fig.3.6 we show four different time-frequency spectra of the same signal: the speech *"Hello!"* shown in Fig.3.5. To obtain the four kind of spectra are used a filter pass-

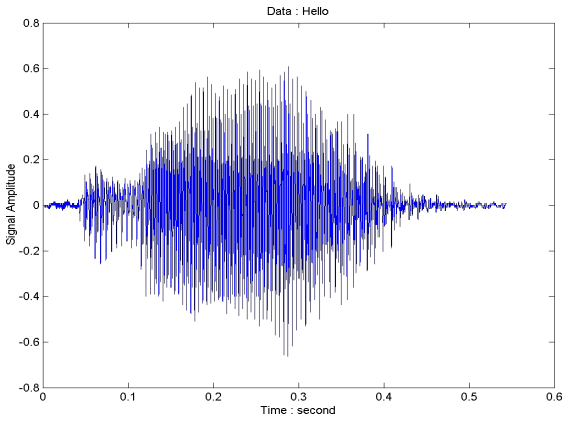

Figure 3.5: Speech signal for the sound *"Hello!"*.

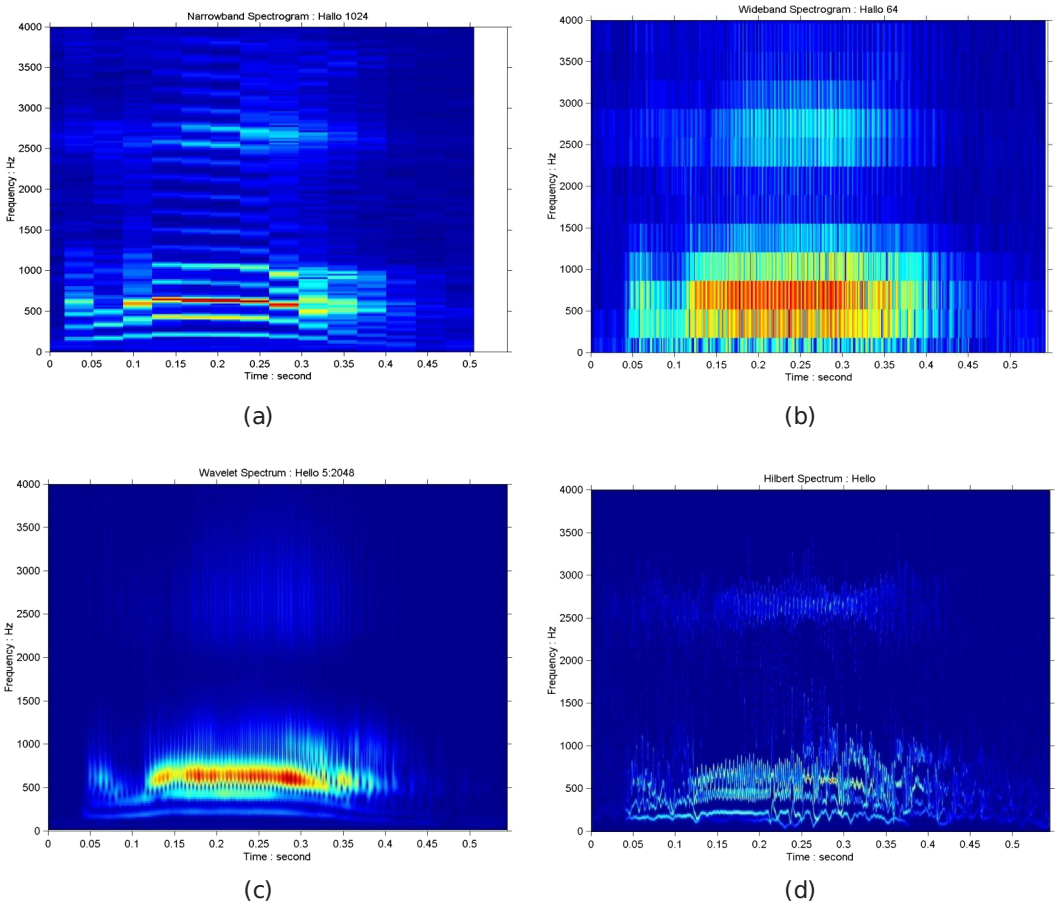

Figure 3.6: Comparison between time-frequency spectrograms obtained with different techniques from the speech in Fig.3.5: (a) Narrow band, (b) Wide band, (c) Morlet-wavelet, (d) Normalized Hilbert Transform (NHT).

band (a), wideband (b), Morlet-wavelet (c) and Normalized Hilbert transform (d). All four spectra present more or less the same pattern, therefore can localize the main frequencies in the same way, but what really changes is the capability to separate the different components. In particular by comparing the Morlet-wavelet (c) with NHT (d), we observe an increasing of details in the time frequency composition in the case of EMD compared to Wavelet technique. These spectra show the high capability of EMD to separate the real components present in a signal evaluating also their real associated energy. In the case of wavelet, we observe a very high color range for the main components. This means that the Fourier Transform overestimate the real energy (proportional to square of the amplitude) contained in each spectral component.

3.3.1 The Analytical Signal

In the ideal case, the instantaneous frequency (IF) of a mono-component signal should be evaluated as the time derivative of a phase function $\theta(x,t)$, that is the argument of an analytical signal where the imaginary part is given by a $\pi/2$ shift of its carrier function $\cos\varphi(t)$ by mean of the quadrature operator $\mathcal{Q}[x(t)]$. Thus any mono-component signal can be divided as:

$$x(t) = a(t)\cos\varphi(t), \tag{3.19}$$

where $a(t)$ is the amplitude modulation function and $\cos\varphi(t)$ its carrier function. Therefore applying the quadrature operator to the signal, we obtain:

$$\mathcal{Q}[x(t)] = a(t)\sin\varphi(t). \tag{3.20}$$

With these expression we can evaluate the IF as in the standard wave theory, by mean of Eq. 3.17, but it is not easy to do this for quasi-mono-component functions obtained with Empirical Mode Decomposition or wavelet decomposition. The first one is how to find a unique pair of functions $[a(t), \phi(t)]$ to represent the data, the second is how to find a method to calculate the quadrature of the signal directly.
In the traditional way this is done by means of the Analytical Signal (AS) through the Hilbert transform (HT) but actually this is only an approximation of quadrature.

To obtain the AS, first we have to write the Hilbert transform for our signal:

$$y(t) = \frac{1}{\pi}\mathcal{P}\int_{-\infty}^{\infty}\frac{x(t')}{t'-t}dt' \tag{3.21}$$

where $\mathcal{P}$ indicate the Cauchy principal value. Also in this case we have several ways to define the imaginary part $y(t)$, but the Hilbert transform provide the unique way to define a imaginary part such that $x(t)$ and $y(t)$ form a complex conjugate pair such that $z(t)$ is an analytical function:

$$z(t) = x(t) + i\,y(t) = a(t)e^{i\theta(t)} \tag{3.22}$$

where

$$a(t) = \left[x^2(t) + y^2(t)\right]^{1/2} \qquad \theta(t) = \arctan\left(\frac{y(t)}{x(t)}\right) \tag{3.23}$$

The equation Eq.3.23, together to the definition of Hilbert transform like a convolution of signal $x(t)$ and the function $1/t$ (Eq.3.21), emphasizes the local proprieties of $x(t)$. In general we define the Instantaneous Frequency as:

$$\omega(t) = \frac{1}{2\pi}\frac{\mathrm{d}\theta(t)}{\mathrm{d}t} \tag{3.24}$$

then, in principle from this definition, we need to have one frequency for a given time: this means a mono-chromatic function, but there is not a firmly definition of *"mono-component"* signal to judge whether a function is mono-component or not. For this reason it was used a definition of *"Narrow Band"* as limitation on data to define IF. Because the time derivative of the phase function $\mathrm{d}\varphi(t)/\mathrm{d}t$ has the physical meaning of IF, the AS has to show some features:

- The function has to be mono-component, with mean equal to zero locally;
- The wave has to be symmetric with respect to zero mean.

These conditions have to be verified from all IMFs obtained with EMD or by function extracted by means of wavelet, but these are only necessary conditions. A most general conditions that IMFs have to verify, are provided by two theorems: the Bedrosian theorem [105] and Nuttall theorem [106],

Theorem: *Bedrosian's Theorem (1963)*
Let $f(x)$ and $g(x)$ denote generally complex function in $\mathrm{L}^2(-\infty,\infty)$ of real variable x. If

1. the Fourier transform $F[u]$ of $f(x)$ vanishes for $|u| > a$ and the Fourier transform $G[u]$ of $g(x)$ vanishes for $|u| < a$, where a is an arbitrary and positive constant, or

2. $f(x)$ and $g(x)$ are analytic (i.e., their real and imaginary parts are a Hilbert pairs), then the Hilbert transform of the product of $f(x)$ and $g(x)$ is given by:

$$\mathcal{H}[f(x)\cdot g(x)] = f(x)\mathcal{H}[g(x)] \tag{3.25}$$

The Bedrosian theorem tells us that if the amplitude function $a(t)$ and the carrier function $\cos\phi(t)$ have no overlapping Fourier spectrum, we can separate the amplitude modulation factor from the carrier function and write:

$$\mathcal{H}[x(t)] = \mathcal{H}[a(t)\cos\phi(t)] = a(t)\mathcal{H}[\cos\phi(t)]. \tag{3.26}$$

Theorem: *Nuttall's Theorem (1966)*
Let $x(t) = a(t)\cos\phi(t)$, where $a(t)$ and $\phi(t)$ are arbitrary, not necessary narrow band functions, and $\mathcal{H}[x(t)]$ the Hilbert transform of $x(t)$ and $\mathcal{Q}[x(t)] = a(t)\sin\phi(t)$ is the quadrature of $x(t)$, then:

$$E = \int_{-\infty}^{\infty} [\mathcal{H}[x(t)] - \mathcal{Q}[x(t)]]^2 \,\mathrm{d}t = 2\int_{-\infty}^{\omega_0} F_q(\omega)\mathrm{d}\omega, \tag{3.27}$$

where

$$F_q(\omega) = F(\omega) + i\int_{-\infty}^{\infty} a(t)\sin\phi(t)e^{-i\omega t}\mathrm{d}t \tag{3.28}$$

where $F(\omega)$ is the Fourier spectrum of signal and $F_q(\omega)$ is the Fourier spectrum of quadrature of signal.

Therefore the necessary and sufficient condition so that the Hilbert transform coincides with the quadrature is that the error must be $E = 0$. This seems to be a great result, but there are several difficulties to apply it in practice.
The first one is that we do not know the spectrum of quadrature of signal $F_q(\omega)$ if the

quadrature is unknown. Then we cannot evaluate the error E. Another difficulty is due to the fact that the error is expressed as an integral, then it provides a global measurement of discrepancy and does not make possible to understand which part causes the error in a non stationary signal. The last issue is that, the Nuttall theorem, tells us only that $\mathcal{H}[x(t)]$ and $\mathcal{Q}[x(t)]$ are different, but does not offer an error index on the frequency, then it's only an approximation for the error index of IF.
The limitation of these two theorems are fundamental to define a IF with physical meaning, also because they have strong theoretical foundation.
To solve these serious problems, that can make useless the Hilbert Transform. Huang *et al.* 2010 [**?**] showed that performing the *"Normalization Scheme"* (NS) to decompose the AM from FM, both Bedrosian and Nuttall theorems are satisfied. This normalization has three important consequences:

1. This is the most important, the normalized carrier enables us directly to compute the quadrature;

2. The normalized carrier has an unitary amplitude, the satisfy automatically the Bedrosian theorem;

3. The normalized carrier enables us to provide a local energy based measure of error as that provided from Nuttall's theorem.

The NS is an empirical method designed to separate the AM from FM. First, we identify the local maximum extrema for the module of a given IMF. Then we interpolate it with the usual cubic spline and divide the IMF signal with this spline:

$$y_1(t) = \frac{x(t)}{e_1(t)} \tag{3.29}$$

in this way we can guarantee that the carrier function has a unitary amplitude. Really to obtain a unitary amplitude we have to iterate the procedure from 3 to 5 times:

$$\begin{aligned} y_2(t) &= \frac{y_1(t)}{e_2(t)} \\ &\vdots \\ y_n(t) &= \frac{y_{n-1}(t)}{e_n(t)} \end{aligned} \tag{3.30}$$

When $|y_n(t)|$ has all maxima less or equal to the unity, then the procedure is terminated and we can write:

$$y_n(t) = \cos\phi(t) = F(t) \tag{3.31}$$

where $F(t)$ is our carrier function. For the Amplitude Modulation function AM, we obtain that:

$$A(t) = \frac{x(t)}{F(t)} = \prod_{i=1}^{n} e_n(t). \tag{3.32}$$

Then we obtain that the original IMF is defined as:

$$x(t) = A(t) * F(t) = A(t)\cos\phi(t) \tag{3.33}$$

With this new definition we can calculate the Hilbert transform and define the AS as:

$$z(t) = x(t) + \mathrm{i}y(y) = A(t)e^{-\mathrm{i}\hat{\theta}(t)} \tag{3.34}$$

then the new phase function is:

$$\hat{\theta}(t) = \arctan\left(\frac{y(t)}{x(t)}\right) \tag{3.35}$$

3.3.2 Calculation of Frequency and Phase

Starting from the Euler's formula of Analytical Signal (AS), defined in Eq.(3.22), if we try to evaluate the Instantaneous Frequency (IF) simply as time derivative of phase function $\hat{\theta}(t)$, we obtain a unphysical result with negative values for the frequency.
Huang *et al.* 2009 [100] introduced a simply method to perform the empirical normalization of a given signal to evaluate the instantaneous frequency by means of two methods: the *Direct Quadrature* (DQ) or the *"Normalized Hilbert Transform"* (NHT). By means of empirical procedure of separating the Amplitude Modulation function (AM) from the Frequency Modulation function (FM) showed in the previous section, we define a carrier function $F(t)$ that satisfies the Bedrosian theorem, because symmetric with respect to the mean value with Fourier spectrum non overlapping with the amplitude modulation function and, in addition, its modulus is smaller than 1: $|F(t)| \leq 1$.

We can describe the carrier function as a cosine of the phase function because their values are contained within the unitary circle:

$$F(t) = \cos\phi(t). \tag{3.36}$$

Therefore, by applying the quadrature operator, that is a simply $\pi/2$ phase shift of the function, we can define the sine of phase function as:

$$\mathcal{DQ}[F(t)] = \sin\phi(t) = \sqrt{1 - F^2(t)}. \tag{3.37}$$

We can define the phase function $\phi(t)$ as:

$$\phi(t) = \arctan\left[\frac{\sin\phi(t)}{\cos\phi(t)}\right] = \arctan\left[\frac{\sqrt{1 - F^2(t)}}{F(t)}\right]. \tag{3.38}$$

Taking the time derivative of this phase function, we obtain an instantaneous frequency with a real physical meaning of frequency as in the classical wave theory. The Nuttal's theorem guarantees also that if we build the Analytical Signal, by means of Hilbert Transform of the Normalized carrier function $|F(t)| \leq 1$, and define the phase function as in Eq.3.23, where the AS amplitude now coincides with amplitude modulation function $A(t)$ in Eq.3.32, both Direct Quadrature and Hilbert Transform are identical and the Eq.3.27 is equal to zero. Therefore we can use alternatively both methods if before we perform the Normalization scheme. In this way we are sure that the Instantaneous frequency obtained has a physical meaning of a frequency.

Chapter 4

Seasonal Modulation Analysis

4.1 Introduction

In the following section we will describe the measurement of seasonal modulation of solar neutrino fluxes due to the Earth's revolution around the Sun. This kind of measurement is essential to demonstrate that the observed data from Borexino experiment are related to the solar neutrinos and, in particular, to the ^{7}Be neutrino.

At first glance it looks like a easy task but, unlike the muon seasonal variation [90], in which the sinusoidal modulation was well visible in the dataset, the weakness of the signal, the high intensity of statistical fluctuations and the background variation during the data taking, they made this measurement extremely challenging.

In addition the statistical noise plus the background variation does not make the signal periodic. This means that also applying the Fourier transform to extract the spectral components does not work properly because of non-stationarity data.

For these reasons, we decided to apply the EEMD method, instead of traditional methods based on Fourier transform, because the EEMD is an adaptive technique designed for non-stationary and non-linear signals and also because it is able to calculate with much more accuracy the instantaneous frequency.

The Earth's orbit is elliptical and the Sun occupies one of the foci. Its eccentricity is very small, about $e = 0.01671$, therefore we have calculated the time variation of

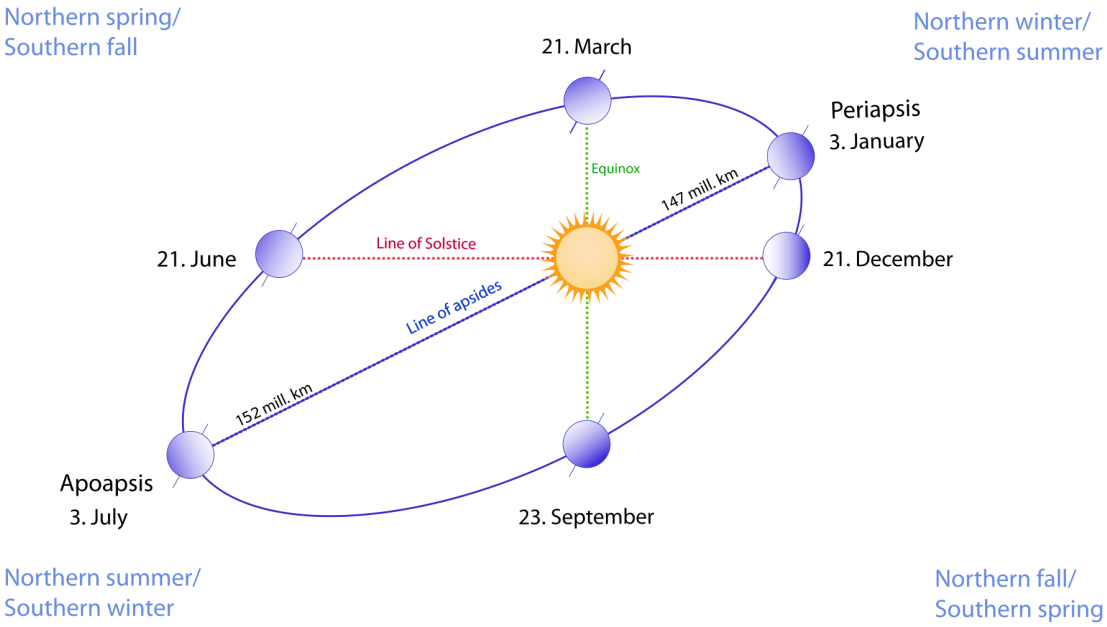

Figure 4.1: Earth's orbit with the dates of main positions. To define the phase we refer to 3rd January in which the flux is maximum $\varphi = 3$ [day]

distance from the Sun by using the Kepler's equations:

$$r(t) = \frac{a(1-e^2)}{1 + e \cdot \cos\theta(t)} \tag{4.1}$$

where $r(t)$ is the distance between the Earth and the Sun and

$$\theta(t) = 2\pi \cdot \frac{t-\varphi}{T} \qquad \text{with } \varphi = 3 \text{ Day}. \tag{4.2}$$

Actually the linear equation for the angle $\theta(t)$ is a good approximation with an error of the order of 0.03%. Therefore, it is negligible with respect to the precision of the experiment. The flux observed from Borexino, assuming the Earth dimensions negligible with respect to the *semi -major axis* $a = 1.496 \times 10^8\ km$, is:

$$\phi_{\nu}^{^7Be}(t) = \frac{\phi_{^7Be}^{Tot}}{4\pi r^2(t)} = \frac{\phi_{^7Be}^{Tot}}{4\pi a^2(1-e^2)^2}\left[1 + e \cdot \cos\left(\frac{2\pi}{T}(t-\varphi)\right)\right]^2 \tag{4.3}$$

where $\phi_{^7Be}^{Tot}$ is the isotropic flux for $\nu_{^7Be}$. When the neutrino flux comes out of the solar surface, it is already reduced because of the MSW effect. We can then convert directly the flux incoming in Borexino to Compton spectrum as it follows:

$$\Phi_e^{^7Be}(t) = \int_0^{T_e^{max}} \int_0^{E_\nu^{max}} \frac{\mathrm{d}\sigma(E'_\nu)}{\mathrm{d}T'_e}\bigg|_{ES} \frac{\mathrm{d}\phi_\nu^{^7Be}(t)}{\mathrm{d}E'_\nu} R(E'_\nu,\, T'_e)\, \mathrm{d}E'_\nu\, \mathrm{d}T'_e =$$

$$= \Phi_0^{^7Be} \cdot \left[1 + e \cdot \cos\left(\frac{2\pi}{T}(t-\varphi)\right)\right]^2 \tag{4.4}$$

where $\Phi_0^{^7Be} = 46.0 \pm 1.5\ cpd/100ton$ is the mean value obtained from ^{7}Be-analysis [91], T_e^{max} is the maximum electron recoil energy, from kinematic of elastic scattering:

$$T_e^{max} = \frac{2E_\nu}{mc^2 + 2E_\nu} \cdot E_\nu \tag{4.5}$$

and $R(E_\nu,\ T_e)$ is the detector resolution.

In order to exclude the background components at low and high energies, we selected a energy windows where to extract the signal. For this reason we are interested only in counting the rate of spectral components in this energy window.

4.2 Stability and Selection of Data

4.2.1 Data and Background Stability

The time stability of Borexino detector and its backgrounds are two crucial issues to perform the seasonal analysis of $\nu_{^7Be}$ solar neutrino flux. As showed in Fig.4.4, along with the Compton spectrum for electron-neutrino elastic scattering, in the energy range considered

$$105\ npe < T_e < 380\ npe,$$

there are several background components related to Radon chain. The daughter components of Radon can be divided in three kinds of events:

- **Fast coincidences:** Events like $^{214}Bi - ^{214}Po$. They are well identified and removed by mean of a filter program in a first selection of data (negligible);
- α **events:** The main contribution is provided by monochromatic component of the ^{210}Po, but there are also other small contributions provided by ^{218}Po, ^{212}Po and ^{222}Rn. These contribution are completely removed by means of α/β-cut.
- β**-events:** these kind of events are indistinguishable from neutrino scattering signal. The main contributions in this case are provided by the ^{85}Kr and the ^{210}Bi

that are superimposed on CNO-neutrinos and a part of $\nu_{^7Be}$ spectrum. Another small contribution is provided by ^{214}Pb that is strongly reduced by the use of a filter that is able to identify these events by means of coincidence technique with a efficiency of 89%.

During the data taking, the experiment needed several operations: tuning of electronic systems, filling operations on liquid scintillator for both Inner Vessel and Outer Vessel (buffer purification) and also on the water of the external shield of the Outer Detector (water loops) in order to thermalize the liquid scintillator inside the Stainless Steel Sphere (SSS). After refilling operations of liquid scintillator, the events coming directly from the Radon decay, like the ^{214}Pd or the α particles like ^{218}Po and ^{222}Rn, can give rise to spikes in the dataset. In Fig.4.2 we show the effects of the count rates of Radon due to refilling operations. These spikes are visible at the beginning of data taking (after the first filling), in June of 2009 and in March of 2010. We have decided to remove these data (1-2 week for each spike) to improve the stability of data time series.
Most of the background elements introduced by the refilling can be drastically reduced by means of the tagging method or by means of the Gatti's parameter selection as for the ^{210}Po (close to 99%).
The most dangerous background component is the ^{210}Bi. This element decay through the β-channel ($T_{1/2} = 5\,day\,(\pm 5\%) \quad Q = 1162.1\,keV(\pm 8\%)$) with a spectrum ranging within $0 < T_e < 600\,npe$ in charge (`m4charge_noavg`). Therefore this decay is impossible to distinguish from Compton's spectrum of electron-neutrino scattering, because they are overlapped. It has another dangerous feature: it is not stable but increases in time like a slow exponential during all data taking period as showed in Fig.4.9. Its increasing may be explained with the convective motion of the liquid scintillator in the inner vessel. The nylon of the vessel is rich of this element and liquid scintillator that rises close the vessel brings on the top this element that goes down in the center of the detector. This increasing of count rates seems not to influence much the possibility of identifying the $\nu_{^7Be}$ shoulder, but it could give some distortion to the signal when the count rates becomes higher at the end of data series.
The operations on the liquid scintillator of the Inner vessel, together with the temper-

ature changes, has also another effect: the inflation of internal nylon vessel as shown in Fig.4.3 (a). This inflation and deflation also influences the time stability of contribution from external background. Because of the different density of liquid scintillator between the inner vessel and the buffer region, especially if the inner vessel is not well inflated, the nylon vessel is pushed up because it is slightly lighter than the buffer liquid. This generates an asymmetry between the top and the bottom regions of the detector for the external background contribution (^{208}Tl and ^{214}Bi), which is provided mainly by the PMTs. At very high energy at $T_{charge} > 1000\,npe$ the count rate of ^{208}Tl-peak is modulated from the Vessel shape and its position compared to the Stainless Steel Sphere (SSS) in which are located on the photo-multipliers. If we compare the time evolution of Inner Vessel Volume in Fig. 4.3.a) with the evolution of thallium peak in Fig. 4.3 (b) it is visible an anti-correlation: when the Volume decreases and then nylon vessel goes up to the top, the count rate increases. When there is a new inflation, by means of refilling, the count rates goes back to the lower rate.

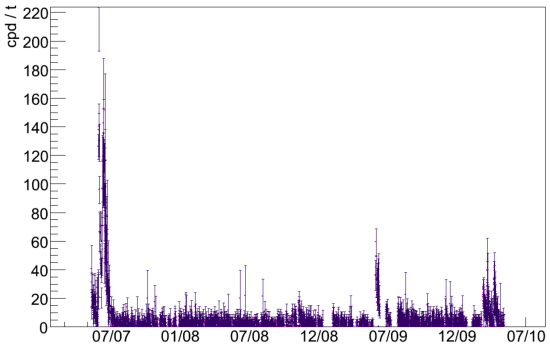

(a) Lead Time Variation

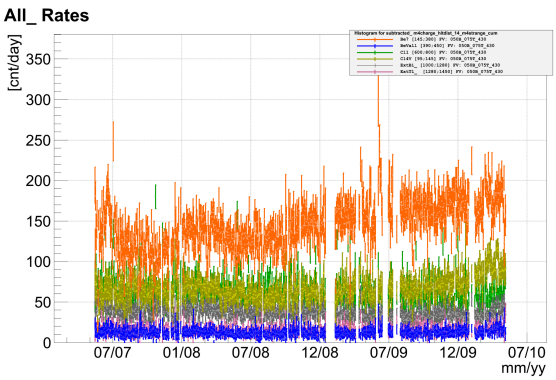

(b) Energy Windows Rates

Figure 4.2: Time variation of Lead ^{214}Pb measured by means of time coincidences method during all 3 years of data taking. The spikes are well visible due to filling, at the beginning, and also after the refilling operations in the middle of 07/2009 in figure a). These temporary increases of count rates for the Lead, and then for the Radon, give rise to increase of count rates also for Beryllium shoulder (orange points in figure b)). Fortunately, we can remove these events by means of time coincidence tagging.

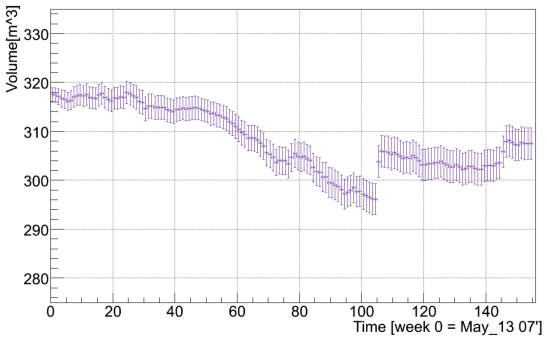

(a) Volume Time Variation

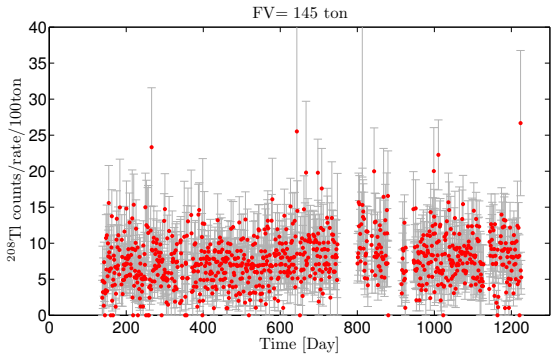

(b) Data for ^{208}Tl Time Variation

Figure 4.3: The time variation of volume of Inner Vessel changes also the counts rate for the external background at high energy. The figure b) shows us the count rates of ^{208}Tl peak was influenced by Volume time variations.

4.2.2 Energy Range and FV Selection

The Borexino spectrum in Fig.4.4 is composed by several background components that, if unstable, could modify the count rates of the energy windows in which they are dominant. These could introduces small distortions in the dataset that we are

analyzing. To perform the analysis we have done a study of small fluctuations of dataset on a long period, in a small portion of the spectrum in which the solar neutrinos spectra are dominant. We divided the spectrum in different regions which were present different spectral components between background and neutrino spectra:

- 90-105 npe for $(^{14}C + \nu_{pp} + {}^{14}\mathrm{C}_{pup})$
- 105-380 npe for *"wide"* Spectral components
  $(^{14}\mathrm{C}_{pup} + \nu_{pp} + \nu_{pep} + \nu_{CNO} + \nu_{^7Be} + {}^{210}\mathrm{Bi}_{bkg} + {}^{85}\mathrm{Kr}_{bkg})$,
- 210-380 npe for *"high"* Spectral components
  $(\nu_{pep} + \nu_{CNO} + \nu_{^7Be} + {}^{210}\mathrm{Bi}_{bkg} + {}^{85}\mathrm{Kr}_{bkg})$,
- 300-360 npe for *"narrow"* Spectral components
  $(\nu_{pep} + \nu_{CNO} + \nu_{^7Be} + {}^{210}\mathrm{Bi}_{bkg})$,
- 380-460 npe for $(\nu_{pep} + \nu_{CNO} + {}^{210}\mathrm{Bi} + {}^{11}C)$
- 600-800 npe for $^{11}\mathrm{C}$

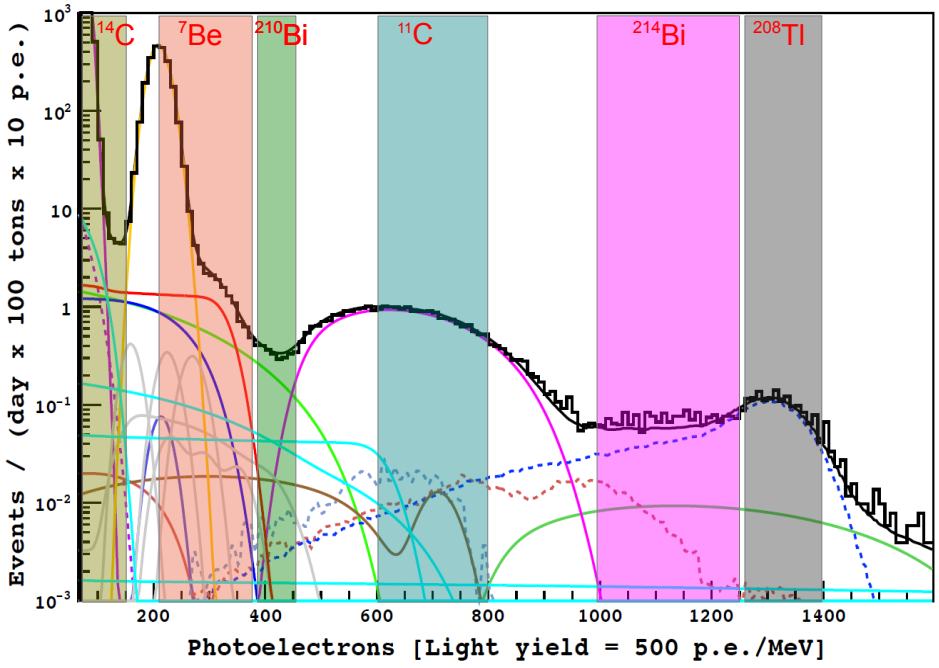

Figure 4.4: Energy windows for different background components. In each energy window there is the dominance of a particular background element.

– 1000-1280 npe for beta events from ^{214}Bi+ External Background

– 1280-1450 npe for ^{208}Tl, the thallium peak at T_e=2.6 MeV.

The energy ranges are expressed in charge `m4charge_noavg` [1] (*"number of photoelectrons" npe*) because, as already shown in section **??**, it is much more stable in time compared with the other charge variables. Another reason is that in this way the results are directly comparable with the measurement of ^{7}Be flux analysis [91].
By means of Gatti's parameter selection [**?**], we can distinguish between the α-events (positive value) and β-events (negative values). Among the β-events there are also present neutrino-electron scattering events, indistinguishable from the real β-events of background. By making a bi-dimensional fit in the Gatti-Charge space, showed in Fig.4.5 (a), we perform a cut of all events within 3σ from the center of ^{210}Po Gaussian peak, in which the ^{210}Po α-events are represented, in first approximation, by a bi-dimensional Gaussian function. In this way we lost about 66% of total β-events in the energy range considered ($105\,npe < T_e < 380\,npe$).
The percentage of relative count rates for all components, after the α/β cut, are reported in Tab.4.1 for two energy windows that we took into account for this analysis: $\Delta T_e = 105 - 380\,npe$ and $\Delta T_e = 210 - 360\,npe$. These percentage are evaluated from the spectral shape of Monte Carlo reproducing the analytical fit results of Borexino spectrum.
To perform the simulations, we consider only the main components in the energy region of neutrino shoulder: the solar neutrino rate of ^{7}Be, plus the slow exponential of Bismuth ^{120}Bi and the constant component of ^{85}Kr shown in Tab.4.1.
In Tab.4.2 we have reported an estimation of expected values for the Signal to Noise Ratio (SNR), at different sizes of energy windows and with different masses for the fiducial volumes. As a signal, we have considered the amplitude of seasonal modulation flux. Instead, for the noise, we took into account the standard deviation of background plus the one of the signal. To do this estimation we did not take into account the contributions of external background, that is negligible at small radii, but become im-

[1] The charge variable used is defined in the section...

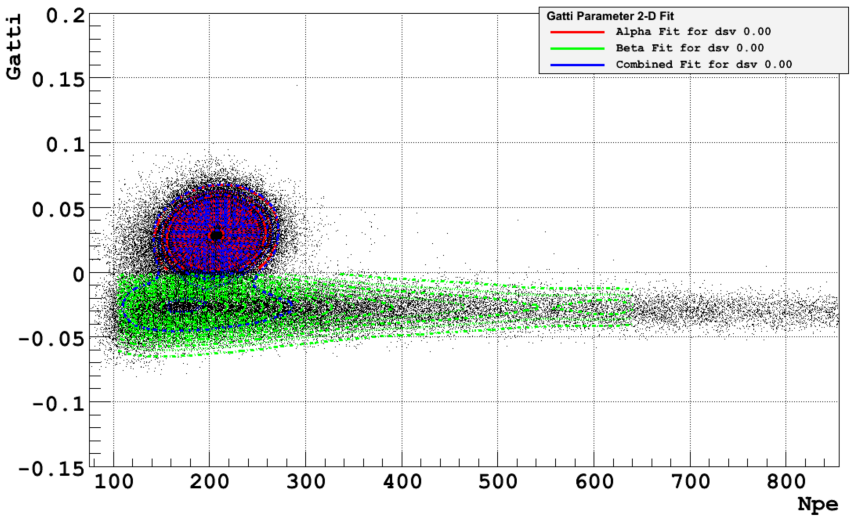

(a) Bi-dimensional Fit Gatti charge

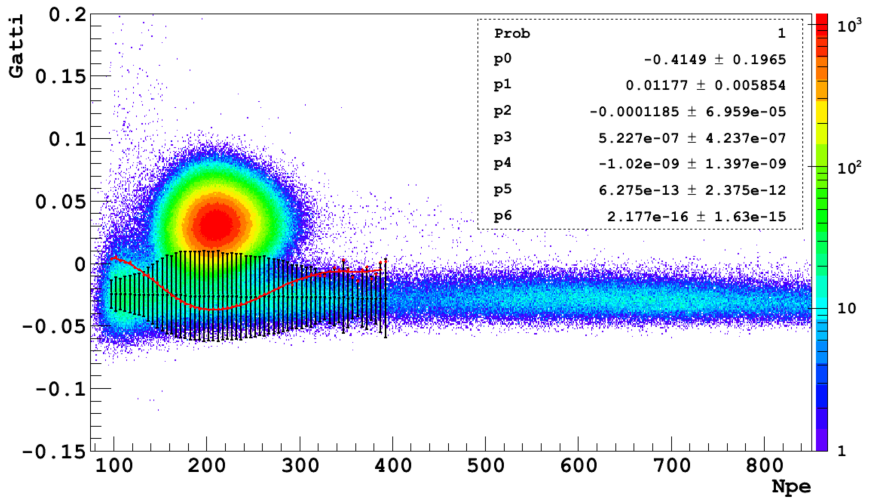

(b) α/β statistical cut

Figure 4.5: Gatti vs Charge space for the Borexino spectrum. The red line shows the α/β statistical cut that reduces the total number of events by 66% in the $\Delta T_e = 105 - 380\,npe$ energy range.

portant to radii larger than $r > 3.75\,m$ (or $\Delta r = r_{IV} - r_{FV} = (4.25 - 3.75)\,m = 0.5\,m$).

In the second step, we have to understand if there are similar fluctuations in the closest energy regions, because these could be an indication that the modulations might be driven by some background components.

From the fit results, we can see that the intensity of neutrino count rates is enough to

β-spectrum	% [105-380] npe	% [210-380] npe	Tot [cpd/100]
^{14}C	3.1×10^{-6} %	0.00 %	3.5×10^{6}
$^{14}C_{Pile-up}$	0.80 %	0.00 %	95
^{210}Bi	53.06 %	17.98 %	41.5 ± 1.5
^{85}Kr	48.78 %	9.45 %	29 ± 5
^{7}Be*	18.11 %	0.00 %	46.0 ± 1.5
^{7}Be	53.02 %	26.65 %	46.0 ± 1.5
^{13}N	53.20 %	16.34 %	2.36
^{15}O	49.72 %	23.56 %	3.36
pp	2.00 %	0.00 %	133 ± 0.8
pep	44.41 %	24.28 %	2.8 ± 0.3
SNR	0.93	1.36	–

Table 4.1: Percentage of total counts rate for each spectral component in two energy windows considered, expressed in charge variable: `m4charge_noavg`. In the last line, we also show the signal to noise ratio between the $\nu_{^7Be}$ and the background.

FV	SNR = $\Delta\Phi_0(7\%)/\sqrt{\sigma_S^2 + \sigma_B^2}$ (S/N)		
[100ton]	[140-380] npe	[210-380] npe	[300-360] npe
0.75	0.2058	0.1722	0.1064
1.50	0.2331	0.2415	0.1498
2.80	0.39	0.3311	0.2051

Table 4.2: Signal to Noise ratio for signal modulation for different energy windows and different FVs. The energy ranges are expressed with the charge variable `m4charge_noavg`.

be dominant as compared to the background components. The maximum amplitude of seasonal modulation of the neutrino flux is about 7% of the mean value measured in the total flux analysis. This means that for the case of new FV = 145 tons and energy window of $\Delta T_e = 105 - 380\, npe$, the $SNR = 0.2$. Therefore, the real signal that we want to measure is extremely weak as compared to the Poissonian statistical fluctuation. The EMD method, in this case, performs a filtering of all high frequency

components (mainly noise), leaving, in the latest modes functions, only the residual at low frequency like the seasonal component and, in the very last IMF, the trend of background components showed in Fig.4.15.

These ratios were not stable in time during whole data taking period due to increase of ^{210}Bi.

In order to enlarge the fiducial volume, we had to take into account the nylon balloon movements of Inner Vessel (IV). After its perforation, happened around the April 2008, and because of the leak of the internal liquid scintillator in the buffer region, the IV deflated losing about 17 m^3 of its initial volume as shown in Fig.4.3. Because of its deflation it lost also its spherical shape, but preserved a cylindrical symmetry with respect to the z-axis. By using the algorithm defined in section §2.5.4, we were able to identify the position of the surface of the nylon balloon, by means of the weekly datasets (*dst*), with an accuracy of $\sigma_R = \pm 20\, cm$. Starting from this profile, upon which we projected the entire surface of the IV sphere, in polar coordinates, we set a distance from it, to define the limits of new FV. Because of the background asymmetry, related to vessel shape position shown in Fig.4.6, we decided to choose different distances from the vessel for the top side (80 cm) equatorial side (75 cm) bottom side (60 cm) showed in Fig.4.6. Moreover, to eliminate the background contribution related to the end cups of IV, we performed a cut in the top and bottom side with a narrow parabola:

$$z(\theta) = \frac{d}{\cos^4 \theta} \tag{4.6}$$

in polar coordinate where $d = 2.60\, m$ from the center of detector.

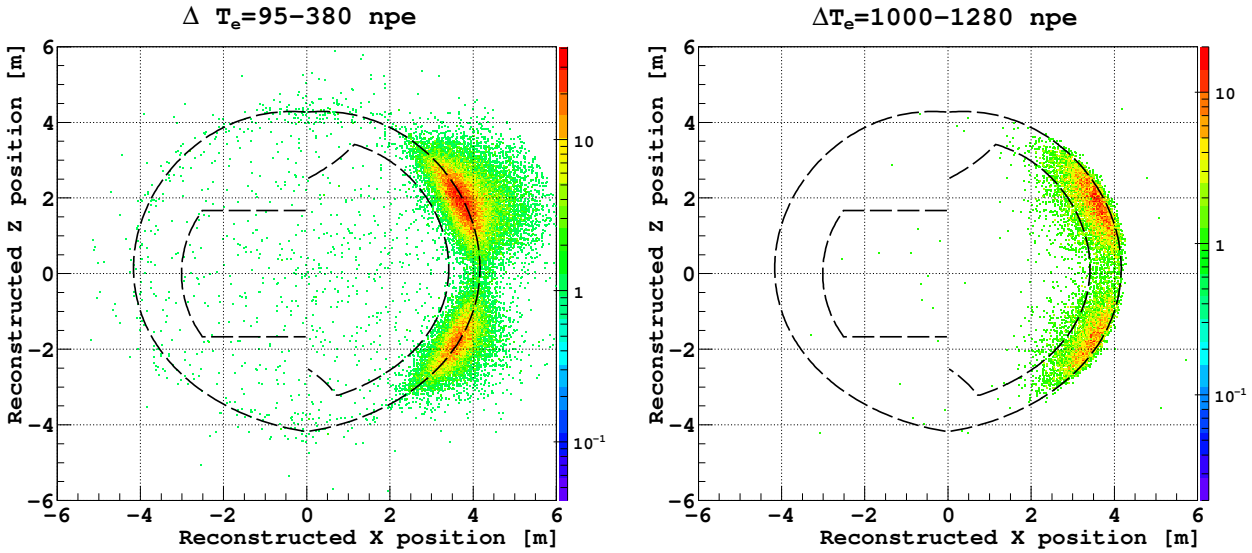

(a) External Background in the energy window $95\ npe < T_e < 380\ npe$

(b) External Background in the energy window $1000\ npe < T_e < 1280\ npe$

Figure 4.6: Penetration inside the Inner vessel of external background events simulated with a source of Thorium ^{228}Th of 3 MBq at different energy windows. These images show that, also with a very intense source, the number of event beyond 75 cm from vessel are negligible, also at the same energy of Beryllium spectrum.

4.3 Borexino Events Simulation

In this section we describe the simulations of Borexino dataset to test the Empirical Mode Decomposition behavior in the case of very low signal to noise ratio.
Generating different dataset and looking at the IMFs of each simulation, we observed two main potentially dangerous phenomena:

1. The shape of IMF extracted from sifting algorithm changes with the initial conditions of the dataset.

2. The presence of mixing mode between two close IMFs. This means that the expected signal can be shared between two different IMFs.

From the simulations, we observed that these two phenomena disappear if we take the IMF average from several simulations of the dataset. In Fig.4.7 we show this effect where the blue lines are the IMFs with the signal extracted from 100 dataset simulated,

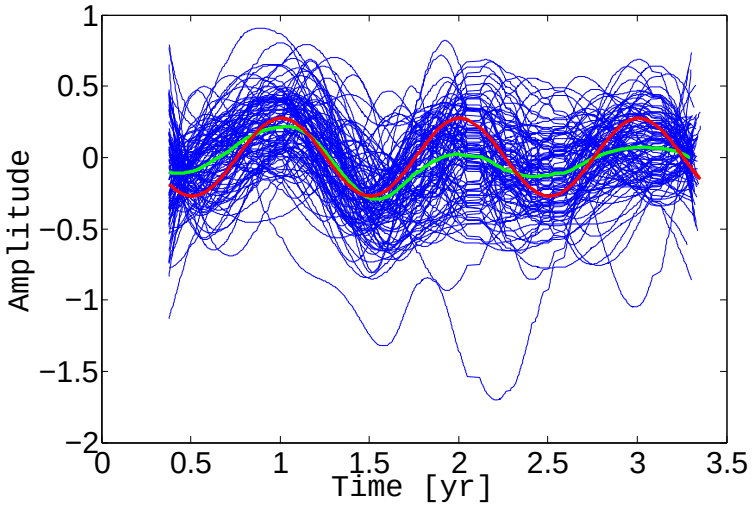

Figure 4.7: In green we show the average of all $IMF_{8/9}$ generated from Monte Carlo. The red curve is the expected signal used to generate the simulation. The decreasing of amplitude could be due to the increasing of exponential function for the background.

the light green line is the average of all of them and finally the dashed-red line is the expected signal.

The real data of Borexino are Poissonian and unrepeatable, so we cannot repeat a new data taking with the same detector conditions. The only way is to emulate different data taking by shifting the data points of a small quantity within the statistical error of 1σ. To apply this technique, also called *"Dithering"*, we sum up to the dataset a random noise with Gaussian distribution (White Noise). As we will show in the next sections, we have done these simulations to choose the parameters of dithering (the sigma of Gaussian distribution) and to understand the real sensitivity to the amplitude, phase and frequency of modulating signal.

The last issue of the dataset was the presence of gaps between the data points from few days up to two weeks long, after the calibration campaigns. The lack of data for several days, in the dataset, compromised the efficiency of the sifting algorithm when it decomposed the initial dataset in intrinsic mode functions. In order to improve the performance of sifting, we filled the empty time bins with random events during the dithering application. Also in this case the random events had a Gaussian distribution,

but the sigma was the root square of mean count rates of the whole dataset.
In the next sections we will describe how we defined the Borexino-like dataset and in particular how we simulated the same signal-to-noise ratio of dataset. Then we will show the results to select the parameter for the dithering and the test of coverage for the sensitivity to signal features. In the last section we will apply all these techniques on the real dataset and we will show the main results.

4.3.1 Signal-Background Generator

To simulate the real dataset, we consider the daily count rates of the low energy region, in which the Compton spectrum shoulder of electron-neutrino scattering is present. Starting from the Tab.4.3, we used a percentage of the total spectral shape integral for the main components in the energy window considered, in order to reproduce, with a good approximation, the real signal-to-noise ratio. Therefore, to generate the statistical fluctuation of real data, we used a random generator with Gaussian distribution and a mean value equal to zero. The sigma of the Gaussian distribution was equal to the square root of expected count rates for each component. In this way we simulated the statistical noise for each component and then we summed all these components to obtain the real dataset.
In Fig.4.8 we made a comparison between the simulated signal and real one. The ^{85}Kr is assumed to be constant in time from a direct measurement by mean of coincidences method **??**. Its contribution in the energy range

$$210\, npe < T_e < 380 npe$$

was of 22% percentage of its total spectrum. In the case of the ^{210}Bi and the $\nu_{^7Be}$, we summed two random noise to two functions respectively:

– The slow exponential function for the ^{210}Bi:

$$\Phi^{210}(t) = \Phi_0^{210} \exp\left(\frac{t}{\tau}\right) \tag{4.7}$$

where $1/\tau = 0.34 \pm 0.02\, [yr^{-1}]$.

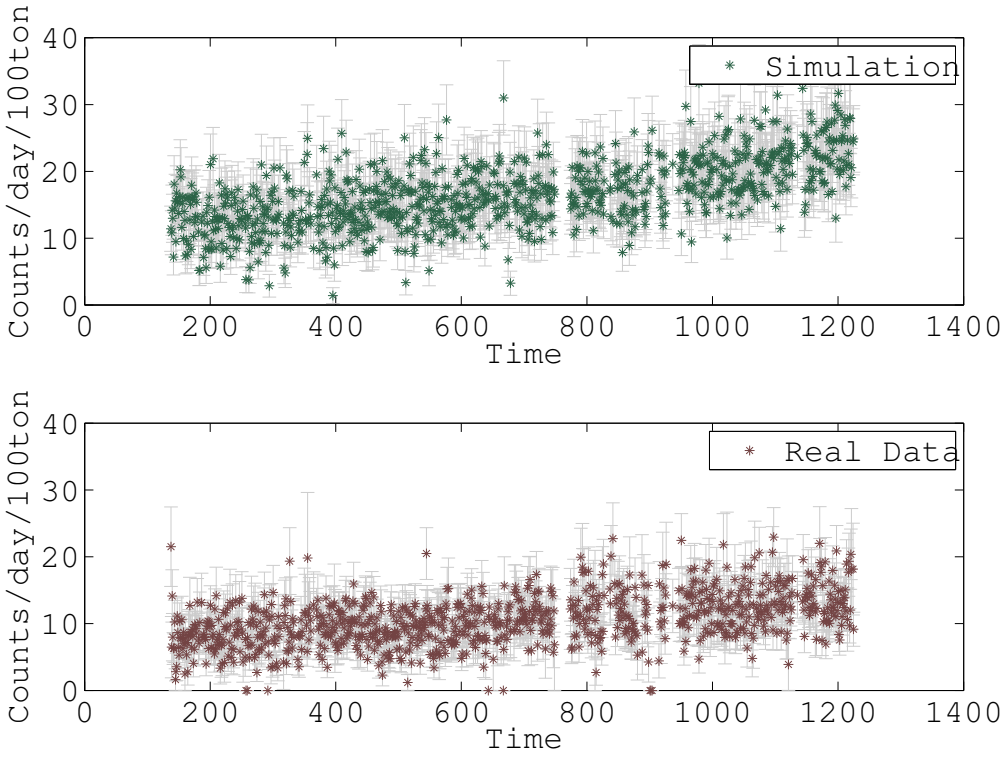

Figure 4.8: Exponential fit to describe the background increase during 3-year of data taking in the standard FV.

– The seasonal function is Eq.4.4:

$$\Phi^{^7Be}(t) \simeq \Phi_0^{^7Be}\left[1 + 2e \cdot \cos\left(\frac{2\pi}{T}(t - \eta_0)\right)\right] \tag{4.8}$$

where $\Phi_0^{^7Be}$ is the average rate measured by Borexino in 3 year of exposure and e is the eccentricity of the Earth's orbit.

For this simulation the amplitude of modulation expected is:

$$|\Delta\Phi^{\nu_{Be7}}| = 2e \cdot \Phi_0^{^7Be} \simeq 7\%\Phi_0^{^7Be} \tag{4.9}$$

For example the amplitude (peak to peak) of modulation for the $\nu^{^7Be}$ flux, in the energy range

$$210\, npe < T_e < 360 npe$$

is:

$$\delta\Phi^{^7Be} \simeq 7\%\Phi_0^{^7Be} = 1.15\, cpd/100 ton. \tag{4.10}$$

Component	$cpd/100ton$	% [140-380] npe	% [210-380] npe	% [300-360] npe
Be7	46.0	55.5%	35.9%	11.8%
Bi210	40.0	46.5%	27.3%	8.3%
Kr85	30.5	48.1%	22.6%	2.9%

Table 4.3: Percentage fractions of counts by performing the integral of spectral shape in different energy range expressed in `m4charge_noavg`.

This means that the expected amplitude for the IMF is:

$$A_{IMF} = 0.57 cpd/100ton \tag{4.11}$$

that correspond to $SNR = 0.2$.

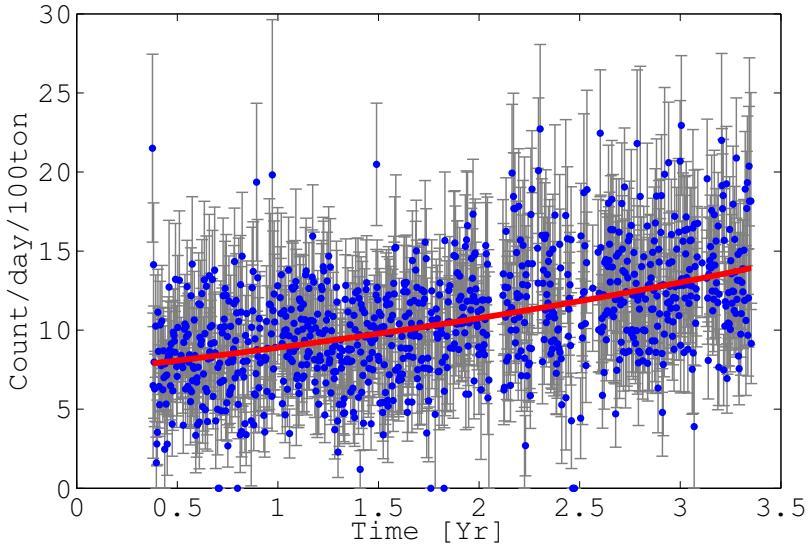

Figure 4.9: Exponential fit to describe the background increase during 3-year of data taking in the standard FV.

4.3.2 Dithering

In this section we performed several simulations to define the best value of the sigma of the Gaussian distribution to generate random events in order to eliminate the overlapping between the modulating signal, present in the dataset, and the statistical fluctuation of data. We applied the dithering to the dataset in the following way: the first step was to generate the dataset with its own random noise, as described in the previous section. For the second step we have two equivalent ways to proceed: in the first method, that we used for this work, we filled the empty days of dataset with random events having the same features of simulated data. Then we summed to this new dataset a vector of white noise events with the same length. We applied to this new dataset, now without gaps, the sifting algorithm to evaluate the frequency, the amplitude and the phase as defined in the chapter **??**. With the values found, after 100 reiteration of this procedure, we filled the histograms in Fig.4.17 obtaining the distribution showed for each parameter.

To define the final mean values for the parameters of the IMF considered, we made a Gaussian fit of their distributions. We repeated again these steps 10 times for each value to test of the σ_{dith}. As reference dimension for this parameter, we considered the average of bin errors for the whole dataset. For the Poissonian distributions the value is equal, in good approximation, to the square root of the bin content. We chose the dimension of σ_{Dith} as a small fraction of this error, starting from very small fraction to the total bin error value (100%):

$$\begin{aligned} \sigma_{Dith}\,[cpd/100ton] = \; & \{0.1\%, 0.5\%, 1.0\%, 3.5\%, 7.5\%, \\ & 10.0\%, 16.0\%, 35.0\%, 70.0\%, 100\%\} \end{aligned} \tag{4.12}$$

For each value showed in Eq.4.12 for σ_{Dith}, we took the mean of χ^2 evaluated in each of 10 simulations as it follows:

$$\chi^2 = \frac{\left(\mu_i - \mu^{Th}\right)^2}{\sigma_i^2} \tag{4.13}$$

in which μ_i is the value of the parameter measured from the IMF, σ_i is the associated error and μ^{Th} is the expected results. We plotted the results in Fig.4.10, where each

point is the average of the results from the 10 simulations. From these simulations we found that the best value for the σ_{Dith} of Gaussian distribution is the 10% of the mean of the bins error from eccentricity results. For the frequency it seems that, increasing the dithering parameter, the χ^2 further decreases, but we get a worse eccentricity results.

We applied these results in the next sections to check the sensitivity of this method for the features of the modulating signal used to generate the dataset. The second method, to perform this kind of analysis, is a little bit different. Instead of extracting 100 times the IMFs and getting the mean values of parameter distributions, we summed 100 times the dithering to the dataset and then we applied the sifting algorithm, in order to extract the IMF and evaluate the amplitude and the mean period of the IMF in which the seasonal modulation is present. The results were more or less equivalent, but the first method seemed to be more efficient in extracting the IMF with a shape closer to the expected one.

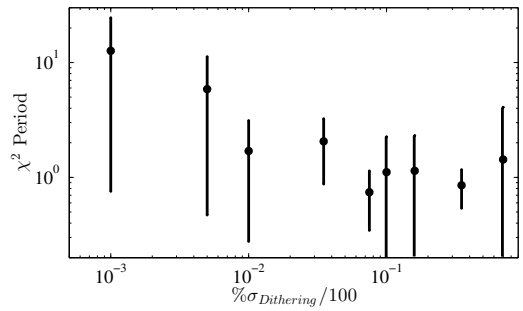

(a) χ^2 average from 10 Simulation for the Period

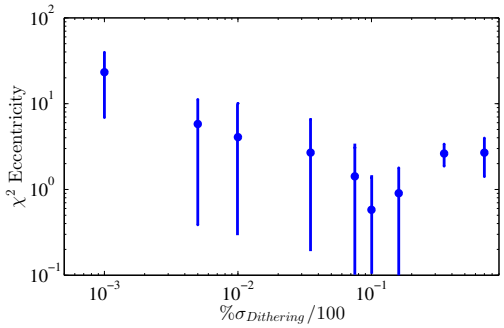

(b) χ^2 average from 10 Simulation for the Eccentricity

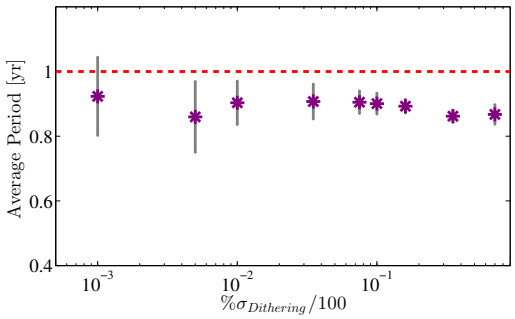

(c) Average periods results from 10 Simulation

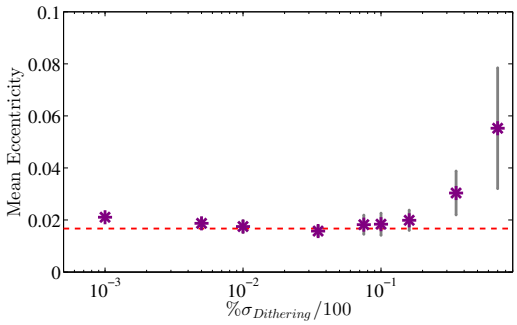

(d) Average Eccentricity results from 10 Simulation

Figure 4.10: On the left column it is showed the χ^2 average (a) and the period values average (c) results from 10 simulation ($T = 1\,yr$). On the right column there are same results for the Eccentricity ($e = 0.0167$). The best values for both the parameters are taken at $\sigma_{Dithering} = 10\%$.

4.3.3 Eccentricity Change

We were looking for the limits of Empirical Mode Decomposition to identify the modulating signal present in the dataset. In this section we tried to change, in our simulations, the amplitude of the eccentricity of the Earth's orbit of $\pm 10\%$, $\pm 20\%$, $\pm 35\%$ and $\pm 50\%$ starting from initial value of $e = 0.0167$.

This test was necessary to understand what is the signal amplitude threshold and if the EMD is able to distinguish between the different cases. This test was also important to understand the role of noise for the estimation of signal amplitude.

In Fig.4.11 we plotted the results starting from the green star that represents the value for the Earth's orbit eccentricity. On x-axis we put the input values for the

eccentricity for the simulation and on y-axis the respective measured values for a FV of 150 tons. The results showing a good agreement, within the errors, with the red dashed-line for the expected values. The method also showed the amplitude limit in which we could see, in same conditions of signal-to-noise ratio, the presence of the signal. In particular, for a fiducial volume of 150 tons and the narrow energy window of $300\,npe < T_e < 360\,npe$ used for these simulations, the method was able to extract the signal with an eccentricity reduced of 20% of Earth orbit eccentricity: $e \geq 0.0134$. For values smaller than this one, the points remained greater than the theoretical values. This value is exactly $e \geq 0.0134$. This threshold might depend on uncertainty due to the fluctuation noise or the presence of a threshold for the S/N ratio between the signal and noise contribution. By means of this exercise it could be posed a general limit of method, starting from SNR. In this case we showed that our technique was able to be sensitive for the weak signals like the seasonal fluctuation of solar neutrino.

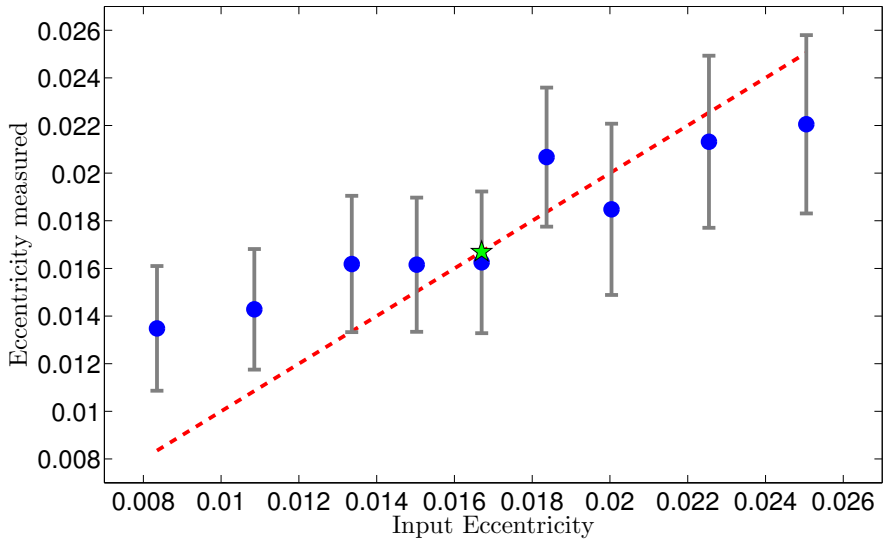

Figure 4.11: Simulation of seasonal signals with different eccentricity values. Starting from the real value (green star) we added and subtracted to this eccentricity the ±10%, ±20%, ±35%, ±50% as shown on the x-axis. The results found by means of EMD method were in agreement within the error. When the eccentricity became too small, the EMD failed.

4.3.4 Phase Change

Another important check concerned the sensitivity of method for the phase determination. We want to understand if changing the phase or summing another signal with a $\pi/2$ and π of phase shift, we would have found the same trigonometric results for the sum of two cosine functions.

In order to do this test, we took two seasonal-like functions with a different phase and then we summed together the modulating parts Σ:

$$\Sigma = \Phi_0 \times \left[\left(1 + e\cos\left(\frac{2\pi}{T}(t-\eta_1) \right) \right)^2 + \left(1 + e\cos\left(\frac{2\pi}{T}\left(t - \eta_1 - \frac{\pi}{2} \right) \right) \right)^2 - 1 \right]$$

$$\simeq \Phi_0 \times \left[1 + 2\sqrt{2}e\cos\left(\frac{2\pi}{T}\left(t - \eta_1 - \frac{\pi}{4} \right) \right) \right] \tag{4.14}$$

Therefore, we generated a new dataset adding to this signal the white noise and then we performed the EMD analysis.

The analytical result is shown in Fig.4.12 with the red line that is a signal increased of $\sqrt{2}$ and a signal shifted of $\pi/4$. From the simulation results, shown in Fig.**??**, putting this signal in the count rates, we obtain the same features of the analytical result. In this way we showed also that the method was really sensitive to the presence of a signal with particular characteristics and that the IMF were not a random coincidence. We expected instead to find a random phase and frequency variation in the case of absence of a signal, i.e. in the case where we summed two signals with opposing phases.

4.4 Real Data Analysis

4.4.1 Dataset Definition

We used 3 years long dataset already selected to perform the ^7Be neutrino flux measurement in [91]. This dataset started from 16 May 2007 to 10 May 2010, for a total exposure of 740.7 live days. As it is already shown in the section §**??**, we used the charge variable `m4charge_noavg` because it was much more stable in time, as com-

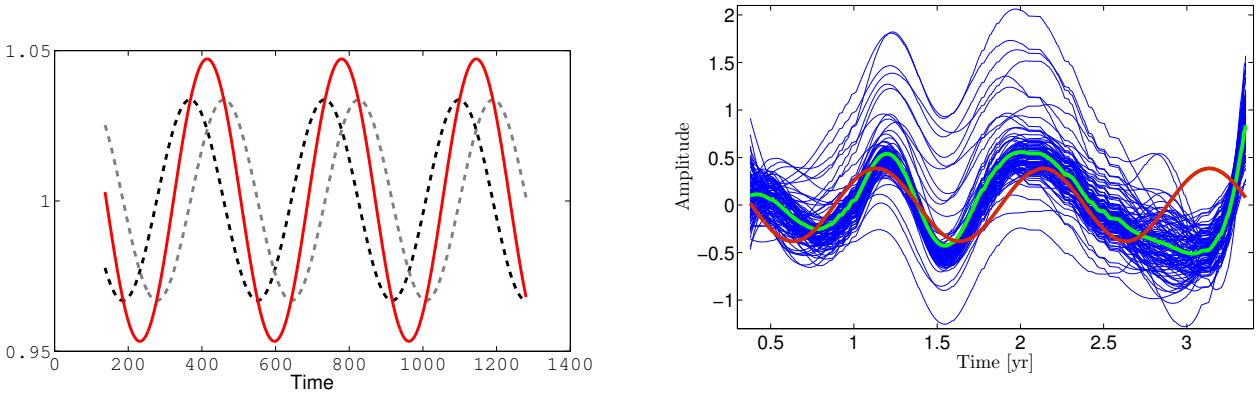

Figure 4.12: Example of summing of two seasonal-like signals with different initial phases used to check the phase sensitivity of method. The red sinusoid is the resulting function that we wanted to find in our simulated data. On the left the expected trigonometric result; on the right the IMF in which is present the signal in phase with the expected result.

pared with the other charge variables available in our analysis framework.

For this dataset, also called Borexino Phase I, it was not possible to make the sum of the same months, year by year, because of background instability already discussed in section §4.2. There was a first natural subdivision of the 3 years long dataset in 8 datasets with different sizes in time, related mainly to different operations made on the detector. With this first subdivision, each dataset was homogeneous. But performing the fit, the analysis highlighted for the first time the background instability and, in particular, related to the increase of ^{210}Bi component.

For the first approach, discussed in the next section, we used a time binning of two months for the sinusoidal fit of data with two different methods.

For the EMD method, instead, we used a 1 day binning in order to improve the performances of sifting algorithm and to take into account all possible variations of detected background.

In both cases of different time binning (1 day or two months), to increase as much as possible the number of events in the each dataset, we had to increase the dimension of Fiducial Volume (FV) considered.

4.4.2 A Preliminary Study on Data with a Direct Fit

As preliminary analysis, we did a direct fit of count rates present in the ν-Be7 shoulder region, between 280 - 380 npe (in charge variable `m4charge_noavg`). We used the Kepler's function in Eq.(4.4) plus a exponential function to describe both the seasonal modulation of neutrino flux and the increasing of background count rate.

To make this preliminary analysis, we also did a first rough FV cut setting the distance from the nylon surface of Inner Vessel (IV) fixed to $\Delta R = 0.75\,m$ and a cut on z-axis at $z_{cut} = \pm 2.0\,m$.

The background instability related to the Radon contamination and to the external background (because of the vessel movement), made this dataset, with two months long bins, unstable and the sinusoidal fit results were not consistent with expected results. At the same time, we tried to use another technique based on results from the spectral fit code.

Instead of using the count rates of each small two month dataset, we did the spectral fit 250 times for each 2-month dataset, varying the initial value of only two parameter to which the fit result was sensitive: the ^{85}Kr and the quenching factor for the ^{11}C spectrum. We took each time a random value for their initial values from a Gaussian distribution around their best values from the total fit. Then, with each one of the 250 fit results, we filled an histogram for each variable and then we took the average values from a Gaussian fit shown in Fig.4.13. In Fig. 4.14 we showed the fit results assuming the Kepler's equation Eq.4.4, imposing only a narrow range for the initial phase (from 0 to 3.5 days). The other parameters, like the total counting rate, the eccentricity and the period of sinusoidal function are left free with wider ranges. In the latter case, the measured value for the period was in good agreement with the expected value of $T_{Seas} = 365.24\,[day] = 1\,yr$ and the mean value for the count rates was in agreement, within the error, with the best value of total fit $\Phi_0^{^7Be} = 46\,cpd/100ton$ [91], but the eccentricity resulted to be about double compared to the expected one, with a very large error (67%).

The fit procedure allowed to take into account the presence of spikes in the count rates of Radon. It allowed to perform a measurement if beta events, even taking into account

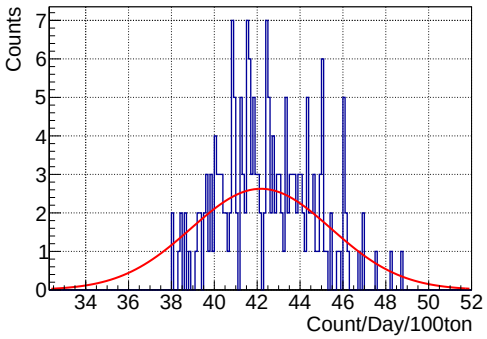

(a) Results for ν_{Be7}

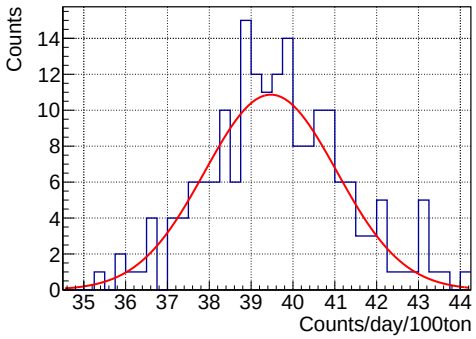

(b) Results for ^{210}Bi

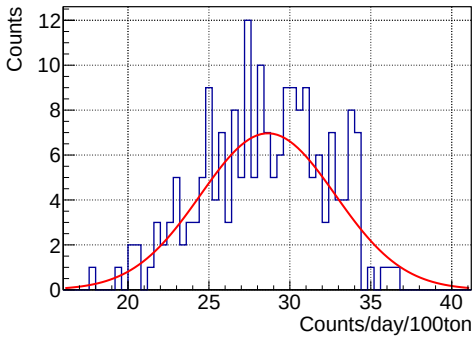

(c) Results for ^{85}Kr

Figure 4.13: First result obtained performing the whole spectral fit of data with two-months binsize. The error in y-axis correspond to error of mean value obtained from Gaussian fit of distribution of 250 spectral fit results. The error in x-axis correspond to real integration time.

all α-events (we did not make the α/β subtraction in this case) but the error associated to each point does not allowed us to obtain a small value for the χ^2.

These two possible methods to perform this analysis did not give us satisfactory results because of the large error and low statistic present in the dataset. These two reason constrained us to find a new method able to extract weak signals from very noisily and non stationary dataset. In the next section we showed the results applying the Ensemble Empirical Mode Decomposition (EEMD) of Borexino dataset, in which was done a much more careful selection of Fiducial Volume and a statistical subtraction of Radon and α events.

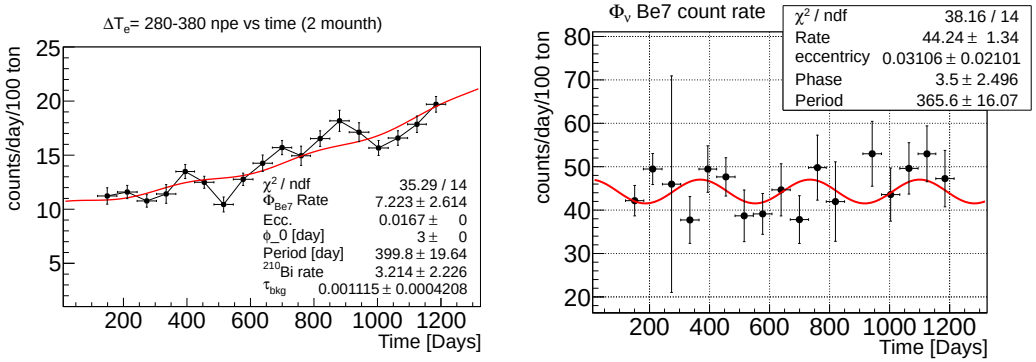

(a) Results for ν_{Be7} (b) Results for ^{210}Bi

Figure 4.14: First result obtained performing the whole spectral fit of data with two-months binsize. The error in y-axis correspond to error of mean value obtained from Gaussian fit of distribution of 250 spectral fit results. The error in x-axis correspond to real integration time.

4.4.3 EEMD Analysis of the energy range $T_e = 105 - 380$ *npe*

In the Borexino dataset there are gaps with different time lengths, usually one or two day, but in the year 2009 there were much more long interruptions because of calibration campaigns up to two weeks long. We filled these gaps with white noise and apply the procedure for the dithering described in the section § 4.3.2, without losing or modifying the information contained in low frequency in the dataset. Therefore, we evaluate by means of Gaussian fit of result distributions the parameters for the amplitude and frequency. We used these values to make the measurement of eccentricity and modulation period respectively:

– Period:

$$T = \frac{1}{\omega}; \qquad \Delta T = \frac{\Delta\omega}{\omega^2}; \tag{4.15}$$

– Eccentricity:

$$e = \sqrt{\frac{a(z)}{\Phi_e^{7Be}}} - 1; \qquad \Delta e = \frac{1}{2\Phi_e^{7Be}} \frac{\Delta a(z)}{\sqrt{e}}; \tag{4.16}$$

The IMF extracted from the sifting algorithm are showed in fig.4.15. The noise related to the statistical fluctuation was absorbed mainly in the first 5 IMFs, in which there are the high frequency components. These components with high frequency do not carry any kind of information. The physical informations, in our case, are present in

the latest IMFs where the low frequency components are dominant. The frequency that we are looking for, is the seasonal modulation:

$$\nu_{Seas} = \frac{1}{365.24\,[day]} = 0.00274[day^{-1}] \tag{4.17}$$

because of the properties of dyadic filter of the sifting algorithm, we can anticipate in which number of the IMF we can expect to find the seasonal modulation. The maximum number of IMF that we can obtain from a correct sifting is related to the number of data points in the dataset: n_{bins}. We have that the maximum number of IMF is:

$$N_{IMF}^{Max} = -\left\lfloor \log_2\left(\frac{2}{n_{bins}}\right)\right\rfloor = -\lfloor \log_2 \nu_{Nyquist}\rfloor \tag{4.18}$$

where the Nyquist frequency is half of sampling frequency $\nu_{sample} = 1/n_{bins}$. In our case we have $n_{bins} \simeq 1200\,bins$ and each bin is 1 day long. Therefore the maximum number IMF that we can extract is:

$$N_{IMF}^{Max} = -\left\lfloor \log_2\left(\frac{2}{n_{bins}}\right)\right\rfloor = 9 \tag{4.19}$$

in which the last one ($\mathrm{IMF}_{9/9}$) is the *trend* of dataset. Instead the number of the IMF in which we expect to find our seasonal signal is:

$$N_{IMF} = -\left\lfloor \log_2\left(\frac{1}{365.24}\right)\right\rfloor = -\lfloor \log_2 \nu_{Seas}\rfloor = 8 \tag{4.20}$$

Therefore we expect to find the seasonal signal, with a mean frequency $\nu_{Seas} = 0.00274$ $[day^{-1}]$, in the spectrum of the $\mathrm{IMF}_{8/9}$ that was exactly what we found in the data analysis shown Fig.4.18. In the upper figure we showed the *Time-Frequency* space in which there are the instantaneous frequency for all IMFs. In particular we showed only the frequency range where there is the instantaneous frequency of $\mathrm{IMF}_{8/9}$ in which the seasonal frequency is present. The dashed white line indicates the value of expected frequency. The color of the line indicates the amplitude of analytical signal associate to the IMF for each instant. To make the power spectrum in the lower figure we took the average in time of the squared amplitude for each value of the frequency. The green line is the power spectrum for all IMF except the last one (the trend), the red, blue and magenta line are the contribution to the total spectrum of the IMFs 8,7,6 respectively.

The power spectrum shows the feature of each IMF, if the sinusoidal signal is present the instantaneous frequency is close to be constant in time, as expected for a periodic function. In the case in which the signal was absent the power spectra has several peaks and a broad spectrum without a specific dominant component. This means that these IMFs are still dominated by the white noise and that do not carry any physical information. From the fit with a Gaussian function of the power spectrum, we evaluated the average of frequency for each IMF extracted after the application of the dithering and the filling of empty bins recursively for 100 times. In this way we filled the lower histogram in Fig. 4.18 (b) obtaining the frequency distribution of 100 IMF in which the signal is present. By means of another fit of this new distribution we define the average frequency of the signal present in our dataset. The same was done for the amplitude for each IMF. We expected that the amplitude should be constant in time, therefore we took the time average of amplitude for the analytical signal and then we filled the upper histogram in Fig. 4.18 (b). The Gaussian fit of the amplitude distribution tells us the average amplitude of our signal.

The last quantity necessary to define completely a periodic function is the initial phase. For the seasonal function the initial phase tells us the day in which the flux have the maximum, that is the January 3rd. Therefore the initial phase, expressed in day is $\varphi_0 = 3$. To obtain this value we fitted the phase function with a straight line:

$$\theta(t) = \langle\omega\rangle t - \varphi_0 \tag{4.21}$$

where $\langle\omega\rangle$ is the average of instantaneous frequency of each IMF. Therefore we subtracted $\langle\omega\rangle t$ to the instantaneous phase function $\theta(t)$ obtaining a constant residual function that indicate the value of initial phase. Unfortunately, the introduction of dithering generate a large family of parallel line that generate a broad distribution of initial values, but centred on $\varphi_0 = 15.47 \pm 9[day]$ with a large sigma of $\sigma_{\varphi_0} = 66 \pm 12[day]$. These results indicate that the best resolution that we had, was of 2 months ($\sim 60[days]$) that was also the best time resolution used to perform the direct fit with the sinusoidal function. Finally we plotted in Fig.4.20 the best fit results for the eccentricity and period for Borexino data that are in good agreement with the expected results for the Earth's orbit.

	$\Delta T_e = 105 - 380\, npe$		Earth $\oplus$
T_{Seas} $[yr]$	0.96	± 0.07 (9%)	1.0
e	0.032	± 0.004 (14%)	0.0167
φ_0 $[day]$	15	± 9 (60%)	3.0

Table 4.4: Final results of Seasonal Analysis with Empirical Mode Decomposition. Excepted for the eccentricity, that is in agreement within 3σ, both period and initial phase are in good agreement with expected values for the terrestrial orbit.

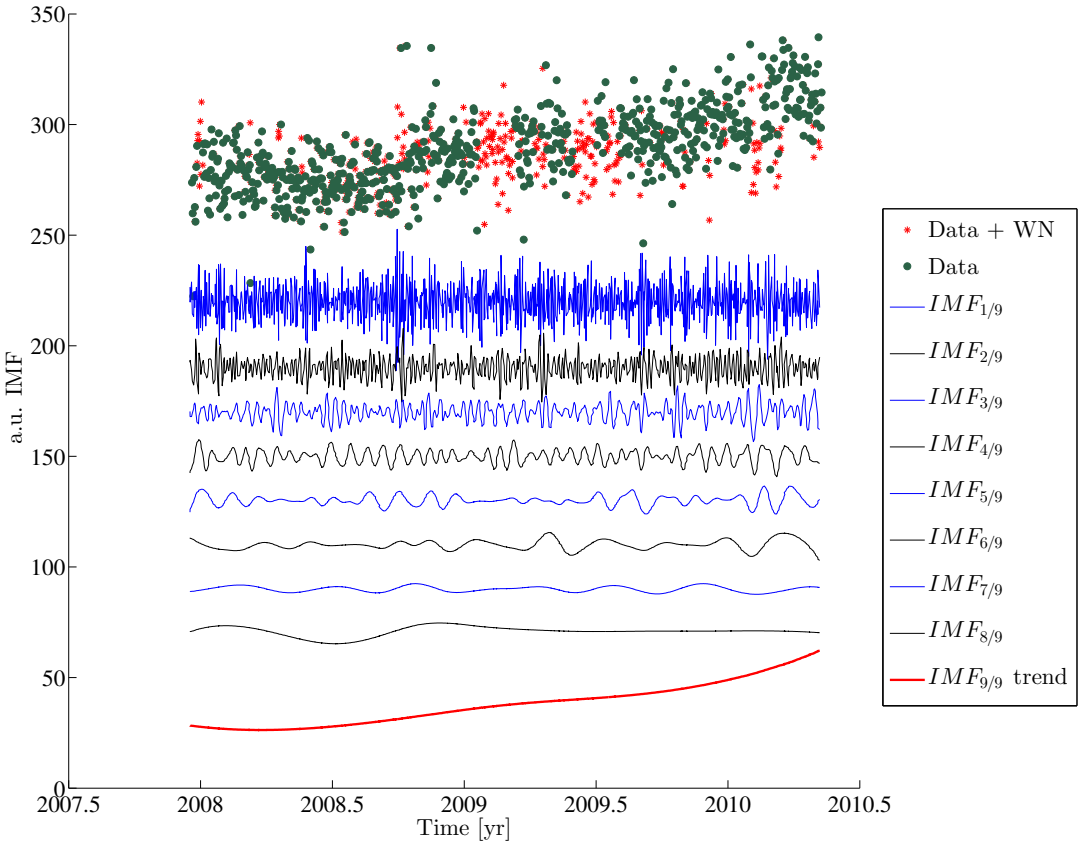

Figure 4.15: From initial data, sequence of IMF extracted by mean of sifting algorithm. We observe that the statistical noise is absorbed from the first 5 IMFs. A portion of real signal is visible in the last but one $IMF_{8/9}$ and in the last one we have a monotonic function called trend. The units on y-axis are arbitrary.

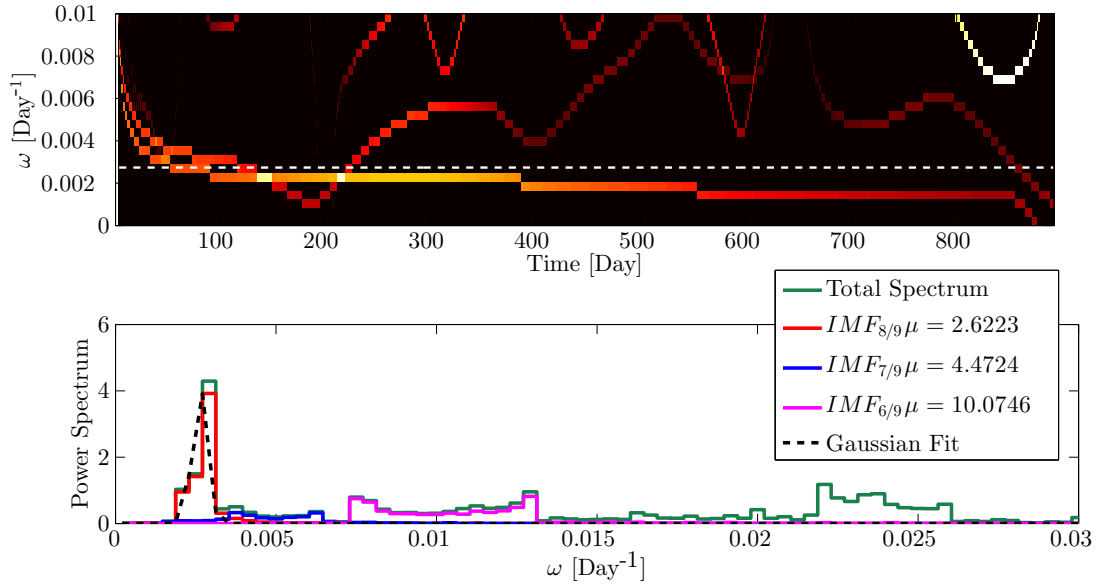

Figure 4.16: In the upper figure we showed the instantaneous frequency for the latest IMFs extracted from Borexino data and evaluated by means of time derivative of phase function $\theta(t)$. The line color indicate the amplitude of analytical signal. In the lower figure we showed the marginal power spectrum for the latest IMF components (red,blue and magenta) and for the whole set of IMFs (green).

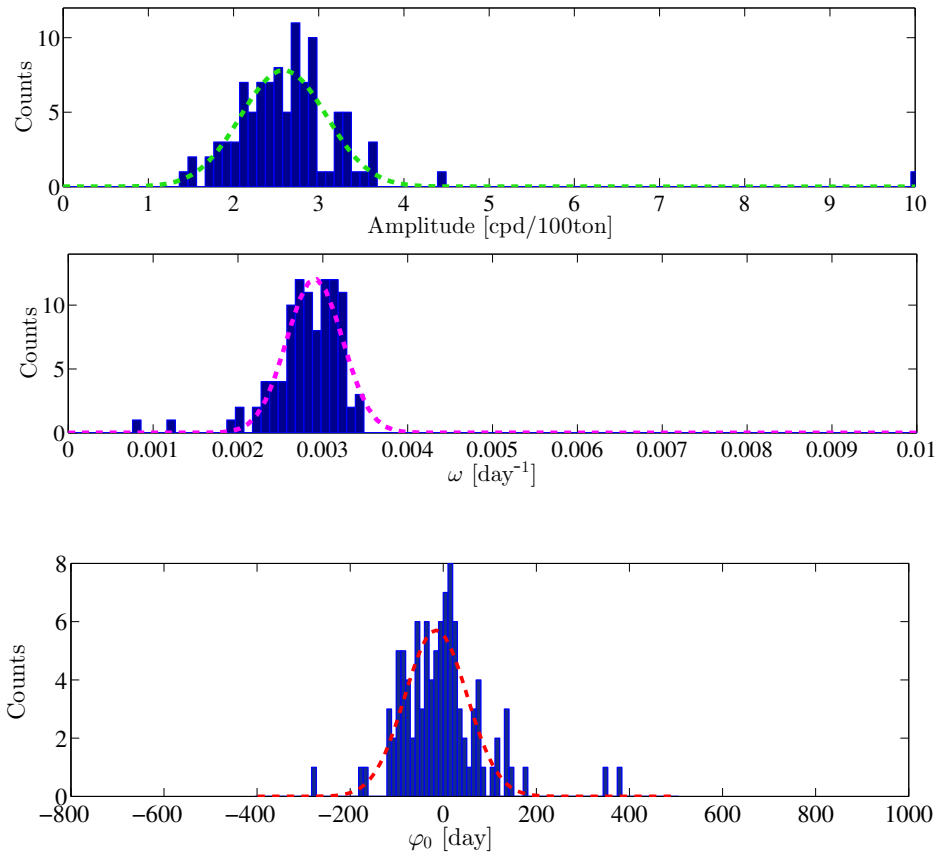

Figure 4.17: These three histograms represent the distributions for the amplitude and frequency and initial phase of the 100 IMFs after the dithering. The values expected for the seasonal signal are within 3σ compared the mean values of the $Amp = 1.36 cpd/100 ton$ and within 1σ for the $\langle\omega(t)\rangle = 2.739 \times 10^{-3}\ [day^{-1}]$. The Initial phase is in agreement within 2σ with the expected signal of $\varphi_0 = 3\ [day]$.

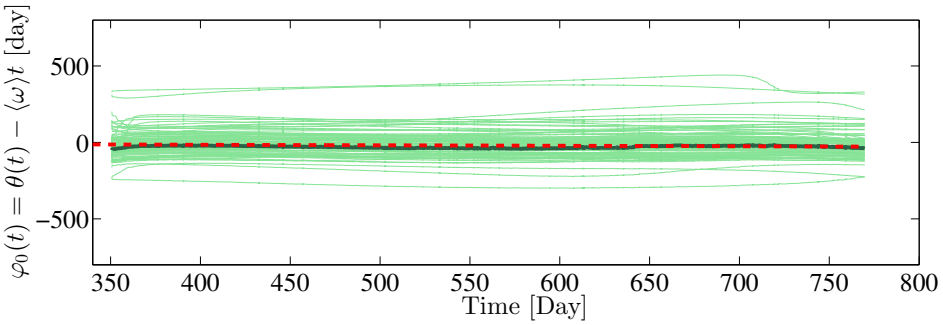

Figure 4.18: Initial Phase evaluation from the Phase function of analytical function of the $IMF_{8/9}$. In figure (a) we showed the constant behaviour of the residual function $\varphi_0(t) = \theta(t) - \langle\omega(t)\rangle \cdot t$. In figure (b) we had taken the distribution of time average for $\varphi_0(t)$.

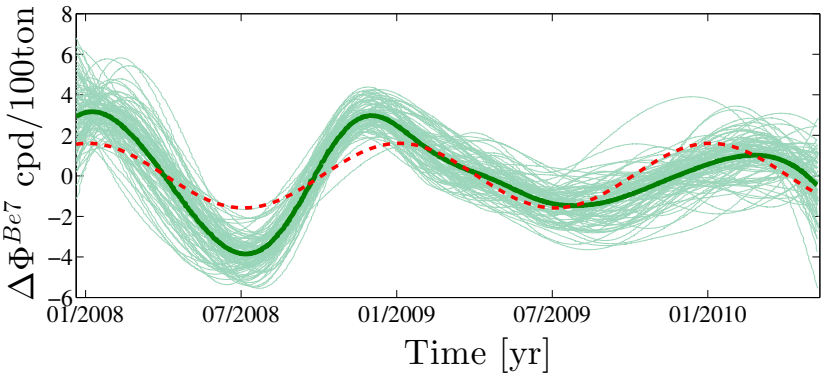

Figure 4.19: $IMF_{8/9}$ extracted from Borexino data by means of sifting algorithm. The dark green line is the average of 100 IMF (light-green line). The red-dashed line is the expected seasonal modulation for all neutrino contained in the energy range.

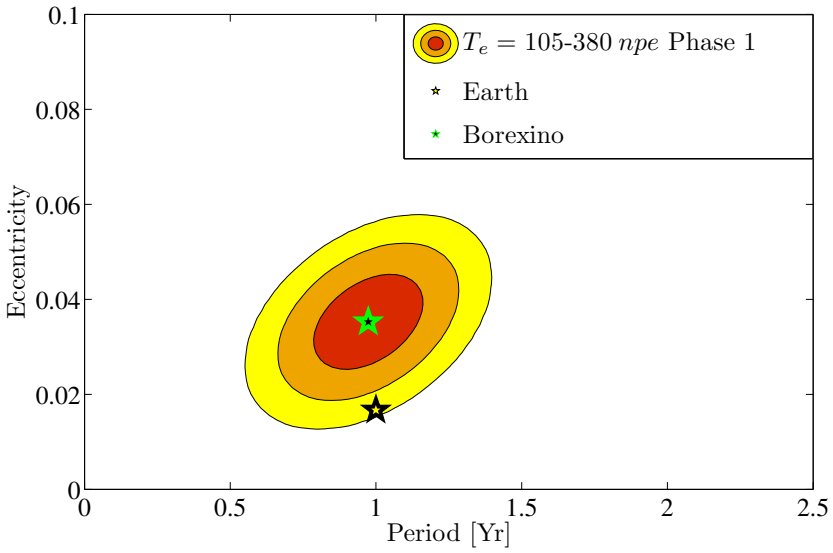

Figure 4.20: Gaussian fit of distribution of Eccentricity and Period points for 100 dithered IMF extracted by means of sifting algorithm. The black-yellow star are the expected values for the eccentricity and period, the light-green-black star are the central values of the Gaussian peak. The Red (1σ = 68% C.L.), Orange (2σ = 95% C.L.) and Yellow (3σ = 99.7% C.L.).

Chapter 5

New Matter Sensitive Observables

5.1 Introduction: Neutrino Global Fit and Non Standard Interaction

The non standard interactions may involve all the unsolved questions about the weak interactions. The future generations of neutrino experiments plan to perform the measurements of the CP phase and to investigate the neutrino masses hierarchy. To perform these kind of measurements we have to know with a very high precision the MSW parameters. The solar neutrino puzzle was definitively solved by mean of the results of reactor anti-neutrino experiment KamLAND [15, 12], that introduced a strong constraint on Δm^2_{12}, ruling out all possible solutions and leaving only two very small region on $\tan^2\theta_{12}$ vs Δm^2_{12} space. These two region are called Large Mixing Angle (LMA) ($\tan^2\theta = [0.3, 0.5]$ and $\Delta m^2_{12} = [10^{-5}, 10^{-4}]eV^2$) and LOW region with the same $\tan^2\theta_{12}$ range, but with a Δm^2_{12} range much more lower than LMA solution ($\Delta m^2_{12} \sim 10^{-7}eV^2$), as shown in the left-panel of Fig.5.1. The last Borexino results, that measured with a 5% of error the ^7Be solar neutrino flux [91], plus the low energy region of ^8B solar neutrino fluxes ($E_\nu \geq 3\ MeV$) [95], put an improvement to KamLAND results by ruling out also the LOW solution, but without appreciable changing for the LMA solution as showed in the right panel of Fig.5.1.

Performing the update for all neutrino experiment results as for SuperKamiokaNDE-

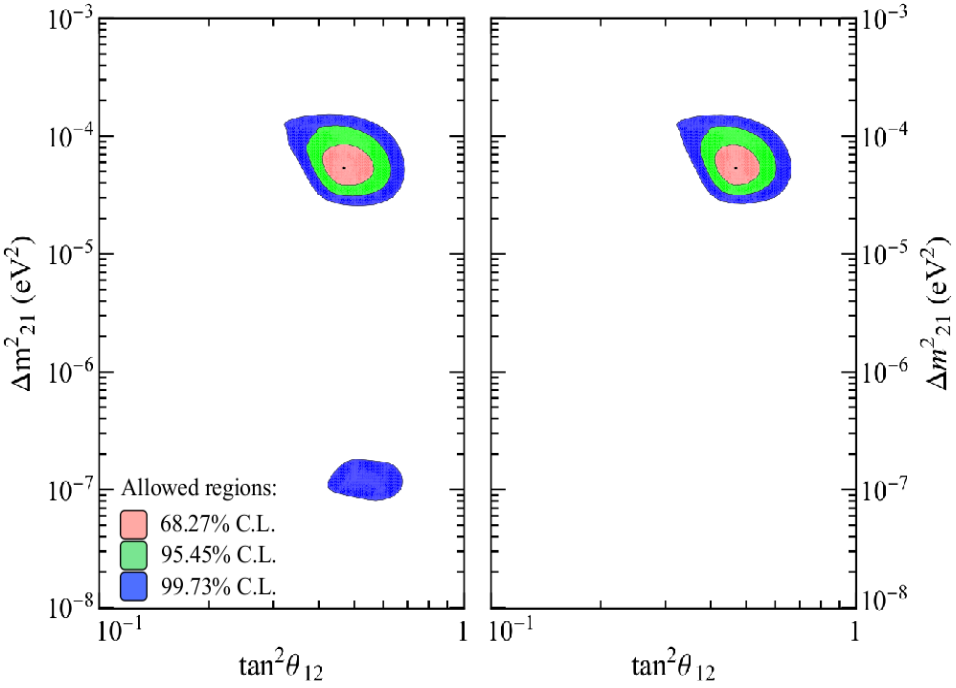

Figure 5.1: Allowed regions (d.o. f. = 3) of the space of parameters at 68.27% C.L. (pink), 95.45% C.L. (green) and 99.73% C.L. (blue) by the solar-without Borexino (left panel) and solar-with Borexino (right panel) data set.

IV [5], SNO [11] and the new results from Daya Bay experiment for the $\sin^2\theta_{13} = 0.023^{+0.014}_{-0.018}$ [21], we found our global fit best value:

$$\begin{cases} \tan^2\theta_{12} = & 0.48 \pm 0.02 \\ \Delta m^2_{12} = & (7.58 \pm 0.17) \times 10^{-5}\, eV^2. \end{cases} \tag{5.1}$$

The high precision reached today with which we can perform the measurement of the MSW oscillation parameters, could be used to investigate the new and non standard kind of interactions (NSI) for neutrinos with the normal matter and in general for the weak interactions.

A first parametrization of MSW theory was performed by [25, 26], by multiplying the Hamiltonian term of matter interaction by a factor A_{MSW}:

$$V(x) \to A_{MSW} \cdot V(x), \tag{5.2}$$

where

$$V(x) = \sqrt{2} G_F N_e(x), \tag{5.3}$$

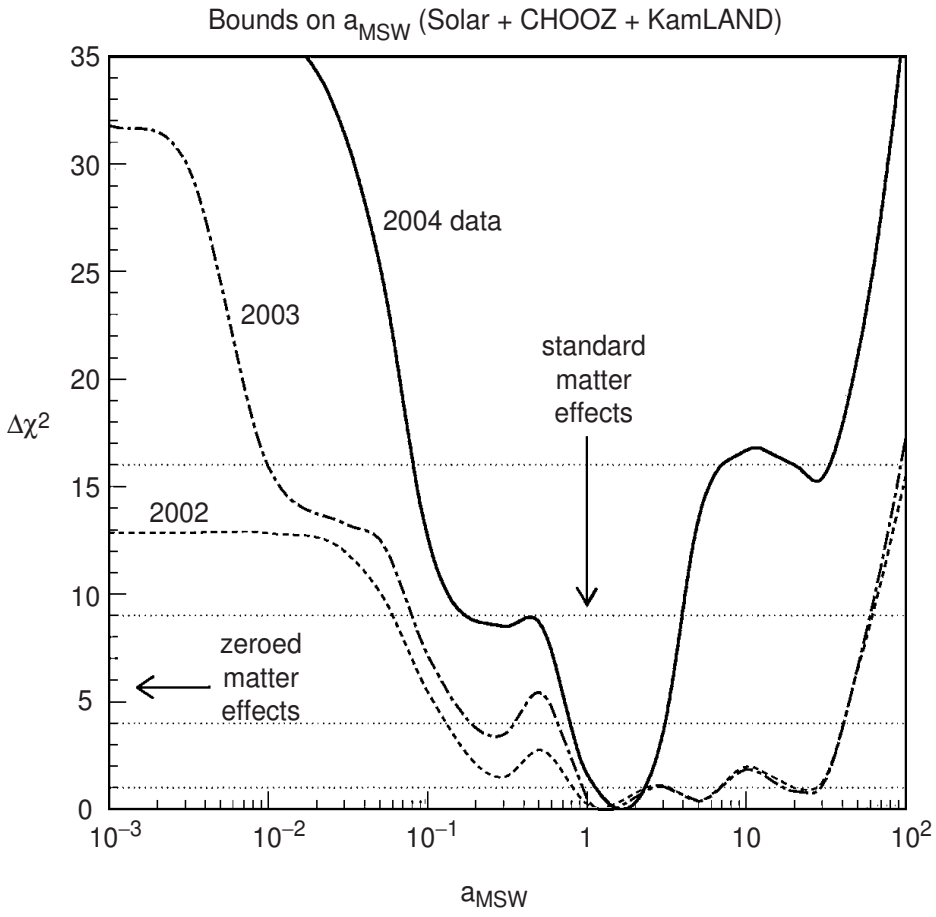

Figure 5.2: A_{MSW} bounds for the combination of all solar experiment, CHOOZ [45] and KamLAND [15] experiment data as available in the 2002, 2003 and 2004. The short dashed line indicates the 1,2,3 and 4σ. Especially after the new data of KamLAND in 2004, the no matter effect is rejected at $> 6\sigma$. On the contrary the matter effect is largely preferred with a minimum for $\Delta\chi^2$ around $A_{MSW} = 2$ at $\sim 2\sigma$.

$N_e(x)$ is the electron density in the solar interior and G_F the Fermi constant. With this parametrization for $A_{MSW} = 0$ the matter effects are not present. Instead, for $A_{MSW} = 1$ the we have the updated standard oscillations due to the matter effect. They have shown that the minimum of $\Delta\chi^2$, as a function of A_{MSW} parameter, prefers the solutions where $A_{MSW} \geq 1$ and ruled out at 5σ the vacuum solution with $A_{MSW} = 0$, as shown in Fig.5.2. This important result was achieved with the high statistic KamLAND results in the 2004 [15] We are therefore interested in using the global fit results to investigate the weak interaction properties as the Neutral (NC) and Charge Current (CC) coupling factors and how some NSI terms could modify the matter

potential in the MSW theory. To include all possible NSI terms, we can write the most generic four-fermion Lagrangian of interaction as:

$$\mathcal{L}^{NSI} = -2\sqrt{2}G_F\left(\nu_\alpha\gamma_\rho\nu_\beta\right)\Big(\, varepsilon^{f\tilde{f}_L}_{\alpha\beta}\,\bar{f}_L\gamma^\rho\tilde{f}_L + \varepsilon^{f\tilde{f}_R}_{\alpha\beta}\bar{f}_R\gamma^\rho\tilde{f}_R\Big) + h.c. \tag{5.4}$$

where G_F is the Fermi coupling constant, $\varepsilon^{f\tilde{f}_P}_{\alpha\beta}$ (with $f = e, u, d$ and $P = L, R$) denote the strength of the NSI (with respect to G_F) between the neutrinos ν with flavour α or β and the Left(Right)-lepton components of fermions f and $\tilde{f}$. The bounds on the $\varepsilon_{\alpha\beta}$ parameters come from accelerator based experiments as CHARM II, that already constrained the parameters $|\varepsilon_{\mu L/R}| < 0.03$ at (90% of C.L.) [27]. Other new bounds are found by means of atmospheric neutrino experiments as MINOS [36] and other ones TEXONO reactor neutrino experiment [37].

The NSI modify both propagation and detection neutrino processes. In particular the propagation or oscillation are sensitive only to $\varepsilon^{f\tilde{f}_P}_{\alpha\beta}$, where $f = \tilde{f}$. Therefore we can write $\varepsilon^{f\tilde{f}_P}_{\alpha\beta} \equiv \varepsilon^{f_P}_{\alpha\beta}$. In addition they are sensitive only to *vector components* of the interaction, then $\varepsilon^{f}_{\alpha\beta} \equiv \varepsilon^{f_L}_{\alpha\beta} + \varepsilon^{f_R}_{\alpha\beta}$.

We can write the term of Hamiltonian for the matter interaction as:

$$H_{mat} = \sqrt{2}G_F n_e \begin{pmatrix} 1+\varepsilon_{ee} & \varepsilon^*_{e\mu} & \varepsilon^*_{e\tau} \\ \varepsilon_{e\mu} & \varepsilon_{\mu\mu} & \varepsilon^*_{\mu\tau} \\ \varepsilon_{e\tau} & \varepsilon_{\mu\tau} & \varepsilon_{\tau\tau} \end{pmatrix} \tag{5.5}$$

where n_e is the number of electron density and the strength factors $\varepsilon_{\alpha\beta}$ are defined as:

$$\varepsilon_{\alpha\beta} = \sum_{f,P} \varepsilon^{f_P}_{\alpha\beta}\frac{n_{f_P}}{n_e} \qquad \text{where} \;\; f = e, u, d \;\text{and}\;\; P = L, R. \tag{5.6}$$

This relation shows also the dependence of the NSI from chemical composition of the medium in which the neutrino propagates. Using the combinations of the $\varepsilon_{\alpha\beta}$ elements, we can study how propagation and detection are affected by NSI by simulating the neutrino propagation in the solar structure and also in the Earth. The chemical composition provided by the solar models and the matter density distribution in the solar core are verified with much more precision by helioseismological data. Therefore we will use the electron, proton and neutron density distributions of the solar model as input data in our simulation of the solar structure.

5.1.1 Neutrino evolution and new parametrizations

To study the neutrino time evolution in a medium, we can start from its standard MSW Hamiltonian [38], that takes into account both vacuum term (only kinetic energy) and the interaction term with the matter, depending on its electron density:

$$i\frac{\mathrm{d}}{\mathrm{d}t}\begin{pmatrix}\nu_e\\ \nu_\mu\\ \nu_\tau\end{pmatrix} = \frac{1}{2E_\nu}\left[U\begin{pmatrix}0 & 0 & 0\\ 0 & \Delta m^2_{21} & 0\\ 0 & 0 & \Delta m^2_{31}\end{pmatrix}U^\dagger + a_{SI}\begin{pmatrix}1+\varepsilon_{ee} & \varepsilon_{e\mu} & \varepsilon_{e\tau}\\ \varepsilon^*_{e\mu} & \varepsilon_{\mu\mu} & \varepsilon_{\mu\tau}\\ \varepsilon^*_{e\tau} & \varepsilon^*_{\mu\tau} & \varepsilon_{\tau\tau}\end{pmatrix}\right]\begin{pmatrix}\nu_e\\ \nu_\mu\\ \nu_\tau\end{pmatrix}. \tag{5.7}$$

where $a_{SI} = \sqrt{2}G_F n_e$ and $\varepsilon_{\alpha\beta} = \sum_{f,P}\frac{n_f}{n_e}\varepsilon^{f_P}_{\alpha\beta}$, as shown in previous section in Eq.5.5. In the case of neutrino propagation, we are sensitive only to the vectorial terms $\varepsilon_{\alpha V} = \varepsilon_{\alpha L} + \varepsilon_{\alpha R}$. Therefore, in general, the off-diagonal component of NSI, related to the flavour change neutral current, undergoes a further suppression factors as compared to diagonal ones. As a conseguence, we take into account only the diagonal entries that are more difficult to constrain through the long-baseline experiments (see [38]). The U matrix are the correspondent Cabibbo-Kobayashi-Maskawa matrix for the leptons that rotates the mass eigenstates into flavour eigenstates for the neutrino fields.

Transforming into new basis $\tilde{\nu} = U^\dagger_{23}\nu$ and using the fact that for solar neutrino $G_F N_e \ll \Delta m^2_{atm}/E_\nu$, we can modify the standard Hamiltonian of matter interaction by adding a new term of NSI $a_{SI} + a_{NSI}$ as already shown in [28], where:

$$a_{NSI} = \sqrt{2}G_F\sum_{f=e,u,d} n_f\left(\varepsilon^f_{ee} - \cos^2\theta_{23}\varepsilon^f_{\mu\mu} - \sin^2\theta_{23}\varepsilon^f_{\tau\tau}\right) \equiv \sqrt{2}G_F\sum_f n_f\varepsilon^f_\odot \tag{5.8}$$

where $\varepsilon^f_\odot \equiv \varepsilon^f_{ee} - \cos^2\theta_{23}\varepsilon^f_{\mu\mu} - \sin^2\theta_{23}\varepsilon^f_{\tau\tau}$ is the fundamental parameter that we want to probe with the global fit of solar neutrino experiment results.

To probe the dependence of $\varepsilon_\odot$ on fermion species, we write the a_{NSI} explicating the proton-neutron number of density as it follows:

$$a_{NSI} = \sqrt{2}G_F[n_p(\varepsilon^e_\odot + \varepsilon^p_\odot) + n_n\varepsilon^n_\odot] \tag{5.9}$$

where we used the neutrality of the matter where $n_e = n_p$. We can make clearer the dependence of non standard interaction from the neutron-proton ratio as:

$$a_{NSI} = a_{SI}\left[\mathcal{E}_s + \left(\frac{n_n}{n_p} - 1\right)\mathcal{E}_{ns}\right] \tag{5.10}$$

where $\mathcal{E}_s = \varepsilon^e_\odot + \varepsilon^p_\odot + \varepsilon^n_\odot$ and $\mathcal{E}_{ns} = \varepsilon^n_\odot$. Here it is clear that $\mathcal{E}_s$, also called iso-singlet factor, depends on the standard interaction with normal matter and is dependent from chemical composition of the medium, on the contrary $\mathcal{E}_{ns}$ depends only on $\varepsilon^n_\odot$ and neutron density number and also on the features of neutral current interaction that takes place with them. We rewrite our new parametrization in a more suitable form, in order to compare our results with the previous works [25, 44] as follow:

$$A_{MSW} = 1 + \mathcal{E}_s + \left(\frac{n_n}{n_p} - 1\right)\mathcal{E}_{ns} \tag{5.11}$$

where A_{MSW} is the factor used to investigate the real magnitude of matter potential effects in the MSW theory for the flavour neutrino oscillation ($H_{mat} = A_{MSW} \cdot a_{SI}$). In this new factor we have an explicit dependence on the neutron-proton ratio that changes in the solar interior. The different solar neutrino fluxes are produced in different regions of solar core, where also the n/p ratios are different. Therefore, from solar neutrino spectrum analysis, we could discriminate between the iso-singlet parameter $\mathcal{E}_s$ and non-singlet $\mathcal{E}_{ns}$. In the standard theory, in which we do not take care of $\mathcal{E}_{ns}$ term, the iso-singlet term is equal to:

$$\mathcal{E}_s = A_{MSW} - 1 \tag{5.12}$$

If we consider that a generic matter as in the interior of the solar core where n/p ratio changes with the radius, $A_{MSW} - 1$ cannot be reduced as a function of $\mathcal{E}_s$ or $\mathcal{E}_{ns}$, therefore we have to handle their linear combination as a parameter.
In the next section we will show that the $A^\odot_{MSW}$ in the solar case can be expressed as :

$$A^\odot_{MSW} = 1 + \mathcal{E}_s - 0.57\mathcal{E}_{ns} \tag{5.13}$$

On the other hand, in the case of Earth's matter we have:

$$A^\oplus_{MSW} = 1 + \mathcal{E}_s - \delta_{ex}\mathcal{E}_{ns} \tag{5.14}$$

where $\delta_{ex} = (n_n/n_p - 1) \simeq 2\%$ is the neutrons over protons excess in the Earth.

5.1.2 Implementation of New Variable in MSW Theory

Starting from the standard MSW theory for three flavour neutrino oscillation, we are going to implement the NSI corrections to the equations of MSW formalism form both

Sun and Earth case. As for MSW theory, we considered the neutrino particles as ultra-relativistic because of their masses are negligible as compared to their kinetic energies. To evaluate the survival probability of the electron flavour in the Sun and Earth interiors, we consider only the transition $\nu_e \to \nu_\mu$ and $\nu_e \to \nu_\tau$, because the solar neutrino experiments are sensitive only to electron neutrino interaction and cannot distinguish between ν_μ and ν_τ. For this reason we take into account only Δm^2_{12}, θ_{12} and θ_{13} for the mixing matrix.

The survival probability for solar matter, in which the matter density decrease as exponential function of the radius, can be written as:

$$P_{ee} = \cos^4\theta_{13}\left(\frac{1}{2} + \frac{1}{2}\cos 2\theta_\odot \cos 2\theta_{12}\right) + \sin^4\theta_{13} \tag{5.15}$$

where $\theta_\odot$ is the mixing angle at neutrino production point, inside the solar core, in which the density is equal to ρ_{prod}. We have that this mixing angle is a function of $\Delta m^2_{12}/E_\nu$, the density of the production point ρ_{prod} and θ_{13}:

$$\cos 2\theta_\odot = \frac{\cos 2\theta_{12} - \xi_\odot}{[1 - 2\xi_\odot \cos 2\theta_{12} + \xi^2_\odot]^{1/2}} \tag{5.16}$$

where $\xi_\odot$ is defined as the ratio between the neutrino oscillation length in the vacuum l_ν and the one in the matter l_0:

$$l_\nu = \frac{4\pi E}{\Delta m^2}; \qquad l_0 = \frac{2\pi m_N}{\sqrt{2}A^\odot_{MSW} G_F \rho_{prod} Y_e \cos^2\theta_{13}}. \tag{5.17}$$

Therefore we have:

$$\xi_\odot = \frac{l_\nu}{l_0} = A^\odot_{MSW}\frac{2\sqrt{2}G_F\rho_{prod}Y_e\cos^2\theta_{13}}{m_N}\frac{E}{\Delta m^2} \tag{5.18}$$

that, at leading order can be expressed as:

$$\xi_\odot \simeq 0.203 \times A^\odot_{MSW} \cdot \cos^2\theta_{13}\left(\frac{E}{1\,\text{MeV}}\right)\left(\frac{\rho_{prod}Y_e}{100\,\text{g cm}^{-3}}\right) \tag{5.19}$$

where, for the solar case, $A^\odot_{MSW}$ is defined in Eq.5.13.

In general, in the Eqs.5.18, 5.19 we defined ρ_{prod} as matter density, Y_e as the number of electrons per nucleon and m_N as nucleon mass. In these calculations we did not take into account the real different distributions of density for protons and neutron nucleons

in the radius of the Sun that could provide different contributions to the mixing effects non considered in the standard approach.

In ours new calculations we considered the neutrino interactions with these different distributions for the nucleons, provided by the solar model as it will be discussed in the next section. On these purposes, we performed a modification of the number of density function and the NSI correction factor as:

$$\cos^2\theta_{13}A^{\odot}_{MSW} \equiv \cos^2\theta_{13}\left[n_e(r)\cdot\mathcal{E}_s + (n_n(r) - n_e(r))\cdot\mathcal{E}_{ns}\right] \tag{5.20}$$

where $n_e(r) = n_p(r)$ and $n_n(r)$ are the number of density of nucleons (protons and neutrons) as a function of solar radius provided by solar standard model considered.

By making explicit the $\xi_\odot$ in the survival probability P_{ee} and studying its variation with energy (fixing the MSW parameters), we observe a linear dependence on $\xi_\odot$ for low energy ranges of solar neutrino:

$$P_{ee} = \cos^4\theta_{13}\left[1 - \frac{1}{2}\sin^2 2\theta_{12}(1 + \xi_\odot\cos^2\theta_{12})\right] + \sin^4\theta_{13}. \tag{5.21}$$

Instead for higher energies the dependence on goes as $(1/\xi)^2$:

$$P_{ee} = \cos^4\theta_{13}\left[\sin^2\theta_{12} + \frac{1}{4}\sin^2 2\theta_{12}\cos^2\theta_{12}\left(\frac{1}{\xi_\odot}\right)^2\right] + \sin^4\theta_{13} \tag{5.22}$$

These relation show that at low energies we are much more sensitive to A_{MSW} corrections, being $\xi^2 \propto A_{MSW}$.

5.2 Simulations of neutrino propagation in the Sun and the Earth structures

In order to study the flavour neutrino states evolution, we simulate their propagation first in the solar interior, then we emulate their state evolution also in the Earth's interior taking into account its density stratifications (PREM) [48]. In this way we calculate the night/day asymmetry of the solar flux taking into account the solar exposure for each experimental site (Kamioka (Jap), Assergi (Ita) and Sudbury (Can)). We performed these simulation varying the values of $\mathcal{E}_s$, $\mathcal{E}_{ns}$ and marginalizing the

parameter $\tan^2\theta_{12}$, Δm^2_{12} and $\cos\theta_{13}$.

We generated 1000 random values with a flat distribution in the ranges $\mathcal{E}_s = [0.5, 2.5]$ and $\mathcal{E}_{ns} = [-3.0, 1.0]$ and for the values of $\cos^2\theta_{13}$ we used a Gaussian distribution around the best value measured by Daya Bay [21], expressed as $\sin^2\theta_{13} = 0.092 \pm 0.016$ with a standard deviation equal to its error, then we convert to $\cos^2\theta_{13}$. In this way we also marginalized the $\cos^2\theta_{13}$ parameter. We used these values to calculate the survival probability map, $P_{1e}(\tan^2\theta_{12}, \Delta m^2_{12})$, for the electron flavour outside the Sun core assuming as lighter mass eigenstate m_1, and the regeneration probability $P_{2e}(\tan^2\theta_{12}, \Delta m^2_{12})$ in the Earth, also in the case of KamLAND experiment, in order to evaluate the final survival probability:

$$P_{ee} = [P_{1e}(1 - P_{2e}) + P_{2e}(1 - P_{1e})]\cos^4\theta_{13} + \sin^4\theta_{13}. \tag{5.23}$$

Therefore we evaluate the χ^2 for the main experiments like SK-IV [29], SNO [35], Gallex/GNO-SAGE [41, 40, 39], Homestake [42], Borexino [90] and KamLAND anti-ν experiment [12].

The neutrino fluxes used in these simulation are produced with the high metallicity Solar Model [30] because of its best agreement with the depth of convective envelope and best agreement with the helioseismological data, related to the internal solar density.

5.2.1 Solar Model

From results of the solar models [34] used in this work, we obtain several information about the structure of the solar interior and, in particular, its chemical evolution in time and the final distribution of the nuclei of chemical elements. These information give us also the neutrino production distributions and also the neutron $n_n(r)$ and proton/electron $n_p(r) = n_e(r)$ distribution as a function of the radius $r = R/R_\odot$ (charge neutrality of the matter).

We can use these three distributions to simulate the neutrino propagation in the solar interior in order to calculate the survival probability of the flavour neutrino state. In order to calculate the survival probability we consider the so called normal mass hierarchy, in which the lighter mass eigenstate is $|\nu_1\rangle$ with eigenvalue m_1 ($m_1 < m_2 < m_3$).

Considering the electron neutrino flavour state as the lighter linear superposition of all three mass eigenstates, with respect to other neutrino flavours, hence the predominant mass eigenstate is $|\nu_1\rangle$. For this reasons we are interested in evaluating the probability P_{e1} that the neutrino comes out of the solar core, holding the $|\nu_1\rangle$ mass eigenstate as predominant. In the simulations we consider the Sun as a unidimensional structure where $r = R/R_\odot$ is the radius in terms of $R_\odot = 6.96 \times 10^8\, m$.

Starting from the center of the solar core ($r_0 \simeq 10^{-3}$) we divided the whole structure in a large number of short layers ($\delta r \sim 10^{-3} \times r$). For each ith-layer of the solar structure, we evaluate the survival probability $P_{e1}(r_i + \delta r)$ considering the density constant in its interior and following its evolution up to the solar surface ($r_n = 1$). Then we evaluate the survival probability P_{e1} for all fluxes of neutrinos produced in the given initial layer that we are considering. We repeated this calculation starting from successive layers of the solar structure, in order to calculate for each flux the effective probability P_{e1} taking into account the position of the region where it has been produced. Therefore we draw for each combination of $[\mathcal{E}_s, \mathcal{E}_{ns}$ and $\cos^2\theta_{13}]$ a P_{e1}-map of oscillation parameters $[\log_{10}(\tan^2\theta_{12}),\ \log_{10}(\Delta m^2_{12}/4E_\nu)]$ space[1]. We evaluate the survival probability only for the LMA region and for a neutrino energy range $200\ keV < E_\nu < 20\ MeV$. The ranges of parameters used for the probability evaluation are:

$$\begin{aligned} -1.0 < \log_{10}(\tan^2\theta_{12}) < 0.0; \\ -13.0 < \log_{10}\left(\frac{\Delta m^2_{12}}{4E_\nu}\right) < -9.0. \end{aligned} \tag{5.24}$$

In Fig.5.3 we show the survival probability P_{e1} that an initial electron neutrino, produced in the solar core by nuclear reactions, has outside the solar surface in the vacuum. Then we assumed in this case that in the electron flavour state the lighter eigenstate is dominant with respect to other ones (normal hierarchy). To evaluate probability P_{e1}, we assumed that the neutrino is produced in an initial point r_i inside the solar structure. We assume also that there are no interactions with the other neutrino coming from more internal regions and that it propagates forward up to the surface. At r_i

[1] We used for both parameters the log-scales only for the sake of simplicity

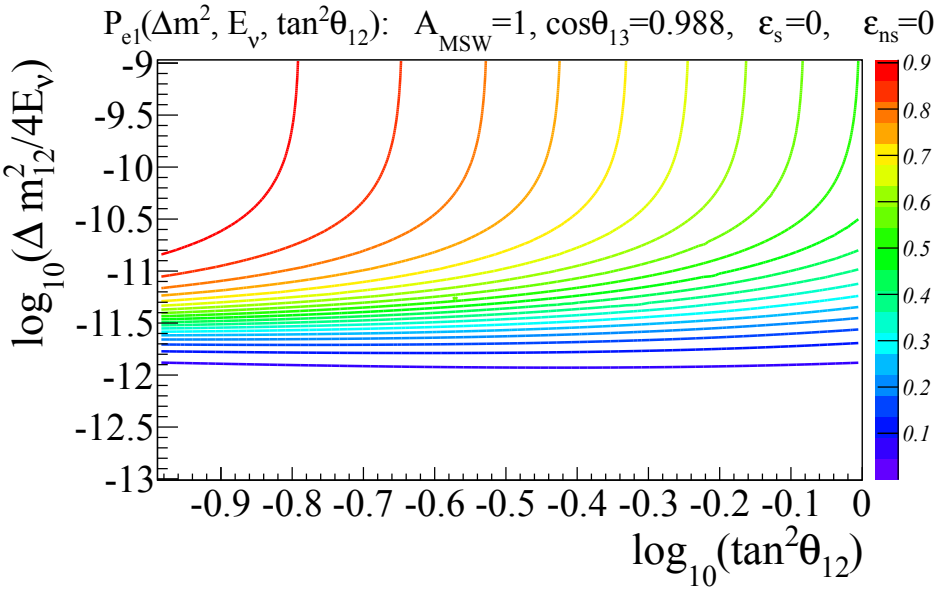

Figure 5.3: Survival probability that a electron neutrino produced inside the solar core. It goes out from the solar surface with lighter mass eigenstate m_1 (by assuming this hierarchy for neutrino mass). The probability depends on the $\Delta^2_{12}/(4E_\nu)$ ratio.

point we have a density $\rho_\odot(r_i)$ given by:

$$\rho_\odot(r_i) = \cos^4\theta^j_{13}\left[n_p(r_i)\mathcal{E}^j_s + (n_n(r_i) - n_p(r_i))\mathcal{E}^j_{ns}\right] \tag{5.25}$$

where j is the particular combination of parameter θ_{13}, $\mathcal{E}_s$ and $\mathcal{E}_{ns}$ used for the simulation. The quantity $n_p(r_i)$ and $n_n(r_i)$ are the density distribution for proton/electron and neutron particles provided by solar models.

Therefore we begin calculating the time evolution function for the flavour neutrino state in order to evaluate how the probability $P_{e1}(r_i)$ evolves after the crossing of successive layer $r_{i+1} = r_i + \delta r \cdots r_n = 1$.

We perform this calculation for each couple of parameter $\Delta m^2/4E_\nu, \tan^2\theta_{12}$ in the range considered. Therefore we have a P_{e1} distribution shown in Fig. 5.3 as a function of the MSW parameters and neutrino energy. The solutions for MSW equations, to describe the 3-flavour propagation and oscillations, are in general extremely complex [49]. In the case of solar neutrinos we can reduce the problem of 3 generation flavour propagation to the effective two-flavour problem following the formalism introduced by [46, 47]. We are interested in evaluating the transitional amplitude $T_{2\nu}(\nu_e \to \nu_1)$ for a neutrino that crosses in the ith-layer where the density is $\rho_\odot(r_i)$ (constant in this

layer). The flavour eigenstate of neutrino $|\nu_\alpha\rangle = U^* |\nu_i\rangle$ where:

$$U = \begin{pmatrix} \cos\theta_{12} & \sin\theta_{12} \\ -\sin\theta_{12} & \cos\theta_{12} \end{pmatrix} \tag{5.26}$$

is a Hermitian rotational matrix .

For practical case of neutrino propagation in a medium with a constant density, as in the case of single layer of the solar core, we can adopt directly the two-flavour formalism.

We start from space-evolution equation for the neutrino field:

$$\begin{aligned} i\frac{\mathrm{d}}{\mathrm{d}L}\begin{pmatrix} \nu_e \\ \nu_x \end{pmatrix} &= \frac{1}{2E}\left[U\begin{pmatrix} m_1^2 & 0 \\ 0 & m_2^2 \end{pmatrix}U^{-1} + \begin{pmatrix} A & 0 \\ 0 & 0 \end{pmatrix}\right]\begin{pmatrix} \nu_e \\ \nu_x \end{pmatrix} \\ &= \frac{1}{4E}\left[(\Sigma + A) + \begin{pmatrix} -\Delta m_{12}^2 c_{12} + A & \Delta m_{12}^2 s_{12} \\ \Delta m_{12}^2 s_{12} & \Delta m_{12}^2 c_{12} - A \end{pmatrix}\right]\begin{pmatrix} \nu_e \\ \nu_x \end{pmatrix} \end{aligned} \tag{5.27}$$

where $c_{12} = \cos\theta_{12}$, $s_{12} = \sin\theta_{12}$ and

$$\Sigma = m_1^2 + m_2^2; \qquad \Delta m_{12}^2 = m_2^2 - m_1^2 \qquad \Delta m_{13}^2 = m_3^2 - m_1^2. \tag{5.28}$$

The effect of matter interaction is contained in A, defined as:

$$A = 2\sqrt{2}G_F N_e(r_i)E = 2\sqrt{2}G_F(Y_e/m_N)\rho_\odot(r_i)E. \tag{5.29}$$

For the sake of simplicity, we are going to reduce the notation in the same way as done in the program code. We define:

$$i\frac{\mathrm{d}}{\mathrm{dL}}\begin{pmatrix} \nu_e \\ \nu_x \end{pmatrix} = \left[\frac{1}{4E}(\Sigma + A) + \begin{pmatrix} -a_1 & b_1 \\ b_1 & a_1 \end{pmatrix}\right]\begin{pmatrix} \nu_e \\ \nu_x \end{pmatrix} \tag{5.30}$$

where

$$\begin{cases} a_1 = \dfrac{\Delta m_{12}^2}{4E_\nu}\cos 2\theta - \dfrac{\sqrt{2}}{2}G_F(Y_e/m_N)\rho_\odot(r_i), \\ \\ b_1 = \dfrac{\Delta m_{12}^2}{4E}\sin 2\theta, \end{cases} \tag{5.31}$$

Solving the eigenvalue equations we obtain the following set of functions as solution for time evolution flavour state:

$$\begin{cases} y_1(r_i) = \cos\left(\sqrt{a_1^2+b_1^2}\cdot r_i\right) - i\dfrac{a_1}{\sqrt{a_1^2+b_1^2}}\sin\left(\sqrt{a_1^2+b_1^2}\cdot r_i\right) \\ \\ y_2(r_i) = -i\dfrac{b_1}{\sqrt{a_1^2+b_1^2}}\sin\left(\sqrt{a_1^2+b_1^2}\cdot r_i\right) \end{cases} \tag{5.32}$$

therefore we can define the eigenvector matrix for each point r_i as:

$$Z^m(r_i) = \begin{pmatrix} y_1(r_i) & y_2(r_i) \\ y_2(r_i) & y_1^*(r_i) \end{pmatrix} \tag{5.33}$$

the final matrix is given by the recursive multiplication of these matrices

$$Z^m = \prod_{k=i}^{n} Z^m(r_k) \tag{5.34}$$

where $i = 0...n$ runs from the center of the solar core to the surface and correspond to the point r_i where the neutrino has been generated. Therefore r_i is the point where we start in evaluating the space evolution of neutrino flavour state in the solar interior. We change in the mass basis:

$$Z^f = U^* \cdot Z^m = \begin{pmatrix} Z^m_{11}c_{12} - Z^m_{21}s_{12} & Z^m_{12}c_{12} - Z^m_{22}s_{12} \\ Z^m_{11}s_{12} + Z^m_{21}c_{12} & Z^m_{12}s_{12} + Z^m_{22}c_{12} \end{pmatrix} \tag{5.35}$$

The probability P_{e1} is given by:

$$P_{e1} = |Z^e_{11}|^2 = |Z^m_{11}\cos\theta_{12} - Z^m_{21}\sin\theta_{12}|^2 = |T_{2\nu}(\nu_e \to \nu_e)|^2 \tag{5.36}$$

This corresponds to the probability that an initial electron neutrino, produced inside the solar core, comes out of the solar surface in the $|\nu_1\rangle$ eigenstate. This neutrino propagates in the solar-earth vacuum space without any interaction as far as it comes in contact with earth. By means of this probability we can evaluate the local flux intensity produced by nuclear reactions starting from the point r_i:

$$\frac{\mathrm{d}\phi_\nu(\mathrm{r_i})}{\mathrm{dr}} = P_{e1}\cdot\frac{\mathrm{dN}_\nu(\mathrm{r_i})}{\mathrm{dr}} \tag{5.37}$$

where $dN_\nu(r_i)/dr$ is the production rate of neutrino evaluated in solar model for each species of neutrino (pp, pep, hep, $Be7$, $B8$, $N13$, $O15$, $F17$). Therefore the total flux is given by the integral over the solar radius:

$$\phi_\nu = \int_0^{R_\odot=1} \frac{\mathrm{d}\phi_\nu(\mathrm{r_i})}{\mathrm{dr}}\, dr. \tag{5.38}$$

These are normalized fluxes because at this point we are interested only to the probability of the oscillation as show in Fig.5.3 for the ^{7}Be.

5.2.2 Earth Model

The neutrinos coming from the Sun have a weak interaction with earth matter, but it exists the probability that some of flavour oscillated neutrinos changes their states coming back in a electron flavour state.
This effect, also called *"regeneration"*, takes place when the neutrinos pass through the Earth matter before to be detected from the experiments. The regeneration effect gives the Night/Day (N/D) asymmetry observed in the ^{8}B neutrino flux at higher energies. This effect depends on the angle exposure of experiment with respect to the zenith and on the density of different internal shells of the earth crossed by neutrinos during their propagation. The reference for the matter density distribution in the internal earth structure is [48], where, by means of the measurements of the earthquake-wave velocity, it is reconstructed the internal shell structure of the earth and it is measured the density of them. In Fig.5.5 we show the density ρ as a function of the depth, along with the velocity of the wave components (V_P and V_S) inside the core and the mantle.

To take into account the N/D effect, we cannot consider the Earth as a unidimensional body, as done for the Sun, but we have to consider its rotation around its axis. Starting from the time-exposure of each experiment, situated at opposite longitudes (Canada, Italy and Japan), we divide overnight rotation in 6 main angle where we trace the path across the Earth shells are intercepted by the solar neutrino before their detection. Obviously, during the daily exposure, the regeneration effect is absent, therefore we consider the solar fluxes without perturbations. To evaluate the regeneration effect,

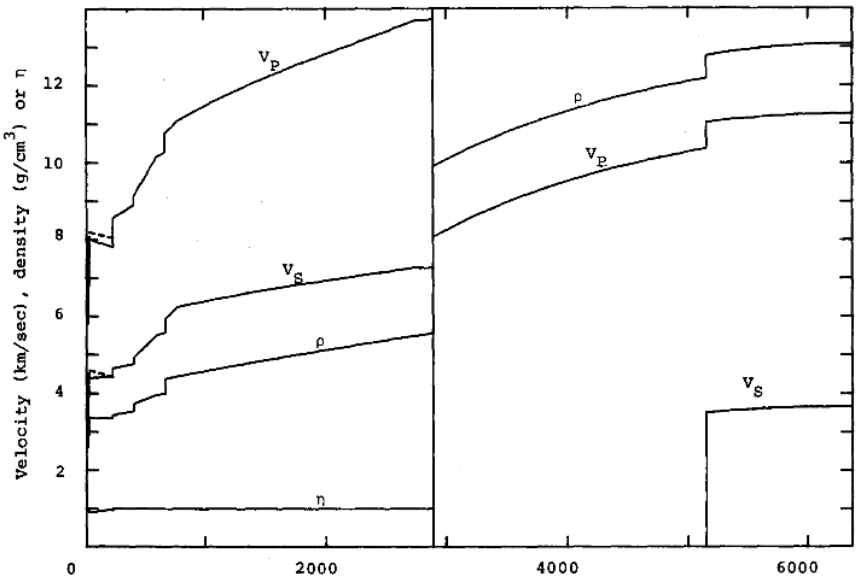

Figure 5.4: The PREM or *Preliminary Reference Earth Model* show the inner structure of the Earth starting from the superficial crust with a average density close to the water $\rho_{\oplus}(r = n) \sim 1.02 g/cm^3$ to core density at 6371.0 km of depth where the density is $\rho_{\oplus}(r = 0) \sim 13.0 g/cm^3$.

we consider the formalism discussed in [50, 51].

The night survival probability for the electron neutrino flavour is:

$$P_{ee}^N = P_{ee}^D - \cos 2\theta_{\odot} \cos^2 \theta_{13} \langle f_{reg} \rangle_{zenith} \tag{5.39}$$

where P_{ee}^D is the probability in the solar case Eq.5.15, f_{reg} is the regeneration effect given in general by:

$$f_{reg} = P_{2e} - \sin^2 \theta_{12} \cos^2 \theta_{13} \tag{5.40}$$

where P_{e2} is the transition probability of second mass eigenstate to ν_e that we have to calculate for the solar neutrinos.

As shown in Fig.5.5 shows, the internal Earth structure is composed by several shells with very different sizes and densities ranging from $\rho_{surf} \simeq 1.02\, g \cdot cm^{-3}$ on surface to the higher densities present in the mantle and core $\rho_{core} \simeq 13.0 g \cdot cm^{-3}$. For comparison, the solar core has a density about 10 times bigger: $\rho_{\odot} \simeq 150.0\, g \cdot cm^{-3}$.

The time exposure provided by experiments gives us the direction of the Sun with respect to the zenith of experiment site. By means of this information we can evaluate

the path of neutrinos through the shells of the Earth. The length of this path is given, roughly by $\delta l = \sqrt{R_{k+1}^2 - R_k^2}$, where R_k is the radius of the shell. Starting from entrance point in Earth crust, as in the solar case, we follow the mass eigenstate evolution up to the detector, changing each time the neutrino pass in a new shell the density of the medium. The density evaluated for the earth is given by:

$$\rho_{Sh}(r_i) = \rho_{\oplus}(r_i)(n_p\mathcal{E}_s + (n_n - n_p)\mathcal{E}_{ns}) \tag{5.41}$$

in which $\rho_{\oplus}(r_i)$ are the polynomials describing the density curve in each shell as a function of the radius. The number of densities for neutron and proton in the Earth are fixed to the crust values: $n_n = 0.506$ and $n_p = 0.494$.
The probability P_{2e} for the electron neutrino regeneration is evaluated in the same way for the solar case, but instead of the first entries of the propagation matrix, we take into account the following term:

$$P_{2e} = |Z_{12}^e|^2 = |Z_{11}^m s_{12} + Z_{12}^m c_{12}|^2 \tag{5.42}$$

In the case of reactor sources, in which we can assume the crust densities constant in a large part of the neutrino path, we can approximate f_{reg} as:

$$f_{reg} = \xi_{\oplus}\cos^2\theta_{13}\sin^2 2\theta_{\oplus}\sin^2\left[A_{MSW}a_{\oplus}\cos^2\theta_{13}(1 - 2\xi_{\oplus}^{-1}\cos^2\theta_{12} + \xi_{\oplus}^{-2})^{-\frac{1}{2}}\left(\frac{L}{2}\right)\right] \tag{5.43}$$

where $\xi_{\oplus}$ is defined as the Eq.5.18 but with earth densities as defined in Eq.5.25 in which n_n, n_p and n_e are the terrestrial values. The parameter $a_{\oplus}$ is defined as

$$a_{\oplus} \equiv \sqrt{2}G_F N_e^{\oplus} = \frac{\sqrt{2}G_F Y_e^{\oplus}\rho_{\oplus}}{m_N} \tag{5.44}$$

where $\rho_{\oplus}$ is defined as $\rho_{\odot}$ in Eq.5.25 Finally L is the length of path crossed by neutrinos in the Earth.

5.2.3 Neutrino Experiments

After the calculation for the survival probability in the Sun of lighter mass eigenstate P_{e1} and the different regeneration probability as a function of the zenith angle in each

experiment, we can evaluate the total survival probability for the electron neutrino flavour and the relative rate or electron spectrum for each experiment considered. The survival probability is expressed as a function of θ_{12}^2 angle and as the $\Delta m^2/(4E_\nu)$ ratio. Therefore to evaluate the total rate for a given pair of MSW parameters, we interpolate the survival probability map for different neutrino energies E_ν.

The solar neutrino fluxes used to evaluate the experimental rate and then the χ^2 map are provided by [34]. In Tab.5.1 we show the neutrino fluxes predicted by the solar models, in which we considered the results of the first column for the Grevesse and Sauval chemical composition [83]. To evaluate the χ^2 map, we marginalized all main

Flux	GS98	AGS05	AGSS09	AGSS09ph
pp	5.97	6.04	6.03	6.01
pep	1.41	1.44	1.44	1.43
hep	7.91	8.24	8.18	8.10
^{7}Be	5.08	4.54	4.64	4.79
^{8}B	5.88	4.66	4.85	5.22
^{13}N	2.82	1.85	2.07	2.15
^{15}O	2.09	1.29	1.47	1.55
^{17}F	5.65	3.14	3.48	3.70

Table 5.1: Predicted neutrino fluxes.
Neutrino fluxes are given in units of 10^{10}(pp), 10^{9}(^{7}Be), 10^{8}(pep, ^{13}N, ^{15}O), 10^{6}(^{8}B, ^{17}F) and 10^{3}(hep) cm^{-2} s^{-1}.

parameters with exception for the new one introduced in this work:

$$\chi^2_{global}(\mathcal{E}_s, \mathcal{E}_{ns}) = Marg\left[\chi^2_\odot(\Delta m^2_{12}, \theta_{12}, \theta_{13}, \mathcal{E}_s, \mathcal{E}_{ns}, f_{B8}, f_{Be7}, f_{pp}, f_{CNO}) + \right. \\ \left. + \chi^2_{KamLAND}(\Delta m^2_{12}, \theta_{12}, \theta_{13})\right] \tag{5.45}$$

where the *Marg* operator is introduced in [52]. The $\chi^2_\odot = \sum_{i=1}^{n} \chi^2_i$ is the sum of χ^2_i evaluated for each single solar neutrino experiment as (i = {Borexino, SK, SNO, Gallex/SAGE/GNO, Homestake}) and f_α, with $\alpha = B8, Be7...$, are the neutrino fluxes predicted by the solar model.

Below it is listed a summary of the experimental results necessary to determine the χ^2 map with their corresponding features related to our calculations.

Homestake

This was the first experiment able to observe the neutrino interactions with the matter [57]. Base on inversed beta-decay proposed by Pontecorvo and Alvarez [77, 78] of chlorine:

$$\nu_e + {}^{37}\text{Cl} \rightarrow {}^{37}\text{Ar} + e^- \tag{5.46}$$

with threshold energy of $E_{nu}^{thr} = 0.814$ MeV. The main fluxes observed are the Be7 neutrino and the CNO neutrinos. The experiment result consist only of the number of Argon nuclei measured after fixed time of exposure, hence only a energy integrated value of the neutrino fluxes, without distinguish the neutrino type and its relative energy.

The total counting rate observed is:

$$R_{^{37}Cl} = 2.56 \pm 0.23 SNU \tag{5.47}$$

where $SNU = 10^{-36}$ events$\times$atoms$^{-1}\times$s^{-1} is the *Solar Neutrino Units*. This results was also the first evidence of *Solar Neutrino Anomaly* (SNA), the expected rate from solar model, without MSW flavour suppression, is $R^0_{^{37}Cl} = 8SNU$ more than 3 times the measured value. In order to evaluate this rate we used the energy distribution of neutrinos $d\phi_\alpha/dE_\nu$ (normalized to 1) multiplied by the total fluxes f_α, provided both by solar models, therefore we multiply this result for the flavor survival probability $P_{ee}(E_\nu)$ in Eq. 5.23 then for the cross section of Homestake experiment calculated by J.Bahcall [56] $\mathrm{d}\sigma_{^{37}Cl}/\mathrm{d}E_\nu$. The final rate is:

$$R_{^{37}Cl} = \int_{E_{thr}}^{E_{max}} \frac{\mathrm{d}\phi_\alpha}{\mathrm{d}E'} \cdot f_\alpha \cdot P_{ee}(E') \cdot \frac{\mathrm{d}\sigma_{^{37}\mathrm{Cl}}}{\mathrm{d}E'} \mathrm{d}E' \tag{5.48}$$

Gallex/GNO and SAGE

The Gallex/GNO [65, 66, 67, 68, 69, 70] and SAGE [71, 72, 73, 74, 75, 76] radiochemical experiment was able to measure for the first time the ν_{pp} neutrino that is most

intense neutrino flux emitted from the sun $f_{pp} \simeq 6 \times 10^{10} cm^{-2}\, s^{-1}$. They are very similar experiment located in the Laboratori Nazionali del Gran Sasso (LNGS-INFN) in Italy and in Baksan Neutrino Laboratory (BNO) at the north of Caucasian mountains respectively. They observe the neutrino events by means of reaction:

$$\nu_e + {}^{71}Ga \rightarrow {}^{71}Ge + e^- \tag{5.49}$$

with a very low threshold $E_{thr} = 0.240$ MeV. Also in this case the results of both experiments are the integral on total energy range of contributions of all neutrino fluxes, without distinguish among the components. The total rate measured is a average between the Gallex/GNO and SAGE counting rate, obtained by detecting the number of Germanium nuclei present in the liquid detector (Gallium):

$$R_{^{71}Ga}^{Gallex/GNO+SAGE} = 68.1 \pm 3.75\, SNU. \tag{5.50}$$

SuperKamiokaNDE

The SuperKamiokaNDE is the bigger neutrino experiment based on Čerenkov effect of scattered electrons by solar neutrino, filled with 5×10^4 tons of water within the Kamioka mine in Japan and with more than 10^4 photo-multipliers on internal surface. Together to KamiokaNDE it was the first neutrino detector able to observe the neutrino events in real time with a threshold energy of $E_{thr}5$ MeV in the phase I and then with a new threshold in the phase II and III at $E_{thr} = 4.5$ MeV. This experiment is able also to observe the direction of neutrinos showing the dependence of the flux with the position of the Sun [2, 3, 5]. In this case we reconstruct the energy spectrum calculating the cross section [58] with radiative corrections. The total rate is calculated as integral of Čerenkov spectrum given by:

$$\frac{\mathrm{d}\Phi_e^{\nu_e}}{\mathrm{d}T_e} = \int_{E_{\nu_e}} \frac{\mathrm{d}\sigma_{ES}^{\nu_e}}{\mathrm{d}T_e \mathrm{d}E'_{\nu_e}} \cdot \frac{\mathrm{d}\phi_{\nu_e}^{MSW}}{\mathrm{d}E_{\nu_e}} \mathrm{d}E_{\nu_e} \tag{5.51}$$

and the other neutrino flavours:

$$\frac{\mathrm{d}\Phi_e^{\nu_x}}{\mathrm{d}T_e} = \int_{E_{\nu_x}} \frac{\mathrm{d}\sigma_{ES}^{\nu_x}}{\mathrm{d}T_e \mathrm{d}E'_{\nu_x}} \cdot \frac{\mathrm{d}\phi_{\nu_x}^{MSW}}{\mathrm{d}E_{\nu_x}} \mathrm{d}E_{\nu_x} \tag{5.52}$$

where $\sigma_{ES}^{\nu_a}$ are the cross section for electron neutrino and the other $\mu - \tau$ flavours. The flux $\phi_{\nu_a}^{MSW}$ are solar fluxes reduced by survival probability. From these spectra we

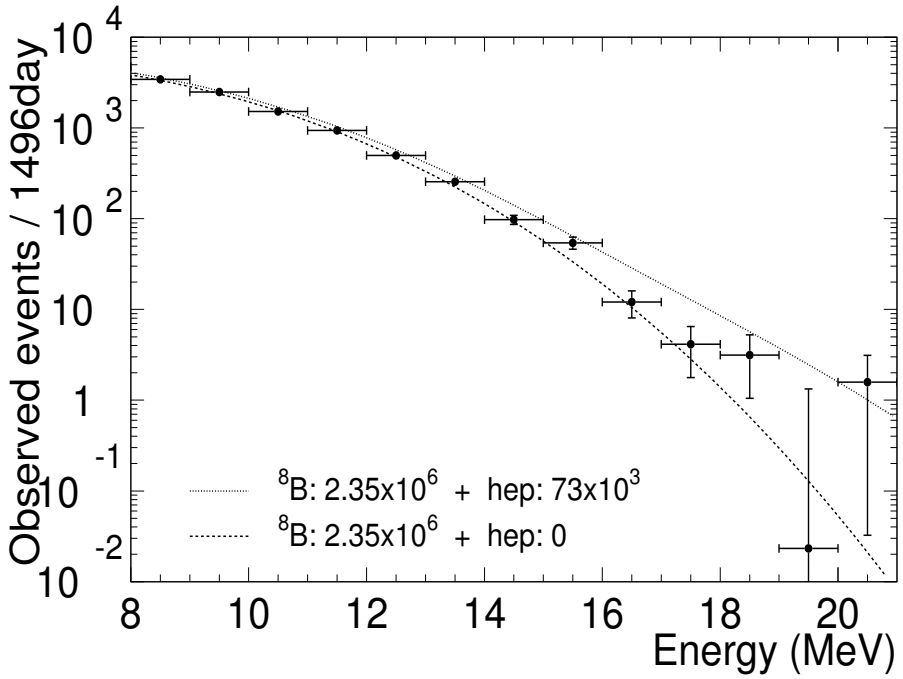

Figure 5.5: Čerenkov spectrum of electron scattering in the SuperKamiokaNDE experiment generated by $^8B + hep$ neutrino fluxes.

perform a Gaussian convolution to obtain the effective spectrum observed within each *bin*, centred on bin energy $\widetilde{T}_e^i$, as follow:

$$\frac{d\widetilde{\Phi}_e^i}{d\widetilde{T}_e^i} = \int_{T_e} \frac{1}{\sqrt{2\pi}\sigma(T_e)} \exp\left(-\frac{(\widetilde{T}_e^i - T_e)^2}{2\sigma^2(T_e)}\right) \frac{d\phi_e}{dT_e} dT_e \tag{5.53}$$

where in this case $\sigma(T_e)$ is the resolution of experiment, defined as:

$$\sigma_{SK}(T_e) = -0.25 + 0.20\sqrt{T_e} + 0.06\,T_e. \tag{5.54}$$

and the integral is done on total energy range. Hence we can integrate this last spectrum on the bin energy range. The total rate observed in this way is expressed in term of neutrino flux as:

$$\Phi_{^8B}^{SK} = (2.35 \pm 0.08) \times 10^6\, cm^{-2}\, s^{-1}. \tag{5.55}$$

Also in this case it is visible a strong reduction of the flux as compared to the expected from solar models.

SNO

The SNO/SNO+ experiment (*Sudbury Neutrino Observatory*) is a water Čerenkov experiment using heavy water (D_2O) situated in the Creighton mine (INCO Ltd.) near to Sudbury, Ontario Canada [4].

This experiment is able to observe with a similar statistic all three interaction that could be done by a neutrino (Neutral Current (NC), Charge Current (CC) and Elastic Scattering (ES)) then it is the only one able to observe directly the total neutrino flux independently from the MSW oscillations. The possible reaction are the following:

$$\begin{aligned} CC: &\quad \nu_e + d \to p + p + e^- \qquad E_{th}^{CC} = 1.44\ MeV \\ NC: &\quad \nu_\alpha + d \to p + n + \nu_\alpha \qquad E_{th}^{NC} = 2.22\ MeV \\ ES: &\quad \nu_\alpha + e^- \to \nu_\alpha + e^- \qquad E_{th}^{ES} = 5.5\ MeV \end{aligned} \tag{5.56}$$

where $\alpha = e, \mu, \tau$. Unfortunately for the CC the threshold has been fixed to 5.5 MeV because of the high background.

In this case, instead of evaluating directly the spectra for each kind of interaction, the collaboration defined a polynomial for the $P_{ee}(E_\nu)$ and for the D/N asymmetry $A_{ee}(E_\nu)$, as a neutrino energy function:

$$P_{ee}^{\mathrm{d}} = c_0 + c_1(E_\nu[MeV] - 10) + c_2(E_\nu(MeV) - 10)^2 \tag{5.57}$$

and the Day-Night asymmetry:

$$A_{ee}(E_\nu) = a_0 + a_1(E_\nu - 10) \tag{5.58}$$

Therefore we evaluated the survival probability and D/N asymmetry as energy functions, with f_{B8} fixed, and fitted the new curves with these polynomial. Hence we evaluated the χ^2 for the SNO results:

$$\chi_j^2(\Delta m^2, \tan^2\theta_{12}) = (R^{Exp} - R_j^{Teo})^T \sigma_{SNO}^{-1} (R^{Exp} - R_j^{Teo}) \tag{5.59}$$

using the best fit shown in Tab.5.2 for R^{Exp} and the inverse of the matrix correlation σ_{SNO} shown in Tab.5.3. Here the subscript j indicates a given combination of $\{\mathcal{E}_s^j$, $\mathcal{E}_{ns}^j$ and $\cos\theta_{13}^j\}$ In Fig.5.6 we show and example $P_{ee}(E_\nu)$ and $A_{ee}(E_\nu)$ function with relative spread due to parameters uncertainties and correlations.

	Best fit	Stat.	Systematic uncertainty			
			Basic	D/N	MC	Total
Φ_{B8}	5.25	± 0.16	$^{+0.11}_{-0.12}$	± 0.01	$^{+0.01}_{-0.03}$	$^{+0.11}_{-0.13}$
c_0	0.317	± 0.016	$^{+0.008}_{-0.010}$	± 0.002	$^{+0.002}_{-0.001}$	± 0.009
c_1	0.0039	$^{+0.0065}_{-0.0067}$	$^{+0.0047}_{-0.0038}$	$^{+0.0012}_{-0.0018}$	$^{+0.0004}_{-0.0008}$	± 0.0045
c_2	-0.0010	± 0.0029	$^{+0.0013}_{-0.0016}$	$^{+0.0002}_{-0.0003}$	$^{+0.0004}_{-0.0002}$	$^{+0.0014}_{-0.0016}$
a_0	0.046	± 0.031	$^{+0.007}_{-0.005}$	± 0.012	$^{+0.002}_{-0.003}$	$^{+0.014}_{-0.013}$
a_1	-0.016	± 0.025	$^{+0.003}_{-0.006}$	± 0.009	± 0.002	$^{+0.010}_{-0.011}$

Table 5.2: Results from the maximum likelihood fit in [11]. Note that Φ_{B8} is in units of $\times 10^6\ cm^{-2}\ s^{-1}$. The D/N systematic uncertainties includes the effect of all nuisance parameters that were applied differently between day and night. We performed the fit of P_{ee} and A_{ee} for each combination of $\mathcal{E}_s$, $\mathcal{E}_{ns}$ and $\cos\theta_{13}$ using the best fit to evaluate the χ^2 for SNO experiment.

	Φ_{B8}	c_0	c_1	c_2	a_0	a_1
Φ_{B8}	1.000	-0.723	0.302	-0.168	0.028	-0.012
c_0	-0.723	1.000	-0.299	-0.366	-0.376	0.129
c_1	0.302	-0.299	1.000	-0.206	0.219	-0.677
c_2	-0.168	-0.366	-0.206	1.000	0.008	-0.035
a_0	0.028	-0.376	0.219	0.008	1.000	-0.297
a_1	-0.012	0.129	-0.677	-0.035	-0.297	1.000

Table 5.3: Correlation matrix from the maximum likelihood fit.

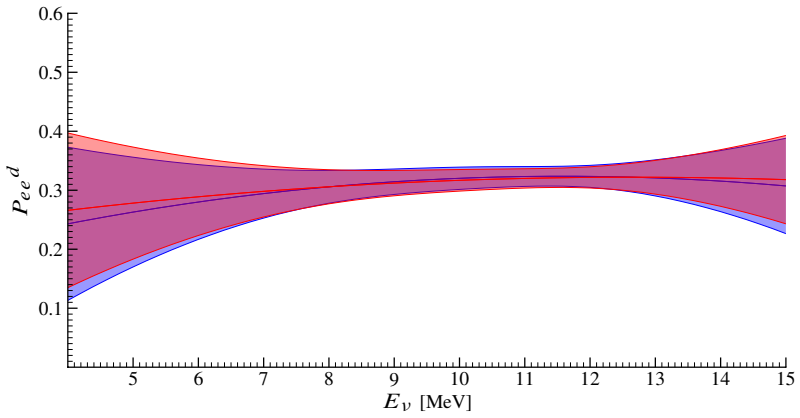

(a) $P_{ee}(E_\nu)$

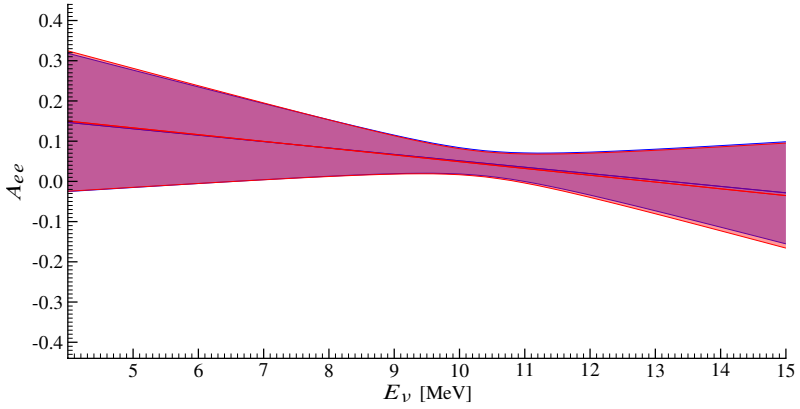

(b) $A_{ee}(E_\nu)$

Figure 5.6: Čerenkov spectrum of electron scattering in the SuperKamiokaNDE experiment generated by ${}^8B + hep$ neutrino fluxes.

Borexino

The Borexino experiment features are extensively discussed in the previous chapters. Here we take into account the last best fit for the count rates of neutrino ν_{Be7}, that is $\phi_e^{Be7} = 46.0 \pm 1.5$ [91] and then we calculate the χ^2 as:

$$\chi^2 = \frac{(R_{sim}(\theta_{12}, \Delta m^2_{12}) - R_{exp})^2}{\sigma^2} \tag{5.60}$$

where $\mathrm{R}_{sim}(\theta_{12}, \Delta m^2_{12})$ is the count rates for the beryllium shoulder in the Borexino spectrum obtained from the simulation for a fixed set of values $(\cos^2\theta_{13}, \mathcal{E}_S, \mathcal{E}_{NS})$ varying the value of Δm^2 and $\tan^2\theta_{12}$.

KamLAND

The KamLAND experiment is located in the same place of the old KamiokaNDE experiment, in the Kamioka mine in Japan. Its position is close to 16 nuclear reactors that contribute for a relevant anti-neutrino flux. It consists of 1 kiloton of liquid scintillator that detect reactor anti-neutrinos through the reaction:

$$p + \overline{\nu}_e \rightarrow n + e^+ \tag{5.61}$$

The positron is then detected when it scintillates and when it annihilates with an electron. This annihilation, in delayed coincidence with the γ-ray from neutron capture, represents an easily distinguishible signal. The anti-neutrino energy spectrum was measured at distance from the nuclear power plants where the oscillating effect was negligible by [60, 61]. The phenomenological parametrization of this spectrum is found to be depending on which kind of isotope is involved [62]:

$$\frac{dN_\nu}{dE_\nu} = e^{a_0 + a_1 E_\nu + a_2 E_\nu} \tag{5.62}$$

where the parameters a_i are reported in Tab.5.4 and the spectrum is expressed in $\nu_e/Mev - fission$. Therefore we have define how many fissions for each isotope there are. For a given nuclear reactor plant this quantity will depend on three factors:

1. The thermal power of that reactor;
2. The isotopic composition of the reactor fuel;
3. The amount of thermal power emitted during the fissioning of a nucleus of a given isotope.

In Tab. 5.5 we report the main characteristics of the nuclear plants considered by the collaboration and we take into account also the time variation of the isotopes in the nuclear fuel and then the power variances showed in [59]. In order to evaluate the effective spectrum observed by KamLAND we start from the initial spectrum for each reactor and its time variation and we apply the MSW flavour oscillation as for the solar case in which in the three flavour case we have that the survival probability is:

$$P_{ee}^{3\nu} = \cos^4\theta_{13}\tilde{P}_{ee}^{2\nu} + \sin^4\theta_{13} \tag{5.63}$$

Isotope	^{235}U	^{239}Pu	^{238}U	^{241}Pu
a_0	0.870	0.896	0.976	0.793
a_1	-0.160	-0.239	-0.162	-0.080
a_2	-0.0910	-0.0981	-0.0790	-0.1085

Table 5.4: Parameters for $\frac{dN_\nu}{dE_\nu}$ parameterization. The resulting spectrum is given in units of $\overline{\nu}_e$/MeV-fission.

Reactor Site	Distance (km)	Max. Thermal Power (GW)
Kashiwazaki	160	24.6
Ohi	180	13.7
Takahama	191	10.2
Hamaoka	213	10.6
Tsuruga	139	4.5
Shiga	81	1.6
Mihama	145	4.9
Fukushima-1	344	14.2
Fukushima-2	344	13.2
Tokai-II	295	3.3
Shimane	414	3.8
Ikata	561	6.0
Genkai	755	6.7
Onagawa	430	4.1
Tomari	784	3.3
Sendai	824	5.3

Table 5.5: Reactor parameters. Reproduced from reference [63].

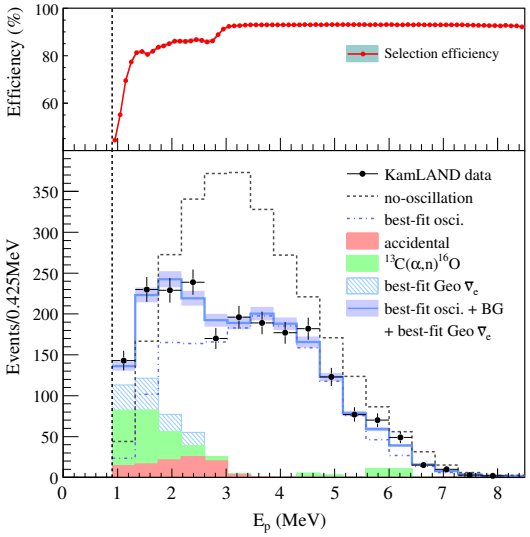

Figure 5.7: Prompt energy spectrum of $\overline{\nu}_e$ events with 0.9 MeV threshold energy. The data are fitted with three flavour neutrino oscillation analysis and the geo-$\overline{\nu}_e$ are unconstrained. In the top panel shows also the energy-dependent selection efficiency.

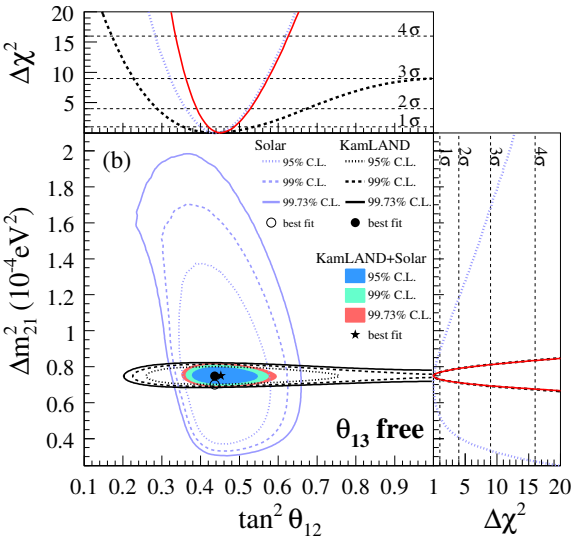

Figure 5.8: The $\Delta\chi^2$ obtained from the KamLand fit plus the solar fit experiment.

where $\tilde{P}^{2\nu}_{ee}$ is evaluated as in the earth case in which:

$$\tilde{P}^{2\nu}_{ee} = 1 - \sin^2 2\theta_{12\oplus} \sin^2\left(\frac{1.27 \cdot \Delta m^2_{12\oplus} L}{E}\right) \tag{5.64}$$

where L is the distance from the nuclear plant in which the anti-neutrino is produced and E is the energy of emission of $\overline{\nu}_e$ in MeV. Here $\sin^2 2\theta_{12\oplus}$ and $\Delta m^2_{12\oplus}$ are defined in the usual way taking into account the new definition of densities 5.41:

$$\sin^2 2\theta_{12\oplus} = \frac{\sin^2 2\theta_{12}}{(\cos 2\theta_{12} - A/\Delta m^2_{12})^2 + \sin^2 2\theta_{12}} \tag{5.65}$$

and

$$\Delta m^2_{12\oplus} = \Delta m^2_{12}\sqrt{(\cos 2\theta_{12} - A/\Delta m^2_{12})^2 + \sin^2 2\theta_{12}} \tag{5.66}$$

where $A = a_\oplus$ show in Eq.5.44.

5.3 Results

The $\Delta\chi^2$ maps in Fig.5.9 shows the dependence of matter potential by a linear combination of two parameters $\mathcal{E}_s$ and $\mathcal{E}_{ns}$ drawing a valley beside, in good approximation,

to the plane $\mathcal{E}_s = 0.57\mathcal{E}_{ns} + c$. This means that the parametrization done in [25, 26] changes with chemical features of the medium considered and then with its neutron, proton ratio, as shown in Eq.5.11. For the solar neutrinos the correlation between $\mathcal{E}_s$ and $\mathcal{E}_{ns}$ is dominate only by the solar n_n/n_p ratio because, in the Earth interior, this ratio is much smaller (Eq.5.13). The $\Delta\chi^2$ map also shows the dependence of A_{MSW} parameter on the neutrino experiment results and which measurement we can prefer to improve the narrow shape of the valley.

The current measurements of neutrino fluxes performed by all experiments described in the previous section give a large shape of $\Delta\chi^2$ valley (5.9.a). The next measurements expected that could really improved this results are:

- the low energy threshold measurement for the ^{8}B neutrino flux within 3σ of CL,
- the observation of day-night asymmetry of ^{8}B neutrino flux at 2σ of CL.

We simulated the expected results to understand how these new measurements could change the $\Delta\chi^2$ valley. In Fig.5.9.b we simulated the actual ^{8}B flux at low energy [30] for high metallicity solar model. In Fig.5.9.c it is shown only the expected day-night asymmetry and in the last one Fig.5.9.d it is shown their combination. We observe in particular a strong reduction of the extension of $\Delta\chi^2$-valley Fig.5.9.b by improving the measurements of the low energy region for the ^{8}B solar neutrino flux as expected from future Borexino results or by lowering the threshold energy from SNO experiment. The day-night asymmetry effects are due only to the matter of the Earth, therefore, as discuss above, they did not give any appreciable improvements on $\mathcal{E}_{ns}$, but it places new bounds only on $\mathcal{E}_s$ as shown in Fig.5.9.c.

In addition these simulated results suggest to study the $\Delta\chi^2$ profile along the $\mathcal{E}_s - 0.57\mathcal{E}_{ns}$ direction.

We simulated the solar neutrino propagation with 1000 random values for $\mathcal{E}_s$ and $\mathcal{E}_{ns}$ in the Sun and in the Earth, then we calculated the expected experimental results and relative χ^2 in the global fit. We took the projection of all χ^2 results on $\mathcal{E}_s - 0.57\mathcal{E}_{ns}$ plane as show in Fig.5.10. In this figure the points are randomly distributed on $[\mathcal{E}_s, \mathcal{E}_{ns}]$ plane, but from the projection of their distribution, they draw a low profile that, in

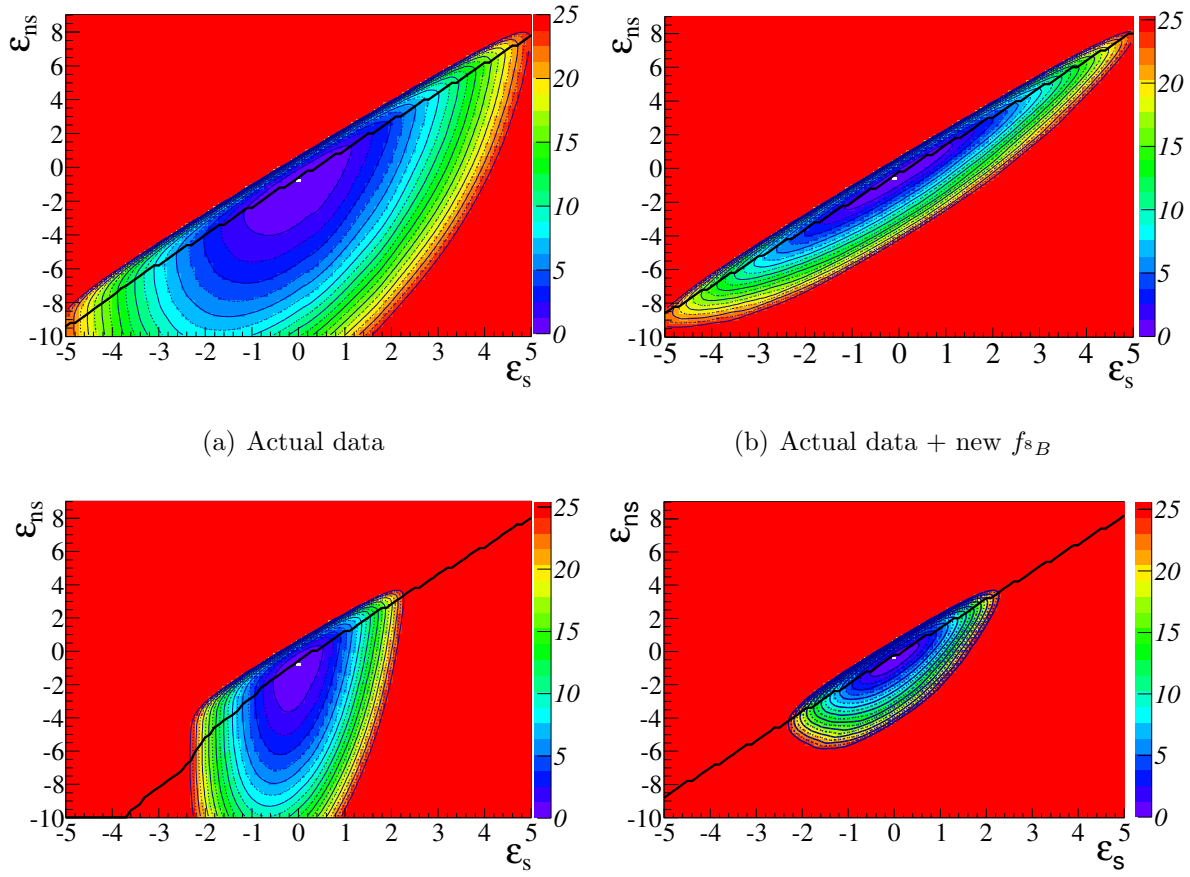

(a) Actual data

(b) Actual data + new $f_{^8B}$

(c) Actual data + expected D/N asymmetry

(d) Actual data+ $f_{^8B}$ + D/N asymmetry

Figure 5.9: $\Delta\chi^2$ contour plots varying $\mathcal{E}_s$ and $\mathcal{E}_{ns}$ and marginalizing the Δm^2_{12}, $\tan^2\theta_{12}$ and $\cos^2\theta_{13}$. In figure a) is generated with the current solar neutrino data. In figure b and c we added to the current data the expected results for the new ^8B neutrino flux at low energy and the expected new D/N asymmetry with higher CL. In last figure d) the combination of both with the current solar neutrino data.

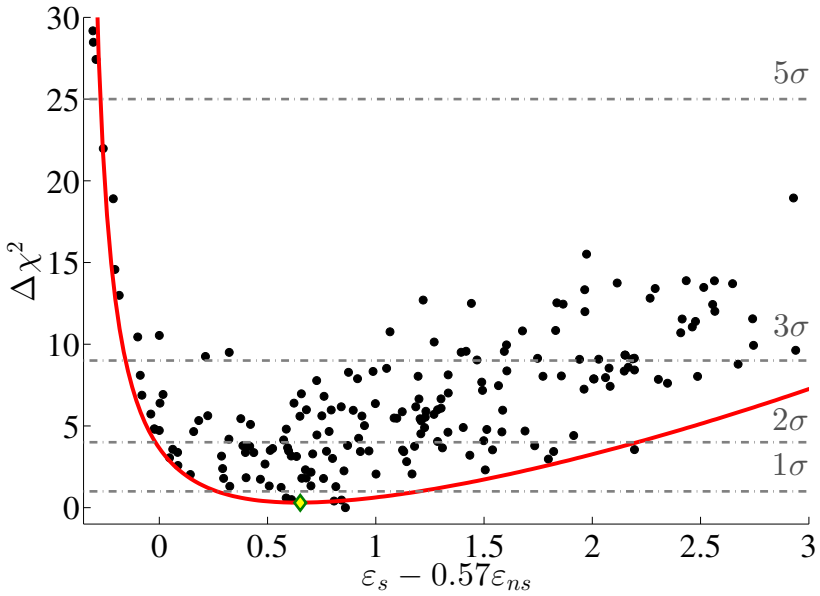

Figure 5.10: Lower profile for the $\Delta\chi^2$ obtained from the projection of all points present in $\mathcal{E}_S$ vs. $\mathcal{E}_{NS}$ on the $\mathcal{E}_S - 0.57\mathcal{E}_{NS}$ plane. Here the green-yellow dot represent the minimum of this profile made by means of a interpolation of the lower points of the distribution.

first approximation, is the minimum profile of the χ^2 valley.

In Fig.5.10 we considered only the last neutrino experiment results, therefore the strong improvement from the ^{8}B spectrum is not present, but, starting from the Eq.5.13

$$A_{MSW} = 1 + \mathcal{E}_s - 0.57\mathcal{E}_{ns},$$

we can observe two main results. First, the vacuum solution $A_{MSW} = 0$ ($\mathcal{E}_s - 0.57\mathcal{E}_{ns} = -1$) is excluded over 5σ. Second, the minimum is found at $\mathcal{E}_s - 0.57\mathcal{E}_{ns} = 0.65$ that it is larger than SI solution, in which the expected value is $\mathcal{E}_s - 0.57\mathcal{E}_{ns} = 0$ (or $A_{MSW} = 1$). The standard solution is contained within 2σ of CL, then it is not excluded, but there could be present also some extra interactions that make the matter potential in MSW larger than the standard one.

Actually, the current solar neutrino results are not able to put other constraints on this new parameter.

The new results expected from Borexino phase II, about the low energy ^{8}B solar neutrino flux with higher statistics and also the new analysis on ^{7}Be flux with lower background, may be able to give new important informations or new constraint about the NSI parameters, in both the cases, for propagation and detection, as suggest in [1].

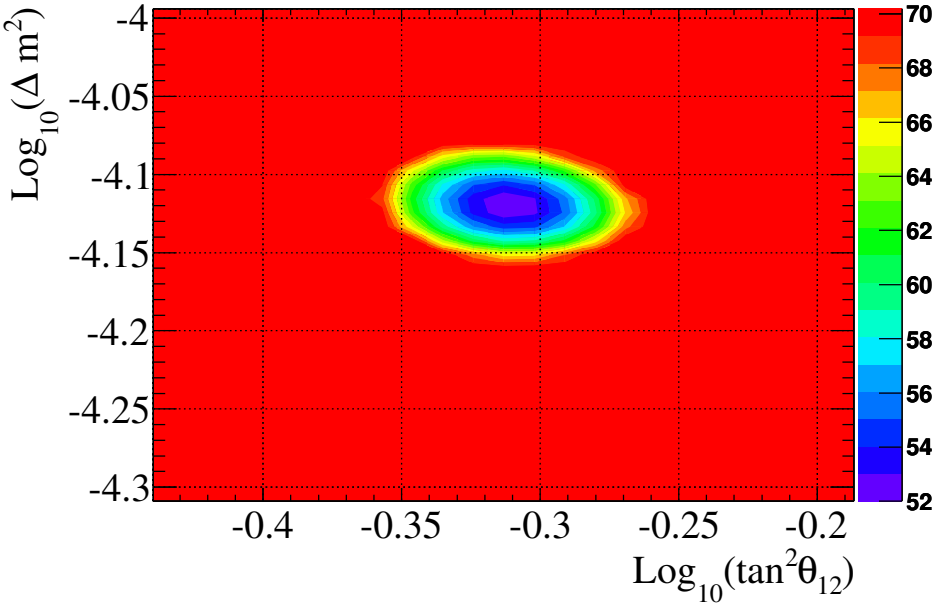

Figure 5.11: χ^2-map for MSW parameters ($\log_{10}\tan^2\theta_{12}$, $\log_{10}\Delta m^2_{12}$) around the minimum of $\Delta\chi^2$ distribution in Fig.5.10 for the new variable $\mathcal{E} - 0.57\mathcal{E}_{ns} = 0.65$.

Chapter 6

Conclusions

The analysis performed in this thesis guarantees that flux observed from Borexino with an average rate of $R_{Be7} = 46.0 \pm 1.5(\text{stat}) \, ^{1.5}_{1.6}(\text{syst})$ cpd/100tons is generated by the Sun, because of its intrinsic seasonal signature. On the Earth there could be several physical quantities that could have the same periodicity, therefore a particular accuracy was required in order to exclude all possible interferences from degenerate spectral components. In particular, the main contribution could be due to the muon flux which has also a seasonal modulation, but with opposite phase. A trace of the muon modulation can be detected, with the EMD decomposition, in the ^{11}C spectrum that present a IMF with opposite phase as expected. The strong dependence of the count rates on the vessel shape has been reduced by means of the choice of a asymmetric fiducial volume from top to bottom.

The tool developed in this work to identify the nylon vessel shape is a valid criterion to perform the study of vessel stability useful also for the *"Operational Group"* to investigate the status of detector taking an image of the vessel each week without stopping the data acquisition. So far, in order to observe the inner vessel status, it was necessary to stop the data taking for 3 days each 6 months, in order to switch on the lights inside the stainless steel sphere and take the pictures. This operation is particular dangerous for the PMTs exposed to high luminosity. Starting from now this kind of operations could be performed only once per year, for example.

The criteria for the data selection adopted for this analysis, allowed us to obtain the

cleanest sample with a maximized signal to noise ratio (SNR). Unfortunately the statistical fluctuations of the data taken day by day (about 24h for each data point) do not permit to appreciate the small variations of the count rates due to the increasing or decreasing of the neutrino fluxes. In addition also the background time instability, mainly due to the ^{210}Bi events, makes much more difficult to perform this measurement.

Fortunately the time scale of the noise, the signal and of the background are very different each other. In the first approximation the spectral components of each contribution have a different frequency ranges, therefore could be possible to separate each one by means of a filter. The *sifting* algorithm perform exactly this operation, leaving in each IMF of a given mode a residual signal in which the frequencies range is about half of the previous one.

This is a characteristic of the so called *dyadic* filter. The sifting is able to perform this operation by filtering out all the high frequencies, due to the statistical fluctuations, leaving only the real signal present in the dataset, although with a weak amplitude as in the seasonal modulation case.

The main difference with the Fourier analysis is that the EMD filters out the real spectral components, on the contrary the Fourier analysis "generate[1]" the harmonics in order to improve the approximation to the real signal by means of a finite Fourier series.

In addition the Fourier transform has a bad behavior on non linear and non periodic functions, as in the case of very noisy signals.

This means that all techniques which adopt the Fourier transforms have a worse frequency resolution when are applied on the non periodic functions,with respect to the EMD. This worse resolution is due to the attempt to better approximate the non linear function.

In this thesis we deeply investigated the real capability of the EMD to observe the seasonal modulation.

[1]Really, for each harmonic component it is associated an amplitude obtained by means of a minimization.

By means of several simulations we checked mainly the real capability to perform the measurements of the amplitude, the frequency and finally of the initial phase of the seasonal sinusoidal-like function.

The main problem found is the strong dependence of IMF functions on the random noise in the initial dataset (initial conditions). It has been solved by summing a random white noise[2] 100 times to the initial dataset. Each time we extracted all the oscillation modes and then we took the average of all 100 IMF for each oscillation mode.

This procedure guarantees that the IMF average is independent from the initial noise component of a given dataset and also the extracted information.

We found a good sensitivity to the frequency of the seasonal modulation with a value in good agreement with the annual periodicity, but weaker agreement for the amplitude. The eccentricity of the Earth orbit is found within 3σ of the expected one. A possible cause of this slight divergence could be a strong influences of the background + vessel shapes variation not completely eliminated yet.

The EMD finally was able to extract as last residual function the most reliable function that can describe the background time variation, opening new possibility to perform more accurate measurements for the CNO neutrinos.

In the second part of this work I dealt with the non standard interactions (NSI). This is a real big field in which the frontiers have not been explored yet and the Borexino experiment might be really the only experiment that could provide new information. For the NSI there are two kind of approaches: the physics related to the particle detection and the second one related to the propagation. I focussed on the propagation part of the problem by performing a simulation of neutrino propagation from the production point in the interior of the Sun, to its arrival on the Earth. Along this path, excluding the solar core regions in which the flavour oscillation happens, the neutrino propagates in the vacuum without any perturbations. We can observe this flux during the day time with the detectors. A different quantity of the flux is observed

[2]The withe noise is obtained by means of a random generator of events with a Gaussian distribution around the central value, by definition.

during the night because of regeneration effect due to non negligible density of Earth interior (up to a tenth of the solar density). This effect depends also on the neutrino energy and for this reason Borexino is not able to observe this asymmetry from the ν_{Be7} energy ($E_\nu = 0.862$ MeV). In the simulation I assumed that the matter potential of MSW theory, responsible for the flavour resonance effect in high density matter, could be parametrized to understand which kind of interaction is dominant during the neutrino propagation. The results show a strong dependence on the neutron/proton ratio, therefore on the chemical composition of the medium in which propagate. They show also direct proportionality between two free parameter $\mathcal{E}_s$ and $\mathcal{E}_{ns}$ adopted in the simulation. The main result is that a detailed study on low energy region for ν_{B8} spectrum is preferred because the parameter A_{MSW} with which the parametrization has been done is much more sensitive at this energy range. Unfortunately the flux of ν_{Be7} does not provided a big contribution to the A_{MSW} shape, although it permitted the exclusion of LOW solution in the Δm_{12} vs $\tan\theta_{12}$ space. The simulations pointed out that the parameter A_{MSW} prefers values more larger than 1 as shown in Fig.5.10 where the minimum of $\Delta\chi^2$ for the parameter $\mathcal{E}_s - 0.57\mathcal{E}_{ns}$ is bigger than 0 (standard MSW effect). This result can indicate that some new kind of interaction can be take into consideration and that this is independent of the solar density. In addition extra terms in Lagrangian interaction are not excluded, but at present the solar neutrino experiment are not able to improve the resolution on the A_{MSW} parameter.

Bibliography

[1] S. K. Agarwalla, F. Lombardi and T. Takeuchi, arXiv:1207.3492 [hep-ph].

[2] J. Hosaka *et al.* [Super-Kamiokande Collaboration], Phys. Rev. D **73** (2006) 112001 [hep-ex/0508053].

[3] Cravens, J. P., et al. 2008, Phys. Rev. D, 78, 032002

[4] Boger, J., et al. 2000, Nuclear Instruments and Methods in Physics Research A, 449, 172

[5] K. Abe *et al.* [Super-Kamiokande Collaboration], Phys. Rev. D **83** (2011) 052010 [arXiv:1010.0118 [hep-ex]].

[6] J.B. Birks, Scintillations from organic crystals: Specific fluorescence and relative response to different radiations, Proc. Phys. Soc. A **64** (1951), pp. 874-877

[7] J.B. Birks, *The Theory and Practice of Scintillation Counting*, Pergamon Press (1964).

[8] V.I. Tretyak, Semi-empirical calculation of quenching factors for ions in scintillators, As- tropart. Phys. 33 (2010).

[9] R. Ardito, C. Arnaboldi, D. R. Artusa, F. T. Avignone, III, M. Balata, I. Bandac, M. Barucci and J. W. Beeman *et al.*, hep-ex/0501010.

[10] K. Nakamura et al., (Particle Data Group) The Review of Particle Physics. *J. Phys. G.* **37** (2010) 075021.

[11] B. Aharmim *et al.* [SNO Collaboration], arXiv:1109.0763 [nucl-ex].

[12] S. Abe *et al.* [KamLAND Collaboration], "Precision Measurement of Neutrino Oscillation Parameters with KamLAND," Phys. Rev. Lett. **100** (2008) 221803 [arXiv:0801.4589 [hep-ex]].

[13] Bellini, G., Benziger, J., Bick, D., et al. 2011, Journal of Instrumentation, 6, 5005

[14] V. Lagomarsino, G. Testera NIM A 430, 2 435 (1999).

[15] T. Araki *et al.* [KamLAND Collaboration], "Measurement of neutrino oscillation with KamLAND: Evidence of spectral distortion," Phys. Rev. Lett. **94** (2005) 081801 [hep-ex/0406035].

[16] G. Alimonti *et al.* [Borexino Collaboration], Nucl. Instrum. Meth. A **609** (2009) 58.

[17] G. Alimonti *et al.* [Borexino Collaboration], Nucl. Instrum. Meth. A **600** (2009) 568 [arXiv:0806.2400 [physics.ins-det]].

[18] G. Bellini *et al.* [Borexino Collaboration], "Absence of day–night asymmetry of 862 keV ^{7}Be solar neutrino rate in Borexino and MSW oscillation parameters," Phys. Lett. B **707** (2012) 22 [arXiv:1104.2150 [hep-ex]].

[19] J. Benziger, L. Cadonati, F. Calaprice, E. de Haas, R. Fernholz, R. Ford, C. Galbiati and A. Goretti *et al.*, Nucl. Instrum. Meth. A **582**, 509 (2007) [physics/0702162 [PHYSICS]].

[20] F. Gatti, G. Morelli, G. Testera and S. Vitale, Nucl. Instrum. Meth. A **370** (1996) 609.

[21] F. P. An *et al.* [DAYA-BAY Collaboration], Phys. Rev. Lett. **108** (2012) 171803 [arXiv:1203.1669 [hep-ex]].

[22] M. Chen, F. Elisei, F. Masetti, U. Mazzucato, C. Salvo and G. Testera, Nucl. Instrum. Meth. A **420** (1999) 189.

[23] D. D'Angelo [Borexino Collaboration], arXiv:1109.3901 [hep-ex].

[24] D. Franco [Borexino Collaboration], Nucl. Phys. Proc. Suppl. **221** (2011) 344.

[25] G. L. Fogli, E. Lisi, A. Marrone and APalazzo, Phys. Lett. B **583** (2004) 149 [hep-ph/0309100].

[26] G. Fogli and E. Lisi, "Evidence for the MSW effect," New J. Phys. **6** (2004) 139.

[27] S. Davidson, C. Pena-Garay, N. Rius and A. Santamaria, "Present and future bounds on nonstandard neutrino interactions," JHEP **0303** (2003) 011 [hep-ph/0302093].

[28] A. Friedland, C. Lunardini and C. Pena-Garay, "Solar neutrinos as probes of neutrino matter interactions," Phys. Lett. B **594** (2004) 347 [hep-ph/0402266].

[29] Y. Takeuchi [Super-Kamiokande Collaboration], "Results from Super-Kamiokande," arXiv:1112.3425 [hep-ex].

[30] C. Pena-Garay and A. Serenelli, "Solar neutrinos and the solar composition problem," arXiv:0811.2424 [astro-ph].

[31] Rogers, F. J., & Iglesias, C. A. 1996, Bulletin of the American Astronomical Society, 28, 915

[32] Rogers, F. J., & Nayfonov, A. 2002, ApJ, 576, 1064

[33] Däppen, W. 2011, Contributions to Plasma Physics, 51, 328

[34] A. M. Serenelli, "New Results on Standard Solar Models," Astrophys. Space Sci. **328** (2010) 13 [arXiv:0910.3690 [astro-ph.SR]].

[35] B. Aharmim *et al.* [SNO Collaboration], "Low Energy Threshold Analysis of the Phase I and Phase II Data Sets of the Sudbury Neutrino Observatory," Phys. Rev. C **81** (2010) 055504 [arXiv:0910.2984 [nucl-ex]].

[36] A. Friedland and C. Lunardini, "Two modes of searching for new neutrino interactions at MINOS," Phys. Rev. D **74** (2006) 033012 [hep-ph/0606101].

[37] M. Deniz *et al.* [TEXONO Collaboration], Phys. Rev. D **82** (2010) 033004 [arXiv:1006.1947 [hep-ph]].

[38] P. Coloma, A. Donini, J. Lopez-Pavon and H. Minakata, JHEP **1108** (2011) 036 [arXiv:1105.5936 [hep-ph]].

[39] M. Altmann *et al.* [GNO Collaboration], Phys. Lett. B **616** (2005) 174 [hep-ex/0504037].

[40] V. N. Gavrin *et al.* [SAGE Collaboration],

[41] W. Hampel *et al.* [GALLEX Collaboration], Phys. Lett. B **447** (1999) 127.

[42] B. T. Cleveland, T. Daily, R. Davis, Jr., J. R. Distel, K. Lande, C. K. Lee, P. S. Wildenhain and J. Ullman, Astrophys. J. **496** (1998) 505.

[43] Z. Berezhiani, R. S. Raghavan and A. Rossi, Nucl. Phys. B **638** (2002) 62 [hep-ph/0111138].

[44] H. Minakata and C. Pena-Garay, Adv. High Energy Phys. **2012** (2012) 349686 [arXiv:1009.4869 [hep-ph]].

[45] M. Apollonio *et al.* [CHOOZ Collaboration], Eur. Phys. J. C **27** (2003) 331 [hep-ex/0301017].

[46] T. -K. Kuo and J. T. Pantaleone, Phys. Rev. Lett. **57** (1986) 1805.

[47] G. L. Fogli, E. Lisi and D. Montanino, "A comprehensive analysis of solar, atmospheric, accelerator and reactor neutrino experiments in a hierarchical three generation scheme," Phys. Rev. D **49** (1994) 3626.

[48] A. M. Dziewonski and D. L. Anderson, "Preliminary reference earth model (PREM)," Phys. Earth Planet. Interiors **25** (1981) 297.

[49] V. D. Barger, K. Whisnant, S. Pakvasa and R. J. N. Phillips, "Matter Effects on Three-Neutrino Oscillations," Phys. Rev. D **22** (1980) 2718.

[50] M. C. Gonzalez-Garcia, C. Pena-Garay, Y. Nir and A. Y. .Smirnov, "Phenomenology of maximal and near maximal lepton mixing," Phys. Rev. D **63** (2001) 013007 [hep-ph/0007227].

[51] M. C. Gonzalez-Garcia, C. Pena-Garay and A. Y. .Smirnov, "Zenith angle distributions at Super-Kamiokande and SNO and the solution of the solar neutrino problem," Phys. Rev. D **63** (2001) 113004 [hep-ph/0012313].

[52] J. N. Bahcall and C. Pena-Garay, JHEP **0311** (2003) 004 [hep-ph/0305159].

[53] J. N. Bahcall, "Gallium solar neutrino experiments: Absorption cross-sections, neutrino spectra, and predicted event rates," Phys. Rev. C **56** (1997) 3391 [hep-ph/9710491, hep-ph/9710491].

[54] Raffelt, G. G. 1996, *Stars as laboratories for fundamental physics : the astrophysics of neutrinos, axions, and other weakly interacting particles* / Georg G. Raffelt. Chicago : University of Chicago Press, 1996. (Theoretical astrophysics) QB464.2 .R34 1996

[55] Parke, S. J. 1986, Physical Review Letters, 57, 1275

[56] J. N. Bahcall, Phys. Rev. **135** (1964) B137.

[57] R. Davis, Jr., D. S. Harmer and K. C. Hoffman, Phys. Rev. Lett. **20** (1968) 1205.

[58] J. N. Bahcall, M. Kamionkowski and A. Sirlin, Phys. Rev. D **51** (1995) 6146 [astro-ph/9502003].

[59] H. Murayama and A. Pierce, Phys. Rev. D **65** (2002) 013012 [hep-ph/0012075].

[60] A. A. Hahn, K. Schreckenbach, G. Colvin, B. Krusche, W. Gelletly and F. Von Feilitzsch, Phys. Lett. B **218** (1989) 365.

[61] K. Schreckenbach, G. Colvin, W. Gelletly and F. Von Feilitzsch, Phys. Lett. B **160** (1985) 325.

[62] P. Vogel and J. Engel, Phys. Rev. D **39** (1989) 3378.

[63] "Proposal for US Participation in KamLAND," March 1999, `http://kamland.lbl.gov/KamLAND.US.Proposal.pdf`

[64] G. Alimonti, B. Alpat, C. Arpesella, G. Bellini, P. Benetti, S. Bonetti, F. P. Calaprice and M. Campanella *et al.*, Nucl. Phys. Proc. Suppl. **32** (1993) 149.

[65] Anselmann, P. et al. 1992 Physics Letters B, 285, 376

[66] Anselmann, P. et al. 1992 Physics Letters B, 285, 390

[67] Anselmann, P. et al. 1993 Physics Letters B, 314, 445

[68] Anselmann, P., 1994, Physics Letters B, 327, 377

[69] Anselmann, P., 1995, Physics Letters B, 342, 440

[70] Anselmann, P., 1995, Physics Letters B, 357, 237

[71] Abazov, A. I., et al. 1991, Physical Review Letters, 67, 3332

[72] Abdurashitov, J. N., et al. 1994, Physics Letters B, 328, 234

[73] Abdurashitov, J. N., et al. 1999, Phys. Rev. C, 60, 055801

[74] Abdurashitov, J. N., et al. 1999, *Physical Review Letters*, 83, 4686

[75] Abdurashitov, J. N., et al. 2002, *Soviet Journal of Experimental and Theoretical Physics*, 95, 181

[76] Abdurashitov, J. N., et al. 2006, Astroparticle Physics, 25, 349

[77] Pontecorvo, B. 1946, Chalk River Report PD 205

[78] Alvarez, L. W., 1949 , University of California Radiation Laboratory Report UCRL 328

[79] E. Gatti, F. De Martini, , Nuclear Electronics, 265-276, Vol. 2, 1962

[80] E. Gatti et al., Energia Nucleare 17 (1970) 34, pdf.

[81] H. O. Back et al. (Borexino collaboration), Nucl. Inst. Meth. A 584 (2008) 98.

[82] Chieffi, A., Limongi, M., & Straniero, O. 1998, ApJ, 502, 737

[83] Grevesse, N., & Sauval, A. J. 1998, Space Science Reviews, 85, 161

[84] M. Asplund, N. Grevesse, & A. J. Sauval, Cosmic Abundances as Records of Stellar Evolution and Nucleosynthesis, **336**, 25 (2005).

[85] M. Asplund, N. Grevesse, A. J. Sauval and P. Scott, Ann. Rev. Astron. Astrophys. **47** (2009) 481 [arXiv:0909.0948 [astro-ph.SR]].

[86] Davis, R., Harmer, D. S., & Hoffman, K. C. 1968, Physical Review Letters, **20**, 1205

[87] Araki, T., et al. 2005, Physical Review Letters, **94**, 081801

[88] J. Beringer et al. (Particle Data Group), Phys. Rev. **D86**, 010001 (2012)

[89] Standish, E. Myles; Williams, James C.. "Orbital Ephemerides of the Sun, Moon, and Planets". International Astronomical Union Commission 4: (Ephemerides). Retrieved 2010-04-03. (PDF).

[90] G. Bellini *et al.* [Borexino Collaboration], JCAP **1205**, 015 (2012) [arXiv:1202.6403 [hep-ex]].

[91] G. Bellini, J. Benziger, D. Bick, S. Bonetti, G. Bonfini, M. Buizza Avanzini, B. Caccianiga and L. Cadonati *et al.*, Phys. Rev. Lett. **107** (2011) 141302 [arXiv:1104.1816 [hep-ex]].

[92] G. Bellini *et al.* [Borexino Collaboration], Phys. Rev. Lett. **108** (2012) 051302 [arXiv:1110.3230 [hep-ex]].

[93] H. Back et al. (Borexino Collaboration) Journal Of Instrumentation 7 (10) P10018 (2012).

[94] G. Alimonti et al., (Borexino Collaboration) Physics Letters B 422, 349 (1998).

[95] G. Bellini *et al.* [Borexino Collaboration], "Measurement of the solar 8B neutrino rate with a liquid scintillator target and 3 MeV energy threshold in the Borexino detector," Phys. Rev. D **82** (2010) 033006 [arXiv:0808.2868 [astro-ph]].

[96] Pais, A., & Piccioni, O. 1955, Physical Review , 100, 1487

[97] Pontecorvo, B. 1957, Zh. Exsp. Tor. Fiz., 34, 247.

[98] Huang, N. E., Shen, Z., Long, S. R., et al. 1998, Royal Society of London Proceedings Series A, 454, 903

[99] Wu, Z.; Huang, N. E. (2004). *"A Study of the Characteristics of White Noise Using the Empirical Mode Decomposition Method"*. Proceedings of the Royal Society of London A 460 (2046): 15971611. doi:10.1098/rspa.2003.1221 – (pdf)

[100] Huang, N. E., Z. Wu, S. R. Long, K. C. Arnold, X. Chen and K. Blank, 2009, *"On instantaneous frequency"*, Advance in Adaptive Data Analysis. Vol.1, No.2. 177-229. (pdf)

[101] Wu Z.; and Huang N. E.; (2010) *"On the Filtering Properties of the Empirical Mode Decomposition"*. Adv. Adaptive Data Anal., Vol. 2, No. 4, 397-414. (pdf)

[102] Gang Wang, Xian-Yao Chen, Fang-Li Qiao, Zhaohua Wu, Norden E. Huang, 2010, *"On Intrinsic Mode Function"*, Advances in Adaptive Data Analysis ,Volume 02, Issue 03; DOI: 10.1142/S1793536910000549 – (pdf)

[103] G. Rilling, P. Flandrin, and P. Gonalves. *"On empirical mode decomposition and its algorithms"*. In Proceedings of IEEE-EURASIP Workshop on Nonlinear Signal and Image Processing NSIP-03, Grado (Italy), June 2003.

[104] Flandrin, P.; Rilling, G.; Gonalves, P. (2003). *"Empirical Mode Decomposition as a Filterbank"* (pdf). IEEE Signal Processing Letters 11 (2): 112114. doi:10.1109/LSP.2003.821662 – (pdf)

[105] E. Bedrosian, *"A product theorem for Hilbert transform"*, Proc. IEEE 51 (1963), 868-869.

[106] A.H Nuttall, *"On the quadrature approximation to the Hilbert transform of modulated signal"*, Proc IEEE 54 (1966) 1458-1459.

[107] Strumia, A., & Vissani, F. 2006, arXiv:hep-ph/0606054

[108] Ianni, A. 2004, Nuclear Instruments and Methods in Physics Research A, 516, 184

[109] H. Nyquist, "Certain topics in telegraph transmission theory", Trans. AIEE, vol. 47, pp. 617644, Apr. 1928 Reprint as classic paper in: Proc. IEEE, Vol. 90, No. 2, Feb 2002

[110] C. E. Shannon, "Communication in the presence of noise", Proc. Institute of Radio Engineers, vol. 37, no.1, pp. 1021, Jan. 1949.Reprint as classic paper in: Proc. IEEE, Vol. 86, No. 2, (Feb 1998)